

NAVIGATION AND SYSTEM IDENTIFICATION OF AN UNMANNED
UNDERWATER SURVEY VEHICLE

A THESIS SUBMITTED TO
THE GRADUATE SCHOOL OF NATURAL AND APPLIED SCIENCES
OF
MIDDLE EAST TECHNICAL UNIVERSITY

BY

SEDA KARADENİZ KARTAL

IN PARTIAL FULFILLMENT OF THE REQUIREMENTS
FOR
THE DEGREE OF DOCTOR OF PHILOSOPHY
IN
ELECTRICAL AND ELECTRONICS ENGINEERING

JANUARY 2017

Approval of the thesis:

**NAVIGATION AND SYSTEM IDENTIFICATION OF AN UNMANNED
UNDERWATER SURVEY VEHICLE**

submitted by **SEDA KARADENİZ KARTAL** in partial fulfillment of the requirements for the degree of **Doctor of Philosophy in Electrical and Electronics Engineering Department, Middle East Technical University** by,

Prof. Dr. Gülbin Dural Ünver
Dean, Graduate School of **Natural and Applied Sciences** _____

Prof. Dr. Tolga Çiloğlu
Head of Department, **Electrical and Electronics Engineering** _____

Prof. Dr. M. Kemal Leblebicioğlu
Supervisor, **Electrical and Electronics Engineering Dept., METU** _____

Examining Committee Members:

Prof. Dr. M. Kemal Özgören
Mechanical Engineering Department, METU _____

Prof. Dr. M. Kemal Leblebicioğlu
Electrical and Electronics Engineering Department, METU _____

Prof. Dr. M. Önder Efe
Computer Engineering Department, Hacettepe University _____

Prof. Dr. Ömer Morgül
Electrical and Electronics Engineering Dept., Bilkent University _____

Assoc. Prof. Dr. Afşar Saranlı
Electrical and Electronics Engineering Department, METU _____

Date:

27/01/2017

I hereby declare that all information in this document has been obtained and presented in accordance with academic rules and ethical conduct. I also declare that, as required by these rules and conduct, I have fully cited and referenced all material and results that are not original to this work.

Name, Last Name: SEDA KARADENİZ KARTAL

Signature :

ABSTRACT

NAVIGATION AND SYSTEM IDENTIFICATION OF AN UNMANNED UNDERWATER SURVEY VEHICLE

KARTAL, SEDA KARADENİZ

Ph.D., Department of Electrical and Electronics Engineering

Supervisor : Prof. Dr. M. Kemal Leblebicioğlu

January 2017, 187 pages

This study includes the mathematical model of an unmanned underwater vehicle, autopilot and the guidance design, the navigation solution and system identification of the unmanned underwater survey vehicle SAGA (Su Altı Gözlem Aracı). First, the 6 degrees-of-freedom (DOF) nonlinear mathematical model of an unmanned underwater vehicle is obtained by a Newton-Euler formulation. Then, the autopilot is designed by utilizing the proportional–integral–derivative (PID) control approach. The navigation problem is solved by integrating the inertial navigation system, acoustic and vision based measurement system and aiding sensors. All measurements are obtained in simulation environment. Performance of the resultant navigation system is analyzed by creating suitable system state, measurement and noise models. The navigational data of the vehicle is improved by utilizing a Kalman filter. After the navigation problem solved, guidance is performed by the way point guidance algorithm by line-of-sight (LOS) and the way point guidance based optimal control with navigational data. The pool experimental set-up is designed by using the inertial navigation system and acoustic-based measurement system composed of pinger and hydrophones together. These are integrated to obtain navigation data of the vehicle more accurately. In addition, the depth sensor is used in order to support depth information. The mathematical model of the vehicle includes some unknown parameters such as added mass and damping coefficients. It is not possible to determine all the parameters values as their effect on the state of the system is usually negligible. On

the other hand, most of the “important” parameters are obtained based on a system identification study of the vehicle by using this estimated experimental navigational data for coupled motion. All of this study is performed in a Matlab/Simulink environment.

Keywords: Mathematical Modelling of an Unmanned Underwater Vehicle, Autopilot, Guidance, Navigation, Acoustic-based Navigation, Vision-based Navigation, Inertial Navigation System, System Identification, Kalman Filter, Sensor Fusion

ÖZ

BİR İNSANSIZ SUALTI GÖZLEM ARACININ NAVİGASYONU VE SİSTEM TANILAMASI

KARTAL, SEDA KARADENİZ

Doktora, Elektrik ve Elektronik Mühendisliği Bölümü

Tez Yöneticisi : Prof. Dr. M. Kemal Leblebicioğlu

Ocak 2017 , 187 sayfa

Bu çalışma, bir insansız sualtı aracının matematiksel modelini, otopilot, güdüm tasarımını, yer tespiti çalışmaları ile SAGA'ya ait sistem tanılama çalışmalarını içermektedir. İlk olarak bir insansız su altı aracının Newton-Euler formülasyonundan gelen 6 serbestlik dereceli doğrusal olmayan modeli elde edilmiştir. Daha sonra aracın otopilotu, PID kontrol yaklaşımı ile tasarlanmıştır. Ataletsel ölçüm sistemi ile akustik ve görüntüleme temelli ölçüm sistemi ile yardımcı algılayıcılar entegre edilerek navigasyon problemi çözülmüştür. Tüm bu ölçümler simülasyon bazlı üretilmiştir. Navigasyon sisteminin performansı uygun sistem durumu ile ölçüm ve gürültü modelleri oluşturularak analiz edilmiştir. Navigasyon datası Kalman filtre ile iyileştirilmiştir. Navigasyon problemi çözüldükten sonra, aracın güdümü görüş hattı ve optimal kontrol yöntemleri ile navigasyon datası kullanılarak gerçekleştirilmiştir. Pinger ve hidrofonlardan oluşan akustik temelli ölçüm sistemi ile ataletsel ölçüm sistemi kullanılarak havuz deney düzeneği oluşturulmuştur. Aracın daha doğru yer bilgisi için bu iki ölçüm sistemi birleştirilmiştir. Buna ek olarak basınç algılayıcısı ile aracın derinlik bilgisi desteklenmiştir. Aracın matematiksel modeli katma kütle ve sönümleme parametreleri gibi değeri bilinmeyen parametreler içerir. Sistemin durumu üzerindeki etkisi genellikle ihmal edilebilir olduğu için tüm parametre değerlerini belirlemek mümkün değildir. Buna karşın, "önemli" parametrelerin çoğu, aracın birleşik hareketi için, kesirilen deneysel navigasyon bilgisini kullanarak sistem tanımlama çalışmasıyla elde

edilir. Tüm bu çalışmalar Matlab/Simulink de yapılmıştır.

Anahtar Kelimeler: İnsansız Sualtı Aracının Matematiksel Modeli, Otopilot, GÜdüm, Navigasyon, Akustik-temelli Navigasyon, Görüntü-temelli Navigasyon, Ataletsel Navigasyon sistemi, Sistem Tanılama, Kalman Filtresi, Sensör Birleştirme

To my father, mother and brother

Memet, Öngül, Ufuk

ACKNOWLEDGMENTS

I would like to express my deep appreciation and sincere gratitude to my supervisor Prof. Dr. M. Kemal Leblebiciođlu for his leading guidance, encouragement, criticism and continuous support from beginning to the end of my PhD. thesis. His advice on both research and my career have been invaluable.

I would like to thank Prof. Dr. M. Kemal Özgören and Assoc. Prof. Dr. Afşar Saranlı for their insightful guidance on my research interests.

This work is supported by Scientific and Technological Research Council of Turkey (TÜBİTAK) under Grant 111E267. I would like to thank TÜBİTAK for their financial support during my PhD. studies. I would also like to thank the Desistek Company and its employees for their help during the experiments.

I would like to thank Fırat Yılmaz Cevher for his support and for helpful discussions at the beginning of my study.

I also thank to Emre Ege, Orkun Öđücü, Mani Kazami and Abdul Ghafoor for their help during the pool and lake experiments. And, I also thank to Raha Shabani and the my colleagues from Computer Vision laboratory for all the emotional support.

I would like to express my special thanks to my father and mother and my dear brother's wife, Burçin for their perpetual support, encouragement, patience and trust.

I would like to express my endless thanks to my husband, my dear life friend, Burak Kartal, for being with me in this long and difficult process as always and for his patience and moral support. And, I also thank to my dear son and daughter, Ömer Yiđit and Buse for giving me worlds with a their smiles.

Finally, my brother, Ufuk, I do not have enough words to describe thanks to him.

TABLE OF CONTENTS

ABSTRACT	v
ÖZ	vii
ACKNOWLEDGMENTS	x
TABLE OF CONTENTS	xi
LIST OF TABLES	xvii
LIST OF FIGURES	xviii
LIST OF ABBREVIATIONS	xxviii

CHAPTERS

1	INTRODUCTION	1
1.1	Motivation of the Thesis	1
1.2	Literature Review	2
1.3	SAGA	4
1.4	Organization of the Thesis	5
2	MATHEMATICAL MODELLING	7
2.1	Introduction	7
2.2	Kinematics	8

2.2.1	Notation of Kinematics Quantities	8
2.2.2	Coordinate Frames	8
2.2.3	Euler Angles	10
2.3	Rigid Body Dynamics	14
2.4	Hydrodynamic Forces and Moments	16
2.4.1	Added Mass and Inertia	17
2.4.2	Hydrodynamic Damping	20
2.4.3	Restoring Forces and Moments	20
2.5	Equations of Motion	22
2.6	Conclusion	24
3	AUTOPILOT	25
3.1	Introduction	25
3.2	Thruster Model	25
3.3	Controller Design	30
3.3.1	Speed Controller	31
3.3.2	Heading Controller	34
3.3.3	Depth Controller	35
3.4	Conclusion	36
4	NAVIGATION	43
4.1	Introduction	43
4.2	Inertial Navigation System	44

4.2.1	Inertial Sensors	44
4.2.2	Error Charecteristics	45
4.2.3	Inertial Navigation Processor	46
4.2.3.1	Kinematics	46
4.2.3.1.1	Coordinate Transformation Matrix	46
4.2.3.1.2	Angular Rate	48
4.2.3.1.3	Position	48
4.2.3.1.4	Velocity	49
4.2.3.1.5	Acceleration	50
4.2.3.2	Earth Model	51
4.2.3.2.1	The Ellipsoid Model of the Earth's Surface	51
4.2.3.2.2	Curvilinear position	52
4.2.3.2.3	Earth Rotation	53
4.2.3.2.4	Specific Force, Gravita- tion, and Gravity	53
4.2.3.3	Inertial Navigation Equations	54
4.2.3.3.1	Attitude Update	55
4.2.3.3.2	Specific-Force Frame Trans- formation	56
4.2.3.3.3	Velocity Update	56
4.2.3.3.4	Position Update	57

4.2.3.4	INS Error Propagation	57
4.3	Global Navigation Satellite System (GNSS)	58
4.4	Acoustic-based Navigation System	60
4.5	Vision-based Navigation System	64
4.6	External Aids	66
4.7	Integrated Navigation	66
4.7.1	Integration Architectures	67
4.7.2	Correction	68
4.7.3	System Model and State Selection	68
4.7.4	Measurement Model	72
4.7.5	Estimation Algorithm	74
4.7.6	Simulation Results	75
4.8	Conclusion	77
5	GUIDANCE	87
5.1	Introduction	87
5.2	Way Point Guidance by LOS	88
5.2.1	Way Point Guidance in the Yaw Plane	89
5.2.2	Way Point Guidance in the Pitch Plane	91
5.2.3	Way Point Guidance in the 3D Motion	93
5.3	Optimal Guidance	95
5.3.1	Constrained Nonlinear Optimization	99

	5.3.2	Simulation Results for Optimal Guidance	100
6		EXPERIMENTS	107
	6.1	Introduction	107
	6.2	Acoustic-based Navigation Experiment of SAGA	108
	6.2.1	Inertial Measurement System and Aiding Sensor	117
	6.2.2	System Model and State Selection for Acoustic-based Navigation Experiment of SAGA	118
	6.2.3	Measurement Model for Acoustic-based Navigation Experiment of SAGA	122
	6.2.4	Simulation Results for the Acoustic-based Navigation Experiment of SAGA	127
	6.3	Conclusion	129
7		SYSTEM IDENTIFICATION OF SAGA	139
	7.1	Introduction	139
	7.2	System Identification Based on Simulation Data	142
	7.2.1	Uncoupled Motion Test Based On Simulation Data	142
	7.2.2	Coupled Motion Test Based on Simulation Data	147
	7.3	System Identification Based on Acoustic Experimental Data	155
	7.4	Conclusion	162
8		CONCLUSION AND FUTURE WORK	167
	8.1	Conclusion	167
	8.2	Future Work	168

APPENDICES

A EXPERIMENTAL WORK IN POOL AND LAKE 177

 A.1 Experimental Work in Pool and Lake 177

B SOME INFORMATION OF SENSORS USED IN THE EXPERI-
MENT 181

 B.1 UM7 Specifications 181

CURRICULUM VITAE 185

LIST OF TABLES

TABLES

Table 1.1	SAGA properties	4
Table 2.1	Notation used for underwater vehicles	7
Table 6.1	Detected peak times of the first, second, third and fourth received signals.	125
Table 6.2	Detected peak times of the fifth, sixth, seventh and eighth received signals.	126
Table 7.1	Decoupled motion of the vehicle and related parameters	140
Table 7.2	Optimization results for the surge motion test based on simulation data	143
Table 7.3	Optimization results for the yaw motion test based on simulation data	145
Table 7.4	Optimization results for pitch motion test based on simulation data .	149
Table 7.5	Damping coefficients as the results of optimization for coupled motion test based on simulation data	156
Table 7.6	Added mass parameters as the results of optimization for system identification for coupled motion test based on simulation data	156
Table 7.7	Damping coefficients as the results of optimization for system identification based on the acoustic experimental data	159
Table 7.8	Added mass parameters as the results of optimization for system identification based on the acoustic experimental data	163

LIST OF FIGURES

FIGURES

Figure 1.1	REMUS, AUV	2
Figure 1.2	DST-R-100-4, ROV	2
Figure 1.3	Hull of SAGA, unmanned underwater survey vehicle [15]	5
Figure 2.1	Body-fixed and earth-fixed reference frame	9
Figure 2.2	Euler angle rotation in z axes	11
Figure 2.3	Euler angle rotation in y axes	12
Figure 2.4	Euler angle rotation in x axes	12
Figure 3.1	Thruster (composed of motor controller-motor-propeller)	26
Figure 3.2	The relationship between PWM value and force (Kgf) [15]	27
Figure 3.3	SAGA's thrusters locations	28
Figure 3.4	Translational velocities in the body-fixed frame for test 1	29
Figure 3.5	Rotational velocities in the body-fixed frame for test 1	30
Figure 3.6	Translational velocities in body-fixed frame for test 2	31
Figure 3.7	Rotational velocities in body-fixed frame for test 2	32
Figure 3.8	Translational velocities in body-fixed frame for test 3	33
Figure 3.9	Rotational velocities in body-fixed frame for test 3	34
Figure 3.10	Translational velocities in body-fixed frame for test 4	35
Figure 3.11	Rotational velocities in body-fixed frame for test 4	36
Figure 3.12	Block diagram of the PID controller	37

Figure 3.13 The block diagram of surge speed controller of SAGA	37
Figure 3.14 Surge speed controller response	38
Figure 3.15 Right and left thrusters response	38
Figure 3.16 The block diagram of heave speed controller of SAGA	38
Figure 3.17 Heave speed controller response	39
Figure 3.18 Vertical thruster response	39
Figure 3.19 The block diagram of yaw rate controller of SAGA	40
Figure 3.20 Yaw rate controller response	40
Figure 3.21 Right and left thrusters response	40
Figure 3.22 The block diagram of yaw angle controller of SAGA	41
Figure 3.23 Heading angle controller response	41
Figure 3.24 The block diagram of depth controller of SAGA	41
Figure 3.25 Depth controller response	42
Figure 4.1 The schematic illustration of INS implementation	44
Figure 4.2 Cross-section of the ellipsoid representing the Earth's surface [20] .	52
Figure 4.3 Geocentric and geodetic latitude [20]	52
Figure 4.4 Schematic of an inertial navigation processor	55
Figure 4.5 GNSS system components. [20]	59
Figure 4.6 Position solution geometry using four satellite navigation signals [20]	60
Figure 4.7 The schematic illustration of the acoustic-based navigation system .	61
Figure 4.8 USBL range and angle measurement	63
Figure 4.9 The schematic illustration of the vision-based navigation system . .	65
Figure 4.10 Integrated Navigation Architecture	67
Figure 4.11 Actual position with respect to time in the Earth frame	76
Figure 4.12 Actual velocity with respect to time in the body coordinate frame .	77

Figure 4.13 Actual attitude with respect to time in the Earth frame	78
Figure 4.14 Actual and measured acceleration from IMU in the body coordinate frame	79
Figure 4.15 Actual and measured angular rate from IMU in the body coordinate frame	80
Figure 4.16 Actual velocity (blue line) and obtained velocity from IMU (red line) and the measured velocity from pitot tupe (green line) in the body coordinate frame	81
Figure 4.17 Actual attitude (blue line) and obtained attitude from IMU (red line) and the measured attitude from magnetic compass (green line) in the Earth coordinate frame	82
Figure 4.18 Actual and obtained position from IMU in the ECEF coordinate frame	83
Figure 4.19 Estimated surge, sway and heave speed error from solution of the integrating IMU and pitot tube data (red line) and the actual error (blue line)	83
Figure 4.20 The actual surge, sway and heave speed (blue line) and the corrected surge, sway and heave speed (red line)	84
Figure 4.21 Estimated roll, pitch and yaw angle error from solution of the integrating IMU and magnetic compass data (red line) and the real error (blue line)	84
Figure 4.22 The actual roll, pitch and yaw angle (blue line) and the corrected roll, pitch and yaw angle (red line)	85
Figure 4.23 The actual position in the x-axis (blue line), Estimated (corrected) position in the x axis for 2 cases: integrating IMU data and camera data (green line), integrating IMU data, vision data and acoustic data (red line)	85
Figure 4.24 The actual position in the y-axis (blue line), Estimated (corrected) position in the y axis for 2 cases: integrating IMU data and vision data (green line), integrating IMU data, vision and acoustic data (red line) . . .	86
Figure 4.25 The actual depth (blue line), Estimated (corrected) depth for 2 cases: integrating depth data coming from inertial navigation and acoustic-based navigation (green line), integrating depth data coming from inertial navigation, acoustic-based navigation and depth sensor (red line)	86
Figure 5.1 The schematic illustration of the combined system, navigation, controller, guidance and vehicle dynamics	88

Figure 5.2	Way point guidance and circle of acceptance [21]	89
Figure 5.3	The schematic illustration of the combined system for the yaw plane motion	90
Figure 5.4	Basic Line of Sight Guidance for the yaw plane	91
Figure 5.5	Way point guidance by LOS in the yaw plane	92
Figure 5.6	Way point guidance by LOS in the yaw plane for two reference points	93
Figure 5.7	The schematic illustration of the combined system for the pitch plane motion	94
Figure 5.8	Way point guidance by LOS in the pitch plane	95
Figure 5.9	The schematic illustration of the combined system for the 3D motion	96
Figure 5.10	Way point guidance by LOS in the 3D motion	97
Figure 5.11	Path possibilities and the illustration of the optimal solution for OCP	99
Figure 5.12	The tracked path for $u_0 = 0.5m/s$ with a different heave velocity, w_0	101
Figure 5.13	The tracked path for $u_0 = 0.5m/s$ in the x-y view	102
Figure 5.14	The tracked path for $u_0 = 0.5m/s$ in the x-z view	103
Figure 5.15	The tracked path for $u_0 = 0.5m/s$ in the y-z view	103
Figure 5.16	The tracked path for $u_0 = 1m/s$ with a different heave velocity, w_0	104
Figure 5.17	The tracked path for $u_0 = 1.5m/s$ with a different heave velocity, w_0	104
Figure 5.18	The tracked path for $u_0 = 0.5m/s$ with a different heave velocity, w_0	105
Figure 6.1	Navigation experiment of the SAGA in the pool of METU	107
Figure 6.2	Pinger used in the experiment	108
Figure 6.3	Hydrophone used in the experiment	109
Figure 6.4	Data card used in the experiment	110
Figure 6.5	Pool experiment set-up composed of pinger and hydrophones	111
Figure 6.6	Received signal from the 1st hydrophone with respect to time	112
Figure 6.7	Received signal from the 2nd hydrophone with respect to time	113
Figure 6.8	Received signal from the 3rd hydrophone with respect to time	113

Figure 6.9	Received signal from the 4th hydrophone with respect to time . . .	114
Figure 6.10	Received signal from the 5th hydrophone with respect to time . . .	114
Figure 6.11	Received signal from the 6th hydrophone with respect to time . . .	115
Figure 6.12	Received signal from the 7th hydrophone with respect to time . . .	115
Figure 6.13	Received signal from the 8th hydrophone with respect to time . . .	116
Figure 6.14	Filtered signal of received signal from the 1st hydrophone with respect to time and the peak times of this filtered signal	117
Figure 6.15	Filtered signal of received signal from the 2nd hydrophone with respect to time and the peak times of this filtered signal	118
Figure 6.16	Filtered signal of received signal from the 3rd hydrophone with respect to time and the peak times of this filtered signal	119
Figure 6.17	Filtered signal of received signal from the 4th hydrophone with respect to time and the peak times of this filtered signal	120
Figure 6.18	Filtered signal of received signal from the 5th hydrophone with respect to time and the peak times of this filtered signal	121
Figure 6.19	Filtered signal of received signal from the 6th hydrophone with respect to time and the peak times of this filtered signal	122
Figure 6.20	Filtered signal of received signal from the 7th hydrophone with respect to time and the peak times of this filtered signal	123
Figure 6.21	Filtered signal of received signal from the 8th hydrophone with respect to time and the peak times of this filtered signal	124
Figure 6.22	The position of the vehicle along x-axis obtained from the acoustic- based navigation system	127
Figure 6.23	The position of the vehicle along y-axis obtained from the acoustic- based navigation system	128
Figure 6.24	IMU (UM7) used in the experiment	129
Figure 6.25	Roll angle measured from the IMU with respect to time and fitted curve of the measured roll angle	130
Figure 6.26	Pitch angle measured from the IMU with respect to time and fitted curve of the measured pitch angle	130

Figure 6.27 Yaw angle measured from the IMU with respect to time and fitted curve of the measured yaw angle	131
Figure 6.28 Measured translational accelerations in x, y and z-axes from the IMU in the body frame	131
Figure 6.29 Obtained translational positions in x, y and z-axes from the IMU in the earth frame	132
Figure 6.30 Depth sensor used in the experiment	132
Figure 6.31 Measured depth comes from the depth sensor	133
Figure 6.32 Applied PWM value of the right, left and vertical thruster during the acoustic-based navigation experiment	133
Figure 6.33 Obtained force value of the right, left and vertical thruster during the acoustic-based navigation experiment	134
Figure 6.34 Real position errors in the x, y and z-axes (blue line) and the estimated position error in the x, y and z-axes from the Kalman filter (red line)	134
Figure 6.35 Real roll, pitch and yaw errors (blue line) and the estimated roll, pitch and yaw error from the Kalman filter (red line)	135
Figure 6.36 Real surge, sway and heave velocity errors (blue line) and the estimated surge, sway and heave velocity errors come from Kalman filter (red line)	135
Figure 6.37 The output of the integrated navigation solution, corrected positions in the earth frame	136
Figure 6.38 The output of the integrated navigation solution, corrected attitudes in the earth frame	136
Figure 6.39 The outputs of the integrated navigation solution, corrected surge, sway and heave speeds	137
Figure 7.1 Position in the x-axis coming from the model response and the estimated position in the x-axis from the integrated navigation solution for the surge motion test based on simulation data	143
Figure 7.2 Position in the x-axis coming from the model response (blue line) and the estimated position in the x-axis from the integrated navigation solution (red line) for the yaw motion test based on simulation data	145

Figure 7.3	Position in the y-axis coming from the model response (blue line) and the estimated position in the y-axis from the integrated navigation solution (red line) for the yaw motion test based on simulation data	146
Figure 7.4	Yaw angle coming from the model response (blue line) and the estimated yaw angle from the integrated navigation solution (red line) for the yaw motion test based on simulation data	147
Figure 7.5	Position in the x-axis coming from the model response (blue line) and the estimated position in the x-axis from the integrated navigation solution (red line) for the pitch motion test based on simulation data	148
Figure 7.6	Position in the z-axis coming from the model response (blue line) and the estimated position in the z-axis from the integrated navigation solution (red line) for the pitch motion test based on simulation data	148
Figure 7.7	Pitch angle coming from the model response (blue line) and the estimated pitch angle from the integrated navigation solution (red line) for the pitch motion test based on simulation data	149
Figure 7.8	Position in the x-axis coming from the model response (blue line) and the estimated position in the x-axis from the integrated navigation solution (red line) for the coupled motion test based on simulation data . .	150
Figure 7.9	Position in the y-axis coming from the model response (blue line) and the estimated position in the y-axis from the integrated navigation solution (red line) for the coupled motion test based on simulation data . .	151
Figure 7.10	Position in the z-axis coming from the model response (blue line) and the estimated position in the z-axis from the integrated navigation solution (red line) for the coupled motion test based on simulation data . .	151
Figure 7.11	Yaw angle coming from the model response (blue line) and the yaw angle from the integrated navigation solution (red line) for the coupled motion test based on simulation test	152
Figure 7.12	Pitch angle coming from the model response (blue line) and the pitch angle from the integrated navigation solution (red line) for the coupled motion test based on simulation test	152
Figure 7.13	The histogram of X_u value in the system identification based on simulation data for coupled motion	153
Figure 7.14	The histogram of $X_{\dot{u}}$ value in the system identification based on simulation data for coupled motion	153

Figure 7.15 The histogram of $Z_{[w]}$ value in the system identification based on simulation data for coupled motion	154
Figure 7.16 The histogram of $M_{[q]}$ value in the system identification based on simulation data for coupled motion	154
Figure 7.17 The histogram of N_r value in the system identification based on simulation data for coupled motion	155
Figure 7.18 The histogram of $N_{[r]}$ value in the system identification based on simulation data for coupled motion	155
Figure 7.19 Estimated position in the x-axis from the Kalman filter (green line), the position in the x-axis from the system model response before system identification based on simulated data (blue line) and the position in the x-axis from the system model response after system identification based on simulated data (red line) with respect to time for the coupled motion . .	156
Figure 7.20 Estimated position in the y-axis from the Kalman filter (green line), the position in the y-axis from the system model response before system identification based on simulated data (blue line) and the position in the y-axis from the system model response after system identification based on simulated data (red line) with respect to time for the coupled motion . .	157
Figure 7.21 Estimated position in the z-axis from the Kalman filter (green line), the position in the z-axis from the system model response before system identification based on simulated data (blue line) and the position in the z-axis from the system model response after system identification based on simulated data (red line) with respect to time for the coupled motion . .	157
Figure 7.22 Estimated yaw angle from the Kalman filter (green line), the yaw angle from the system model response before system identification basen on simulated data (blue line) and the yaw angle from the system model response after system identification based on simulated data (red line) with respect to time	158
Figure 7.23 Estimated pitch angle from the Kalman filter (green line), the pitch angle from the system model response before system identification basen on simulated data (blue line) and the pitch angle from the system model response after system identification based on simulated data (red line) with respect to time	158
Figure 7.24 The histogram of X_u value in the system identification based on the acoustic experimental data for coupled motion	159

Figure 7.25 The histogram of $X_{ u}$ value in the system identification based on the acoustic experimental data for coupled motion	160
Figure 7.26 The histogram of Z_w value in the system identification based on the acoustic experimental data for coupled motion	160
Figure 7.27 The histogram of $Z_{ w}$ value in the system identification based on the acoustic experimental data for coupled motion	161
Figure 7.28 The histogram of M_q value in the system identification based on the acoustic experimental data for coupled motion	161
Figure 7.29 The histogram of $M_{ q}$ value in the system identification based on the acoustic experimental data for coupled motion	162
Figure 7.30 The histogram of N_r value in the system identification based on the acoustic experimental data for coupled motion	162
Figure 7.31 The histogram of $N_{ r}$ value in the system identification based on the acoustic experimental data for coupled motion	163
Figure 7.32 Estimated position in the x-axis from the Kalman filter (green line), the position in the x-axis from the system model response before system identification based on acoustic experimental data (blue line) and the position in the x-axis from the system model response after system identification based on acoustic experimental data (red line) with respect to time	164
Figure 7.33 Estimated position in the y-axis from the Kalman filter (green line), position in the y-axis from the system model response before system identification based on acoustic experimental data (blue line) and position in the y-axis from the system model response after system identification based on acoustic experimental data (red line) with respect to time.	164
Figure 7.34 Estimated position in the z-axis from the Kalman filter (green line), the position in the z-axis from the system model response before system identification based on acoustic experimental data (blue line) and the position in the z-axis from the system model response after system identification based on acoustic experimental data (red line) with respect to time	165
Figure 7.35 Estimated yaw angle from the Kalman filter (green line), the yaw angle from the system model response before system identification based on acoustic experimental data (blue line) and the yaw angle from the system model response after system identification based on acoustic experimental data (red line) with respect to time	165

Figure 7.36 Estimated pitch angle from the Kalman filter (green line), the pitch angle from the system model response before system identification based on acoustic experimental data (blue line) and the pitch angle from the system model response after system identification based on acoustic experimental data (red line) with respect to time	166
Figure A.1 Experiment to test whether the pinger works	177
Figure A.2 Experiment to detect the critical distance between hydrophones and the pinger	178
Figure A.3 Acoustic-based navigation experiment set-up	178
Figure A.4 Acoustic-based navigation experimental set-up	179
Figure A.5 Experiment to test whether USBL works in the pool	179
Figure A.6 Experiment to test whether USBL works in the lake	180
Figure A.7 Experiment to test whether USBL works in the lake	180
Figure B.1 Attitude and heading specifications	181
Figure B.2 Gyro specifications	182
Figure B.3 Accelerometer specifications	182
Figure B.4 Magnetometer specifications	183

LIST OF ABBREVIATIONS

DOF	Degrees of freedom
CG	Center of Gravity
SAGA	Su Altı Gözlem Aracı
UUV	Unmanned underwater vehicle
AUV	Autonomous underwater vehicle
ROV	Remotely operated vehicle
SBL	Short base line
USBL	Ultra short base line
INS	Inertial navigation system
PID	Proportional–integral–derivative
IMU	Inertial measurement unit
ECEF	Earth center earth fixed frame
PWM	Pulse width modulation
TOD	Time of duration
LOS	Line of sight
OCP	Optimal control problem
GA	Genetic algorithm
GPS	Global Positioning System
GNSS	Global Navigation Satellite System

CHAPTER 1

INTRODUCTION

1.1 Motivation of the Thesis

There are many research operations on oceans which covers about seventy percent of the Earth such as underwater geological, hydro-graphic, archaeological and oil-gas research, port and ship security. Since most of these research operations have to be conducted in dangerous places, unmanned underwater vehicles (UUV) can be utilized for human safety. The first unmanned underwater vehicle, Self-Propelled Underwater Research Vehicle (SPRUV), was designed at the applied physics laboratory at the University of Washington as early as 1957 by Stan Murphy, Bob Francois and later on, Terry Ewart. It was used to study diffusion, acoustic transmission, and submarine wakes. Many different vehicles have been improved to date with developing technology.

UUV's are divided into two main classes according to the type of its operation. One of them is autonomous underwater vehicles (AUV's) and the other is the remotely operated vehicles (ROV's). While an AUV does not require input from operator, an ROV requires the control input from operator. Remote Environmental Monitoring UnitS (REMUS) can be given as an example for an AUV as shown in Fig.1.1. Its simulation model was developed in 6 DOF [36] in 2001. ROVs are classified according to size, depth capability, on board horsepower, and steering system (all-electric or electric-hydraulic). DST-R-100-4 which is in miniROV class can be given as an example for ROVs as shown in Fig. 1.2 was designed by Desistek Company in 2012.

In UUVs, navigation, guidance and control systems generally work together. The



Figure 1.1: REMUS, AUV

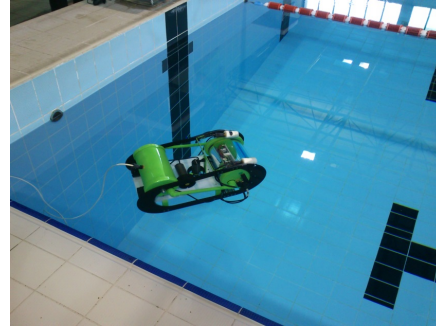


Figure 1.2: DST-R-100-4, ROV

position of the vehicle must first be known to direct the vehicle to go wherever. Navigation data is the reference signal for the guidance system of the vehicle. Guidance system generates the reference signal for the controllers of the vehicle. All the system provides the vehicle to go to the desired points with desired speed and attitude. The success of the system depends on the accuracy of the navigation information. In this thesis, solution of the navigation problem is explained in detail.

1.2 Literature Review

In general, mathematical models of UUVs are nonlinear; but linear models can be preferred sometimes [18]. This thesis focused on a nonlinear mathematical model (since it is more accurate and realistic). Mathematical models of UUVs have some unknown parameters such as added mass and damping coefficients. The added mass parameters and damping coefficients can be obtained by using some programs such as WAMIT, VERES, SEAWAY and SOLIDWORKS. If the structure of the vehicle has some symmetry with respect to pitch and yaw planes, added mass parameters can be approximately obtained by using the strip theory [18]. For more accuracy, the values of the parameters can be improved by a system identification study based on the navigational data from a physical experiment. System identification study can be performed offline after the experimental data is obtained. However, it was performed as online for realistic result [23]. Experimental identification was done for both coupled motion of the vehicle in 6 (DOF) and uncoupled motions such as surge, yaw, pitch, [31], [2]. In this study, the system identification was performed

using simulated data for both coupled and decoupled motion and it was done using experimental data for coupled motion of SAGA.

It is seen that the determination of the vehicle position is very important for the system identification study especially when the GPS data is unavailable. In general, there are three main categories of navigation systems for determination of vehicle position: acoustic-based navigation, inertial navigation and geophysical navigation [35]. Inertial navigation uses accelerometers and gyroscopes. The position error grows with time in inertial navigation [30] and [22]. Acoustic based navigation techniques are based on measuring time of duration (TOD) of signals from acoustic beacons or the opposite. In order to determine TOD there are three common methods such as ultra-short base line (USBL), short base line (SBL) and long base line (LBL) [17] and [6]. Geophysical navigation techniques use sonar, cameras and magnetometer for reference information [7] and [39]. For more accuracy in position, INS, acoustic-based navigation and geophysical navigation are integrated [28] and [32]. In this thesis, the inertial navigation system (INS) and acoustic-based data collection system with sensors (magnetometer and depth sensor) are integrated to determine the position of the vehicle with a reasonable accuracy.

The solution of the navigation data is reference signal of the guidance system. The guidance and control of the vehicle is very important for applications of these kinds of vehicles; because the vehicles have complex dynamics and there are difficulties in underwater environments. There are many control techniques to design autopilots for unmanned underwater vehicles (UUV). Speed autopilots are designed by P or PI control techniques [11]. Position autopilots are also designed by the same controllers [41]. More complicated autopilots are designed with PID and sliding mode control techniques [29]. Optimal kinematic control for an autonomous underwater vehicle and a particular set of optimal motions which trace helical paths are discussed in [5]. A new optimal control method based on the energy equations of the controlled system is presented in [19]. This method is applied on an under-actuated underwater vehicle. In the study of the configuration optimization for an underwater vehicle, the maneuver requirements of the optimization problem are obtained by the solution of an optimal control problem [1]. Optimal control is applied on an underwater sensor network for cooperative target tracking [4]. In this thesis, the surge and heave

speeds and the yaw angle are controlled by using PID controllers. The input signal of the controller is generated from the guidance system. There are many guidance algorithms to bring the vehicle to a desired position. The most common algorithm is the line-of-sight (LOS) guidance [3]. The environmental distributions such as currents, wind and waves effects the guidance performance. Integral LOS guidance is performed both in the constant ocean current and in the environmental distribution [12] and [8]. In this thesis, the way point guidance by line of sight and way point guidance based optimal control are studied.

1.3 SAGA

The unmanned underwater survey vehicle (SAGA) used in this thesis is a remotely operated underwater survey vehicle specifically developed for the purpose of investigation of underwater and equipped with a camera and a two dimensional sonar in addition to several other custom specific sensors as seen in Fig. 1.3. It is very easy to obtain navigational data and high resolution video, as regards to underwater operation, from this vehicle [15]. It consists of three basic parts; cable, operator console and vehicle's body. The cable provides data transmission and power transmission between the vehicle and the operator console. The vehicle is controlled and the data from the vehicle is observed by the operator console. The properties of SAGA is shown in Table 1.1.

Table 1.1: SAGA properties

Length	420 mm
Width	330 mm
Height	270 mm
Weight in air	10 kg
Max. operation depth	250 m
Max. surge speed	3 knots
Volume	0.01
Thruster configuration	2 forward 1 vertical



Figure 1.3: Hull of SAGA, unmanned underwater survey vehicle [15]

1.4 Organization of the Thesis

Chapter 1 gives the information about history and application area of an unmanned underwater vehicles and literature survey about the scope of this thesis and it mentions about SAGA.

Chapter 2 explains the mathematical model of unmanned underwater vehicle. Kinematic and rigid body dynamic parts of an underwater vehicle are explained. The motion of an underwater vehicle is defined in 6 DOF. Hydrodynamic forces and moments are explained. The equations of motion of SAGA is derived.

Chapter 3 consists of the thruster model of SAGA, autopilot design of SAGA and an analysis of the nonlinear system response. The nonlinear mathematical model of SAGA is implemented in Matlab/Simulink environment and the system response is analyzed with different tests by activating different thrusters. In addition, PID controller design for translational and rotational velocity and position are explained in this chapter.

Chapter 4 gives information how the navigation problem of SAGA is solved. The inertial navigation system, acoustic-based navigation system, vision-based navigation

systems are explained. Inertial navigation processor and inertial navigation equations are given. System model based on the inertial navigation system and measured model are obtained for the integrated navigation system. The navigation solution is obtained with the design of the integrated navigation architecture by Kalman filter algorithm.

Chapter 5 includes the guidance algorithm of SAGA. The guidance of SAGA is composed of the way point guidance with LOS and the optimal guidance.

Chapter 6 presents the acoustic-based navigation experiment of SAGA at the pool of the Middle East Technical University (METU). The experimental navigation data obtained from the acoustic based measurement system is integrated into the measured data which comes from the inertial navigation system and the depth sensor. System states are estimated by a Kalman filter algorithm.

Chapter 7 explains how to obtain the unknown parameters of the mathematical model of SAGA. First, the navigation data is generated from simulation-based model to be used in the system identification study for the uncoupled and coupled motions. Then, the real navigation data of SAGA which was obtained in Chapter 6 is used for the system identification study of the coupled motion. Finally, system responses with and without the system identification study are compared.

Chapter 8 summarizes this thesis and comments on the results of the thesis. In addition, it gives possible future directions as a continuation of this work.

CHAPTER 2

MATHEMATICAL MODELLING

2.1 Introduction

Modeling of an underwater vehicle has two main parts, statics and dynamics study. While statics is associated with bodies at constant velocity, dynamics is associated with bodies having accelerated motion. The motion of an underwater vehicle is determined in 6 DOF since 6 independent coordinates are required to determine the position and orientation of a rigid body. Table 2.1 shows notations used in mathematical modeling of an underwater vehicles. The first three coordinates and their time derivatives are used to illustrate the position and translational motion along x , y and z axes. The orientation and rotational motion are determined using the last 3 coordinates and their derivatives. The six different motions are determined for underwater vehicles such as surge, sway, heave, roll, pitch and yaw [18].

Table 2.1: Notation used for underwater vehicles

DOF		Forces and Moments	Linear and Angular Velocities	Positions and Euler Angles
1	motions in the x-direction (surge)	X	u	x
2	motions in the y-direction (sway)	Y	v	y
3	motions in the z-direction (heave)	Z	w	z
4	rotation about the x-axis (roll)	K	p	ϕ
5	rotation about the y-axis (pitch)	M	q	θ
6	rotation about the z-axis (yaw)	N	r	ψ

2.2 Kinematics

2.2.1 Notation of Kinematics Quantities

Most of kinematic quantities such as position, velocity, acceleration, and angular rate, involve three coordinate frames [20].

- object frame: The frame whose motion is described, α ;
- reference frame: The frame with which that motion is respect to, β ;
- resolving frame: The set of axes in which that motion is represented, γ .

The notation is used as $x_{\beta\alpha}^{\gamma}$. The vector, x , refers to a kinematic property of frame α with respect to frame β , expressed in the frame γ axes.

2.2.2 Coordinate Frames

A coordinate frame can be defined in two ways. First, it provides an origin and a set of axes in terms of which the motion of objects is described. Second, it defines the position and orientation of an object. To determine the motion of the vehicle in 6 DOF, there are two main coordinate frames such as body-fixed and earth-fixed coordinate frames as shown in Fig 2.1. The position and attitude of the vehicle are defined with respect to the earth frame. The linear and angular velocities of the vehicle are defined related to the body-fixed frame. To solve the navigation problem, there are many coordinate frames such as Earth-Centered Inertial Frame, Earth-Centered Earth-Fixed Frame, Local Navigation Frame and Body-Fixed Frame. Earth-Centered Earth-Fixed Frame is chosen as reference and resolving frames in this thesis [20]. All axes of ECEF frame are fixed with respect to the Earth. The ECEF frame is denoted as e . Body-fixed coordinate frame is denoted as b , $X_b Y_b Z_b$ and the origin of the body-fixed coordinate frame is chosen as the CG as shown in Figure 2.1 [18].

For underwater vehicles, body axes X_b , Y_b and Z_b correspond to the *principal axes of inertia*, and are defined as [18]:

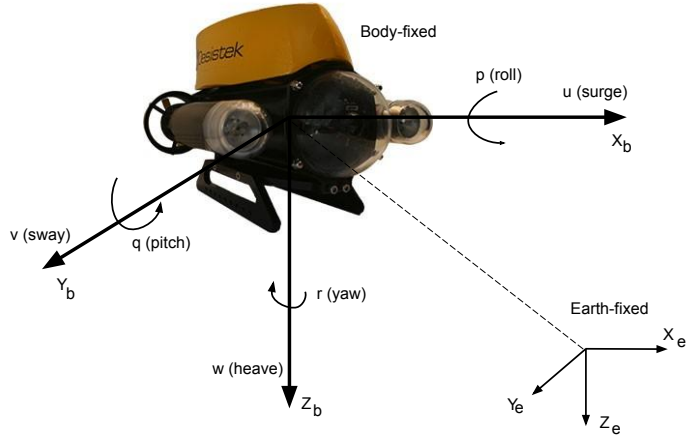


Figure 2.1: Body-fixed and earth-fixed reference frame

X_b - longitudinal axis (directed from aft to fore)

Y_b - transverse axis (directed to starboard)

Z_b - normal axis (directed from top to bottom)

The motion of the body-fixed coordinate frame is defined related to an inertial reference frame. The earth-fixed coordinate frame, $X_e Y_e Z_e$ is also considered to be inertial since motion of the Earth scarcely effects low speed underwater vehicle. When the moving, body-fixed, coordinate frame with origin O , $X_b Y_b Z_b$ rotates with angular velocity around an earth-fixed coordinate frame $X_e Y_e Z_e$, the body's inertia tensor is defined [18]:

$$I_0 \triangleq \begin{bmatrix} I_x & -I_{xy} & -I_{xz} \\ -I_{yx} & I_y & -I_{yz} \\ -I_{zx} & -I_{zy} & I_z \end{bmatrix} \quad (2.1)$$

where, I_x, I_y, I_z are moments of inertia about $X_O Y_O Z_O$ axes and $I_{xy} = I_{yx}$, $I_{xz} = I_{zx}$, $I_{yz} = I_{zy}$ are products of inertia. They depend on the mass of the body and its geometry.

The general motion of an underwater vehicle in 6 DOF is described related to SNAME

notation by the following vectors as [18]:

$$\vec{\eta} = [x \ y \ z \ \phi \ \theta \ \psi]^T \vec{\eta}_1 = [x \ y \ z]^T \vec{\eta}_2 = [\phi \ \theta \ \varphi]^T \quad (2.2)$$

$$\vec{v} = [u \ v \ w \ p \ q \ r]^T \vec{v}_1 = [u \ v \ w]^T \vec{v}_2 = [p \ q \ r]^T \quad (2.3)$$

$$\vec{\tau} = [X \ Y \ Z \ K \ M \ N]^T \vec{\tau}_1 = [X \ Y \ Z]^T \vec{\tau}_2 = [K \ M \ N]^T \quad (2.4)$$

where

η_1 : The position vector in the earth fixed frame,

η_2 : The orientation vector in the earth fixed frame,

η : The position and orientation vector in the earth fixed frame,

v_1 : The linear velocity vector in the body-fixed frame,

v_2 : The angular velocity vector in the body-fixed frame,

v : The linear and angular velocity vector in the body-fixed frame,

τ_1 : The forces act on the vehicle in the body-fixed frame,

τ_2 : The moments act on the vehicle in the body-fixed frame,

τ : The forces and moments act on the vehicle in the body-fixed frame.

2.2.3 Euler Angles

Euler angles, roll, pitch, yaw is the ideal way of the describing the attitude. The attitude is composed of three rotations. It is defined by the transformation of a vector $x = (x, y, z)$ from resolving axes, β to an α frame. The first rotation, $\varphi_{\beta\alpha}$, is the yaw rotation. The x and y components of the vector rotate with yaw angle around the common z axes of the frames, α and β as shown in Fig. 2.2.

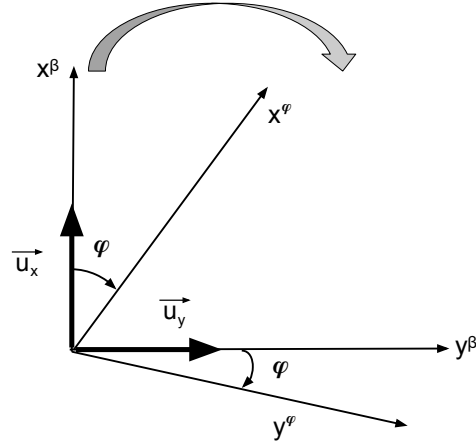


Figure 2.2: Euler angle rotation in z axes

$$\begin{aligned}
 x^\varphi &= x^\beta \cos \varphi_{\beta\alpha} \vec{u}_x + y^\beta \sin \varphi_{\beta\alpha} \vec{u}_y \\
 y^\varphi &= -x^\beta \sin \varphi_{\beta\alpha} \vec{u}_x + y^\beta \cos \varphi_{\beta\alpha} \vec{u}_y \\
 z^\varphi &= z^\beta
 \end{aligned} \tag{2.5}$$

Thus, the rotation transformation matrix related to yaw rotation is obtained as

$$C_{z,\varphi} = \begin{bmatrix} \cos\varphi & \sin\varphi & 0 \\ -\sin\varphi & \cos\varphi & 0 \\ 0 & 0 & 1 \end{bmatrix} \tag{2.6}$$

Second rotation is the pitch rotation. x and z components of the vector rotates with pitch angle around common y axes of α and β frames as shown in Fig. 2.3.

$$\begin{aligned}
 x^\theta &= x^\varphi \cos \theta_{\beta\alpha} \vec{u}_x - z^\varphi \sin \theta_{\beta\alpha} \vec{u}_z \\
 y^\theta &= y^\varphi \\
 z^\theta &= x^\varphi \sin \theta_{\beta\alpha} \vec{u}_x + z^\varphi \cos \theta_{\beta\alpha} \vec{u}_z
 \end{aligned} \tag{2.7}$$

The transformation matrix of the pitch rotation is obtained as

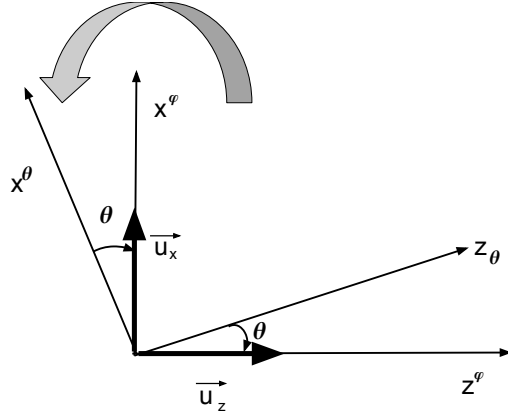


Figure 2.3: Euler angle rotation in y axes

$$C_{y,\theta} = \begin{bmatrix} \cos\theta & 0 & -\sin\theta \\ 0 & 1 & 0 \\ \sin\theta & 0 & \cos\theta \end{bmatrix} \quad (2.8)$$

Finally, the roll rotation, $\phi_{\beta\alpha}$, is performed. The y and z components of the vector rotate with roll angle around common x axes of these frames as shown in Fig. 2.4

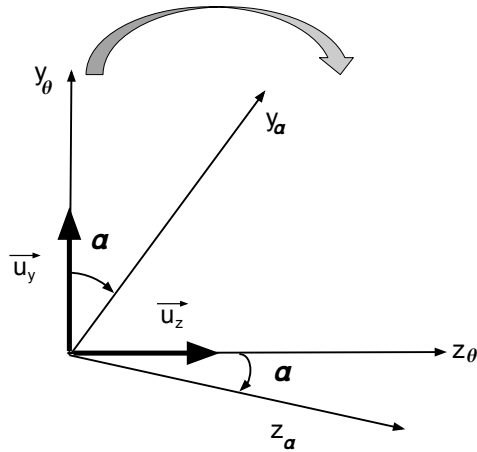


Figure 2.4: Euler angle rotation in x axes

$$\begin{aligned} x^\alpha &= x^\theta \\ y^\alpha &= y^\theta \cos \phi_{\beta\alpha} + z^\theta \sin \phi_{\beta\alpha} \\ z^\alpha &= -y^\theta \sin \phi_{\beta\alpha} + z^\theta \cos \phi_{\beta\alpha} \end{aligned} \quad (2.9)$$

The transformation matrix of the roll rotation is obtained as

$$C_{x,\theta} = \begin{bmatrix} 1 & 0 & 0 \\ 0 & \cos\phi & \sin\phi \\ 0 & -\sin\phi & \cos\phi \end{bmatrix} \quad (2.10)$$

Euler rotation from frame β to frame α is represented by the vector

$$\Psi_{\beta\alpha} = \begin{bmatrix} \phi_{\beta\alpha} \\ \theta_{\beta\alpha} \\ \varphi_{\beta\alpha} \end{bmatrix} \quad (2.11)$$

Reversing the sign of the Euler angles does not return to the original orientation

$$\begin{bmatrix} \phi_{\beta\alpha} \\ \theta_{\beta\alpha} \\ \varphi_{\beta\alpha} \end{bmatrix} \neq \begin{bmatrix} -\phi_{\beta\alpha} \\ -\theta_{\beta\alpha} \\ -\varphi_{\beta\alpha} \end{bmatrix} \quad (2.12)$$

Euler angles which are roll, pitch and yaw are used in order to transform from the body-fixed frame to the earth fixed frame and vice versa. It is described by the following vector.

$$\eta_2 = [\phi, \theta, \psi]^T \quad (2.13)$$

The body-fixed linear velocity vector $v_1 = [u, v, w]^T$ and the position rate vector $\dot{\eta}_1 = [\dot{x}, \dot{y}, \dot{z}]^T$ are related to coordinate transformation matrix $C_b^e(\eta_2)$ as follow:

$$\dot{\eta}_1 = C_b^e(\eta_2) v_1 \quad (2.14)$$

where

$$C_b^e(\eta_2) = \begin{bmatrix} c\psi c\theta & -s\psi c\phi + c\psi s\theta s\phi & s\psi s\phi + c\psi c\phi s\theta \\ s\psi c\theta & c\psi c\phi + s\phi s\theta s\psi & -c\psi s\phi + s\theta s\psi c\phi \\ -s\theta & c\theta s\phi & c\theta c\phi \end{bmatrix} \quad (2.15)$$

The orientation in the earth-fixed frame can be obtained by angular velocity transformation as

$$\dot{\eta}_2 = T_b^e(\eta_2) v_2 \quad (2.16)$$

where

$$v_2 = [p, q, r]^T \quad (2.17)$$

$$\dot{\eta}_2 = [\dot{\phi}, \dot{\theta}, \dot{\psi}]^T \quad (2.18)$$

$$T_b^e(\eta_2) = \begin{bmatrix} 1 & s\phi t\theta & c\phi t\theta \\ 0 & c\phi & -s\phi \\ 0 & -s\phi/c\theta & c\phi/c\theta \end{bmatrix} \quad (2.19)$$

For a pitch angle, θ , is equal to $\mp 90^\circ$, the transformation matrix $T_b^e(\eta_2)$ is undefined. But, because of the mechanical design of SAGA, pitch angle cannot be equal to $\mp 90^\circ$.

2.3 Rigid Body Dynamics

The nonlinear dynamic equation of motion in 6 DOF are defined as [18]:

$$\begin{aligned} M\dot{v} + C(v)v + D(v)v + g(\eta) &= \tau \\ \dot{\eta} &= J(\eta)v \end{aligned} \quad (2.20)$$

where

M : Inertia matrix, including added mass,

$C(v)$: Matrix of Coriolis and centripetal terms, including added mass,

$D(v)$: Damping matrix,

$g(\eta)$: Gravitational forces and moments vector ,

τ : Control inputs vector.

The rigid body equations of motions, translational and rotational, are derived by using Newton's second law taking Euler's first and second axioms. Translational motion equation is derived by using the linear momentum formula, p_c and rotational motion

equation is derived by using the angular momentum formula, h_c .

$$\dot{p}_c = \tau_1 \quad p_c = mv_1 \quad (2.21)$$

$$\dot{h}_c = \tau_2 \quad h_c = I_c v_2 \quad (2.22)$$

where $\tau_1 = [X, Y, Z]^T$ are forces and $\tau_2 = [K, M, N]^T$ are moments related to body's center of gravity. v_1, v_2 are linear and angular velocity vector respectively. So, the rigid-body equations of translational and rotational motion in 6 DOF are obtained, where the coordinates of the center of gravity, r_G , are given by x_G, y_G and z_G .

$$\begin{aligned} X &= m(\dot{u} - vr + wq - x_G(q^2 + r^2) + y_G(pq - \dot{r}) + z_G(pr + \dot{q})) \\ Y &= m(\dot{v} - wp + ur - x_G(qp + \dot{r}) - y_G(r^2 + p^2) + z_G(qr - \dot{p})) \\ Z &= m(\dot{w} - uq + vp + x_G(rp - \dot{q}) - y_G(rq + \dot{p}) + z_G(p^2 + q^2)) \end{aligned} \quad (2.23)$$

$$\begin{aligned} K &= I_x \dot{p} - I_{xy} \dot{q} - I_{xz} \dot{r} - qI_{zx}p - q^2 I_{zy} + I_z r q + I_{yx} p r - I_y q r + I_{yz} r^2 \\ &\quad + m(y_G p v - y_G q u + y_G \dot{w} + z_G p w - z_G r u - z_G \dot{v}) \\ M &= I_y \dot{q} - I_{yx} \dot{p} - I_{yz} \dot{r} + p^2 I_{zx} + I_{zy} q p - I_z r p + I_x p r - I_{xy} q r - r^2 I_{xz} \\ &\quad + m(-x_G p v + x_G q u - x_G \dot{w} + z_G q w - z_G r u + \dot{u} z_G) \\ N &= I_z \dot{r} - I_{zy} \dot{q} - I_{zx} \dot{p} + p^2 I_{yx} + p q I_y - p r I_{yz} - q I_x p + q^2 I_{xy} + q r I_{xz} \\ &\quad + m(-x_G p w + x_G r u + x_G \dot{v} - y_G q w + y_G r v - \dot{u} y_G) \end{aligned} \quad (2.24)$$

These equations of the translational and rotational motions are explained in a more compact form as:

$$M_{RB} \dot{v} + C_{RB}(v)v = \tau_{RB} \quad (2.25)$$

where

τ_{RB} : The generalized vector of external forces and moments act on the vehicle,

v : The linear and angular velocity vector in the body-fixed frame,

M_{RB} : The rigid body inertia matrix,

C_{RB} : The rigid body Coriolis and centripetal matrix.

M_{RB} is defined as [18]:

$$M_{RB} = \begin{bmatrix} m & 0 & 0 & 0 & mz_G & -my_G \\ 0 & m & 0 & -mz_G & 0 & mx_G \\ 0 & 0 & m & my_G & -mx_G & 0 \\ 0 & -mz_G & my_G & I_x & -I_{xy} & -I_{xz} \\ mz_G & 0 & -mx_G & -I_{yx} & I_y & -I_{yz} \\ -my_G & mx_G & 0 & -I_{zx} & -I_{zy} & I_z \end{bmatrix} \quad (2.26)$$

C_{RB} is defined as [18]:

$$C_{RB} = \begin{pmatrix} 0 & 0 & 0 \\ 0 & 0 & 0 \\ 0 & 0 & 0 \\ -m(y_G q + rz_G) & m(y_G p + w) & m(pz_G - v) \\ m(x_G q - w) & -m(rz_G + x_G p) & m(qz_G + u) \\ m(x_G r + v) & m(y_G r - u) & -m(x_G p + y_G q) \\ m(rz_G + qy_G) & -m(x_G q - w) & -m(x_G r + v) \\ -m(y_G p + w) & m(rz_G + x_G p) & m(y_G r - u) \\ -m(pz_G - v) & -m(u + qz_G) & m(qy_G + x_G p) \\ 0 & -qI_{yz} - I_{xz}p + rI_z & I_{xy}p - qI_y + rI_{yz} \\ qI_{yz} + I_{xz}p - rI_z & 0 & -I_{xz}r - I_{xy}q + pI_x \\ -I_{xy}p + qI_y - rI_{yz} & I_{xz}r + I_{xy}q - pI_x & 0 \end{pmatrix} \quad (2.27)$$

2.4 Hydrodynamic Forces and Moments

Hydrodynamic forces and moments are composed of radiation-induced forces and Froude-Kriloff and diffraction forces. The radiation-induced forces and moments are caused by added mass, restoring forces due to Archimedes and hydrodynamic

damping. The Froude-Kriloff and diffraction forces are caused by environmental forces such as waves, wind and currents [18].

The total external forces and moments acting on the vehicle are represented as

$$\tau_{RB} = \tau_H + \tau_E + \tau \quad (2.28)$$

where τ is the propulsion forces and moments, τ_E is represented environmental forces and moments and τ_H is hydrodynamic forces and moments. Hydrodynamic forces and moments are defined as

$$\tau_H = -M_A \dot{v} - C_A(v)v - D(v)v - g(\eta) \quad (2.29)$$

where, the terms of $(-M_A \dot{v} - C_A(v)v)$ is due to added mass, $g(\eta)$ is due to restoring forces and $D(v)v$ is hydrodynamic damping.

Substitution of Equation (2.29) into Equation (2.28) together with Equation (2.25) results in the dynamic equation of motion in the 6 DOF as follows [18].

$$M\dot{v} + C(v)v + D(v)v + g(\eta) = \tau_E + \tau \quad (2.30)$$

where

$$M \triangleq M_{RB} + M_A \quad C(v) \triangleq C_{RB}(v) + C_A(v) \quad (2.31)$$

2.4.1 Added Mass and Inertia

The added mass terms should be understood as pressure-induced forces and moments due to a forced motion of the body which are proportional to the acceleration of the body. The added mass forces and moments are derived using the fluid kinetic energy, T_A which can be written a quadratic form of the body axis velocity vector components [18] as

$$T_A = \frac{1}{2} v^T M_A v \quad (2.32)$$

where M_A is a 6×6 the added mass inertia matrix expressed as follow [18]:

$$M_A = - \begin{bmatrix} X_{\dot{u}} & X_{\dot{v}} & X_{\dot{w}} & X_{\dot{p}} & X_{\dot{q}} & X_{\dot{r}} \\ Y_{\dot{u}} & Y_{\dot{v}} & Y_{\dot{w}} & Y_{\dot{p}} & Y_{\dot{q}} & Y_{\dot{r}} \\ Z_{\dot{u}} & Z_{\dot{v}} & Z_{\dot{w}} & Z_{\dot{p}} & Z_{\dot{q}} & Z_{\dot{r}} \\ K_{\dot{u}} & K_{\dot{v}} & K_{\dot{w}} & K_{\dot{p}} & K_{\dot{q}} & K_{\dot{r}} \\ M_{\dot{u}} & M_{\dot{v}} & M_{\dot{w}} & M_{\dot{p}} & M_{\dot{q}} & M_{\dot{r}} \\ N_{\dot{u}} & N_{\dot{v}} & N_{\dot{w}} & N_{\dot{p}} & N_{\dot{q}} & N_{\dot{r}} \end{bmatrix} \quad (2.33)$$

Z_A represents hydrodynamic added mass force along z -axis due to an acceleration \dot{w} in the z direction can be written as:

$$Z_A = Z_{\dot{w}}\dot{w} \quad (2.34)$$

where

$$Z_{\dot{w}} \triangleq \frac{\delta Z}{\delta \dot{w}} \quad (2.35)$$

The added mass forces and moments are separated in the added inertia matrix, M_A defined in (2.33) and matrix of hydrodynamic Coriolis and centripetal terms, $C_A(v)$ defined in (2.36) [18].

$$C_A(v) = \begin{bmatrix} 0 & 0 & 0 & 0 & -a_3 & a_2 \\ 0 & 0 & 0 & a_3 & 0 & -a_1 \\ 0 & 0 & 0 & -a_2 & a_1 & 0 \\ 0 & -a_3 & a_2 & 0 & -b_3 & b_2 \\ a_3 & 0 & -a_1 & b_3 & 0 & -b_1 \\ -a_2 & a_1 & 0 & -b_2 & b_1 & 0 \end{bmatrix} \quad (2.36)$$

where

$$\begin{aligned} a_1 &= X_{\dot{u}}u + X_{\dot{v}}v + X_{\dot{w}}w + X_{\dot{p}}p + X_{\dot{q}}q + X_{\dot{r}}r \\ a_2 &= X_{\dot{v}}u + Y_{\dot{v}}v + Y_{\dot{w}}w + Y_{\dot{p}}p + Y_{\dot{q}}q + Y_{\dot{r}}r \\ a_3 &= X_{\dot{w}}u + Y_{\dot{w}}v + Z_{\dot{w}}w + Z_{\dot{p}}p + Z_{\dot{q}}q + Z_{\dot{r}}r \\ b_1 &= X_{\dot{p}}u + Y_{\dot{p}}v + Z_{\dot{p}}w + K_{\dot{p}}p + K_{\dot{q}}q + K_{\dot{r}}r \\ b_2 &= X_{\dot{q}}u + Y_{\dot{q}}v + Z_{\dot{q}}w + K_{\dot{q}}p + M_{\dot{q}}q + M_{\dot{r}}r \\ b_3 &= X_{\dot{r}}u + Y_{\dot{r}}v + Z_{\dot{r}}w + K_{\dot{r}}p + M_{\dot{r}}q + N_{\dot{r}}r \end{aligned} \quad (2.37)$$

The added mass parameters can be obtained from some hydrodynamic software programs such as WAMIT, VERES and SEAWAY and SOLIDWORKS. If the structure of the vehicle has some symmetry with respect to pitch and yaw planes, added mass parameters can be obtained approximately using the strip theory [18]. For more accuracy, values of these parameters can be improved by a system identification study based on the navigational data from a pool experiment.

In many ROV applications the vehicle will usually moves at low speeds. If the vehicle also has three planes of symmetry, this suggests that we can neglect the contributions from the off-diagonal elements in the added inertia matrix M_A . Also, it is assumed that the vehicle is designed ellipsoidal shape represented semi-major, a , semi-minor, b , and semi-vertical c axes which are defined as in [18].

$$\frac{x^2}{a^2} + \frac{y^2}{b^2} + \frac{z^2}{c^2} = 1 \quad (2.38)$$

The diagonal added mass terms are obtained as follow equations by letting $b = c$ and $a > b$ [18].

$$X_{\dot{u}} = -\frac{\alpha_0}{2 - \alpha_0}m \quad (2.39)$$

$$Y_{\dot{v}} = Z_{\dot{w}} = -\frac{\beta_0}{2 - \beta_0} \quad (2.40)$$

$$K_{\dot{p}} = 0 \quad (2.41)$$

$$N_{\dot{r}} = M_{\dot{q}} = -\frac{1}{5} \frac{(b^2 - a^2)^2(\alpha_0 - \beta_0)}{2(b^2 - a^2) + (b^2 + a^2)(\beta_0 - \alpha_0)}m \quad (2.42)$$

where

$$\alpha_0 = \frac{2(1 - e^2)}{e^3} \left(\frac{1}{2} \ln \frac{1 + e}{1 - e} - e \right) \quad (2.43)$$

$$\beta_0 = \frac{1}{e^2} - \frac{1 - e^2}{2e^3} \ln \frac{1 + e}{1 - e} \quad (2.44)$$

$$e = 1 - \left(\frac{b}{a} \right)^2 \quad (2.45)$$

2.4.2 Hydrodynamic Damping

The hydrodynamic damping for ocean vehicles is caused by potential damping, skin friction, wave drift damping and damping due to vortex shedding. Potential damping consists of surface waves. These waves are high frequency waves with small wave length. Wave drift damping occurs while the vehicle moves on the surface of the sea. Potential and wave damping effects are neglected since the vehicle operates in deep water. Skin friction caused by ow of water around the boundary of vehicle. Damping due to the skin friction are modeled is linear and quadratic damping in (2.46) [18].

$$D_{skin}(v) = D_{linear} + D_{quadratic}(v) \quad (2.46)$$

Damping due to vortex shedding occurs because of the pressure differences on the ow path of water and it is modeled in (2.47). It is proportional to projected sectional area of the vehicle and with square of velocity,

$$D_{vortex} = -\frac{1}{2}\rho C_D(Rn) A |v| v \quad (2.47)$$

where v is the vehicle velocity, A is the projected cross-sectional area, $C_D(Rn)$ is drag-coefficient depends on Reynolds number, Rn and ρ is the water density.

After all, the total drag acting on the vehicle is expressed as [18]:

$$D_M(v) = - \begin{bmatrix} X_u + X_{|u|u}|u| & X_v + X_{|v|v}|v| & X_w + X_{|w|w}|w| & X_p + X_{|p|p}|p| & X_q + X_{|q|q}|q| & X_r + X_{|r|r}|r| \\ Y_u + Y_{|u|u}|u| & Y_v + Y_{|v|v}|v| & Y_w + Y_{|w|w}|w| & Y_p + Y_{|p|p}|p| & Y_q + Y_{|q|q}|q| & Y_r + Y_{|r|r}|r| \\ Z_u + Z_{|u|u}|u| & Z_v + Z_{|v|v}|v| & Z_w + Z_{|w|w}|w| & Z_p + Z_{|p|p}|p| & Z_q + Z_{|q|q}|q| & Z_r + Z_{|r|r}|r| \\ K_u + K_{|u|u}|u| & K_v + K_{|v|v}|v| & K_w + K_{|w|w}|w| & K_p + K_{|p|p}|p| & K_q + K_{|q|q}|q| & K_r + K_{|r|r}|r| \\ M_u + M_{|u|u}|u| & M_v + M_{|v|v}|v| & M_w + M_{|w|w}|w| & M_p + M_{|p|p}|p| & M_q + M_{|q|q}|q| & M_r + M_{|r|r}|r| \\ N_u + N_{|u|u}|u| & N_v + N_{|v|v}|v| & N_w + N_{|w|w}|w| & N_p + N_{|p|p}|p| & N_q + N_{|q|q}|q| & N_r + N_{|r|r}|r| \end{bmatrix} \quad (2.48)$$

2.4.3 Restoring Forces and Moments

Restoring forces and moments composed of gravitational and buoyant forces. The gravitational force, f_G is defined in the body-fixed coordinate frame in (2.49). It acts

through center of gravity $r_G = [x_G, y_G, z_G]^T$ of the vehicle.

$$f_G(\eta_2) = J_1^{-1}(\eta_2) \begin{bmatrix} 0 \\ 0 \\ W \end{bmatrix} \quad (2.49)$$

where W is weight of vehicle's body defined as $W = mg$ letting m , the mass of the vehicle, g , the acceleration of gravity and $J_1(\eta_2)$ is Euler angle coordinate transformation matrix.

The buoyant force is defined in the body-fixed coordinate system in (2.50). It acts through the center of buoyancy $r_B = [x_B, y_B, z_B]^T$.

$$f_B(\eta_2) = -J_1^{-1}(\eta_2) \begin{bmatrix} 0 \\ 0 \\ B \end{bmatrix} \quad (2.50)$$

B is buoyancy force defined as $B = \rho g \nabla$, letting ρ be the fluid density, ∇ be the volume of the fluid displaced by the vehicle.

The restoring force and moment vector in the body-fixed coordinate system is:

$$g(\eta) = - \begin{bmatrix} f_G(\eta) + f_B(\eta) \\ r_G \times f_G(\eta) + r_B \times f_B(\eta) \end{bmatrix} \quad (2.51)$$

Equation (2.51) is expanded as:

$$g(\eta) = \begin{bmatrix} (W - B)s\theta \\ -(W - B)c\theta s\phi \\ -(W - B)c\theta c\phi \\ -c\theta c\phi(y_G W - y_B B) + c\theta s\phi(-z_G W + z_B B) \\ -c\theta c\phi(-x_G W + x_B B) + s\theta(-z_G W + z_B B) \\ -c\theta s\phi(x_G W - x_B B) + s\theta(y_G W - y_B B) \end{bmatrix} \quad (2.52)$$

2.5 Equations of Motion

The nonlinear equations of motion for SAGA in the body-fixed frame are written as:

$$\begin{aligned} M\dot{v} + C(v)v + D(v)v + g(\eta) &= \tau \\ \dot{\eta} &= J(\eta)v \end{aligned} \quad (2.53)$$

$$M \triangleq M_{RB} + M_A \quad C(v) \triangleq C_{RB}(v) + C_A(v) \quad (2.54)$$

The rigid body mass is a diagonal matrix since the vehicle is assumed to have three symmetry planes. The off-diagonal contributions are neglected. The simplified rigid body mass matrix of SAGA is defined as

$$M_{RB} = \begin{bmatrix} m & 0 & 0 & 0 & 0 & 0 \\ 0 & m & 0 & 0 & 0 & 0 \\ 0 & 0 & m & 0 & 0 & 0 \\ 0 & 0 & 0 & I_x & 0 & 0 \\ 0 & 0 & 0 & 0 & I_y & 0 \\ 0 & 0 & 0 & 0 & 0 & I_z \end{bmatrix} \quad (2.55)$$

For completely submerged vehicles M_A will always be strictly positive, that is, $M_A > 0$. In many ROV applications the vehicle will usually moves at low speeds. If the vehicle also has three planes of symmetry, this suggests that we can neglect the contributions from the off-diagonal elements in the added inertia matrix M_A . Hence, the following simple expressions for M_A and C_A are obtained for SAGA as:

$$M_A = - \begin{bmatrix} X & 0 & 0 & 0 & 0 & 0 \\ 0 & Y & 0 & 0 & 0 & 0 \\ 0 & 0 & Z & 0 & 0 & 0 \\ 0 & 0 & 0 & K & 0 & 0 \\ 0 & 0 & 0 & 0 & M & 0 \\ 0 & 0 & 0 & 0 & 0 & N \end{bmatrix} \quad (2.56)$$

$$C_A(v) = \begin{bmatrix} 0 & 0 & 0 & 0 & -Z_{\dot{w}}w & Y_{\dot{v}}v \\ 0 & 0 & 0 & Z_{\dot{w}}w & 0 & -X_{\dot{u}}u \\ 0 & 0 & 0 & -Y_{\dot{v}}v & X_{\dot{u}}u & 0 \\ 0 & -Z_{\dot{w}}w & Y_{\dot{v}}v & 0 & -N_{\dot{r}}r & M_{\dot{q}}q \\ Z_{\dot{w}}w & 0 & -X_{\dot{u}}u & N_{\dot{r}}r & 0 & 0 \\ -Y_{\dot{v}}v & X_{\dot{u}}u & 0 & -M_{\dot{q}}q & 0 & 0 \end{bmatrix} \quad (2.57)$$

The moving weather in the surface of the rotating earth causes water to veer to right (clockwise) in the northern hemisphere and to the left (anticlockwise) in the southern hemisphere. This effect is known as the Coriolis force. The Coriolis and centripetal force matrix of SAGA is the sum of the rigid body and hydrodynamic Coriolis and centripetal matrices.

$$C(v) \triangleq C_{RB}(v) + C_A(v) \quad (2.58)$$

The rigid body Coriolis and centripetal matrix is related to vehicle's speed and it is defined as

$$C_{RB} = \begin{bmatrix} 0 & 0 & 0 & 0 & m(w) & -m(v) \\ 0 & 0 & 0 & m(-w) & 0 & m(u) \\ 0 & 0 & 0 & m(v) & m(-u) & 0 \\ 0 & m(w) & -m(v) & 0 & I_z r & -I_y q \\ m(-w) & 0 & m(u) & -I_z r & 0 & 0 \\ m(v) & m(-u) & 0 & I_y q & 0 & 0 \end{bmatrix} \quad (2.59)$$

The damping force matrix is assumed consisting of only linear terms since the vehicle will only be able to move at low speeds. The contribution of quadratic damping terms is neglected since the effect of the quadratic damping terms is important at higher speeds. Hence, the following simple expressions is obtained for SAGA as

$$D(v) = - \begin{bmatrix} X_u & 0 & 0 & 0 & 0 & 0 \\ 0 & Y_v & 0 & 0 & 0 & 0 \\ 0 & 0 & Z_w & 0 & 0 & 0 \\ 0 & 0 & 0 & K_p & 0 & 0 \\ 0 & 0 & 0 & 0 & M_q & 0 \\ 0 & 0 & 0 & 0 & 0 & N_r \end{bmatrix} \quad (2.60)$$

The restoring force and moment matrix is defined as in Equation 2.52.

In the nonlinear mathematical modeling of the vehicle, u is the column matrix which consists of moments and forces produced from thrusters will be given in Chapter 3.

2.6 Conclusion

In this chapter, the mathematical modeling of an unmanned underwater survey vehicle is obtained. Kinematics and dynamics of the model are explained. The coordinate transformation matrix is obtained using the ZYX rotation. The inertia matrix of the SAGA is defined as a diagonal matrix. The rigid body mass and Coriolis matrices are obtained with the added mass parameters. The damping forces on the vehicle are defined and the damping matrix is obtained with linear damping coefficients. Restoring forces matrix is defined for the SAGA. The nonlinear equations of motion for the SAGA are obtained after the all matrices that build the mathematical model are defined.

CHAPTER 3

AUTOPILOT

3.1 Introduction

In this chapter, the nonlinear mathematical model of SAGA is implemented in MATLAB/Simulink environment. Since the system input of the model is the force value produced from thrusters, the thruster model is explained. Then, the system response is analyzed with different tests by activating different thrusters. The surge, heave speed and rotational speed bring the angle of yaw which are controlled by a PID controller. In addition, the depth and the yaw angle are controlled also by a PID controller.

3.2 Thruster Model

The hardware elements of the motor controller-motor-propeller are collected in one place and it is called the thruster shown in Fig. 3.1. Each thruster is driven by a DC motor. The dynamic equations of the motors are given [38] as:

$$L_a \frac{d}{dt} i_a = - R_a i_a - 2\pi K_M n + u_a \quad (3.1)$$

$$2\pi J_m \frac{d}{dt} n = K_M i_a - Q(n, V_a) \quad (3.2)$$

where

L_a : Inductance of the rotor,



Figure 3.1: Thruster (composed of motor controller-motor-propeller)

R_a : Resistance of the rotor,

u_a : Voltage of the rotor,

K_M : Torque constant of the motor,

i_a : Rotor current,

J_m : Inertial moment of the motor,

n : Rotational speed of the motor,

$Q(n, V_a)$: Torque of the propeller.

There is a reference PWM value for each motor. Motor is stopped when PWM value reaches the value of 1500 rpm. If the applied PWM value is the higher than 1500 rpm, motor rotates positive direction. If the applied PWM value is the lower than the 1500 rpm, motor rotates the opposite direction. Since the system input for mathematical model of SAGA is force value (Nm) of each thruster, applied PWM values are transformed to the force values. The relationship between the force (Kgf) value and the PWM value of the used motors is shown in Fig. 3.2 [15].

SAGA has three thrusters. Two of which are located horizontally, at right and left sides as shown in Fig. 3.3. The distance between center of gravity and right thruster, r_1 , is equal to the distance between the center of gravity and the left thruster, r_2 .

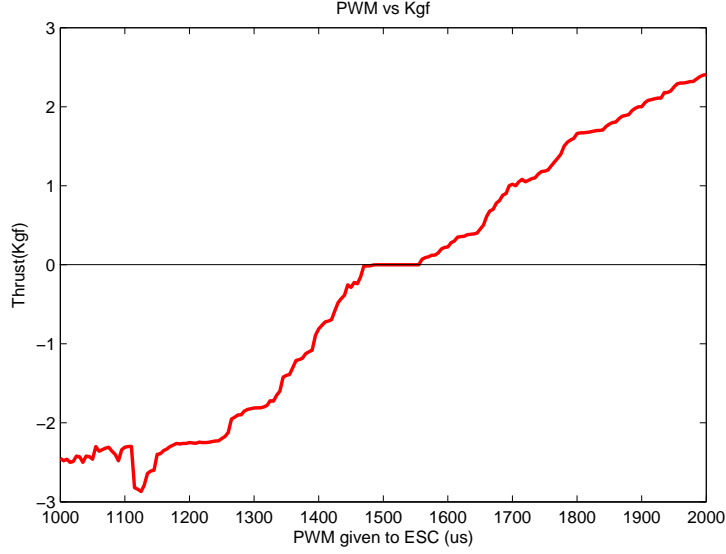


Figure 3.2: The relationship between PWM value and force (Kgf) [15]

The last one is located vertically. The motion in the x-axis (surge motion) and the rotation around the z-axis (yaw angle) are accomplished by horizontal thrusters. The motion in the z-axis (heave motion) and the rotation around the y-axis (pitch angle) are managed by using the vertical thruster. Since the vertical thruster is located almost on the center of gravity, r_3 the pitch angle is usually very small.

The resultant thrust force and moments applied on the vehicle are expressed as follow.

$$\tau = \begin{bmatrix} \sum X \\ \sum Y \\ \sum Z \\ \sum K \\ \sum M \\ \sum N \end{bmatrix} = \begin{bmatrix} T_1 + T_2 \\ 0 \\ T_3 \\ 0 \\ T_3 r_3 \\ T_1 r_1 + T_2 r_2 \end{bmatrix} \quad (3.3)$$

where

T_1 : Produced force from the right thruster,

T_2 : Produced force from the left thruster,

T_3 : Produced force from the vertical thruster,

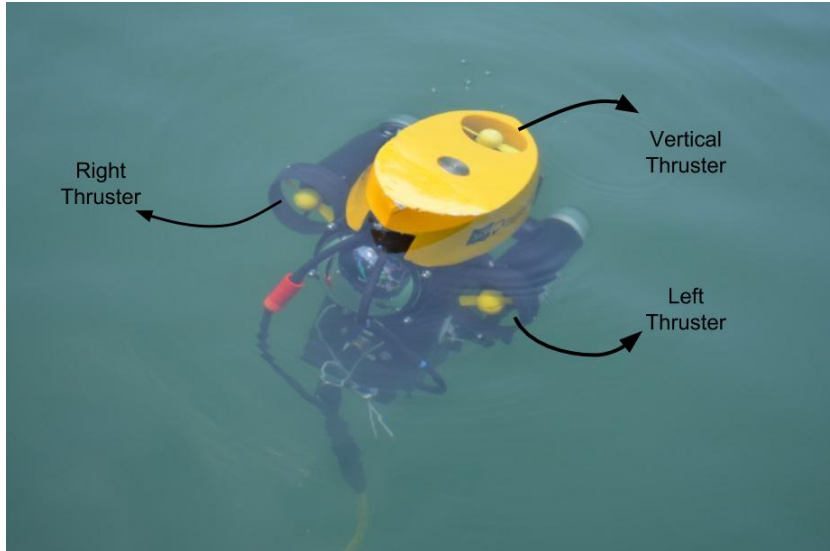


Figure 3.3: SAGA's thrusters locations

r_1 : Distance between the right thruster and the center of gravity,

r_2 : Distance between the left thruster and the center of gravity,

r_3 : Distance between the vertical thruster and the center of gravity.

The nonlinear model of SAGA is implemented in MATLAB/Simulink environment. The system response is analyzed with some tests. Each thruster produces a maximum $10N$ force.

Test 1 : $T_1 = 10, T_2 = 10, T_3 = 0$

The right and left thrusters are activated by applying equal maximum force, $10 N$ in the same direction in test 1. The system response is shown in figures 3.4 and 3.5. As seen from these figures, the vehicle moves only in the x direction with a maximum surge speed, $1.5 m/s$. The system is considered stable since the translational and rotational velocities are equal to zero.

Test 2 : $T_1 = 10, T_2 = -10, T_3 = 0$

The right and left thrusters are activated by applying equal maximum force, $10 N$ in the opposite direction in test 2. As seen in figures 3.6 and 3.7, the vehicle rotates around the z direction with rotational velocity of yaw. The system is considered

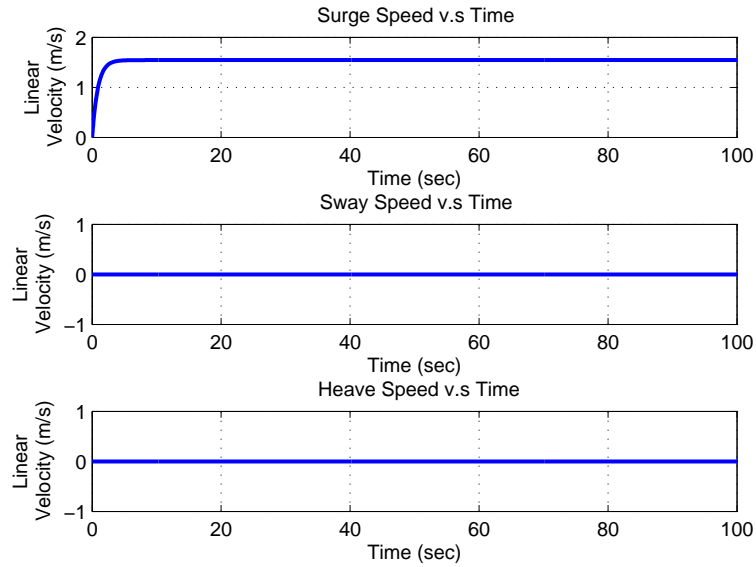


Figure 3.4: Translational velocities in the body-fixed frame for test 1

stable since rotational velocity of yaw converges to a constant value and the remaining translational and rotational velocities are equal to zero.

Test 3 : $T_1 = 0, T_2 = 0, T_3 = 10$

The vertical thruster is activated by applying max force 10 N in test 3. The vehicle moves in the z direction with heave speed as seen in figures 3.8 and 3.9. Since the vertical thruster is positioned almost on the CG of the vehicle, the rotational velocity of pitch converges to zero within 5 seconds. The system is stable when the vertical thruster works.

Test 4 : $T_1 = 0, T_2 = 10, T_3 = 0$

The right thruster is activated by applying max force 10 N in test 4. As seen in figures 3.10 3.11 the vehicle moves in x and y direction with the surge speed and the yaw rate. Test 4 shows that both of the forward thrust and yaw moment are produced using only one thruster.

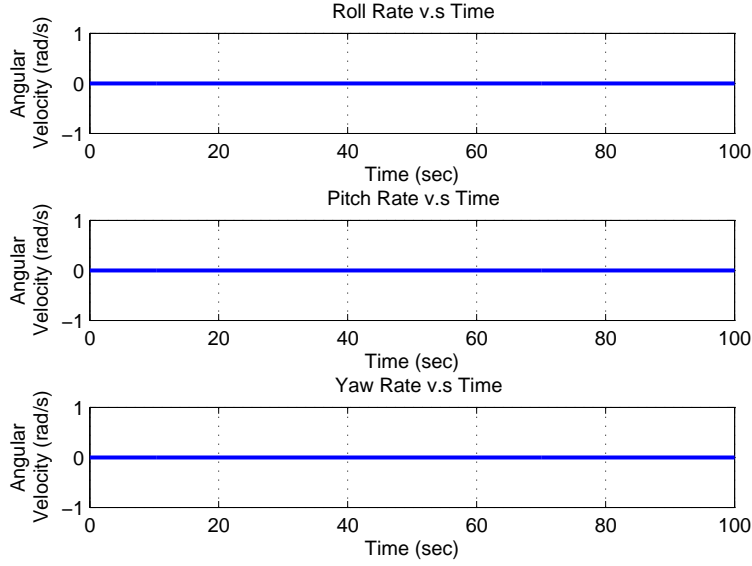


Figure 3.5: Rotational velocities in the body-fixed frame for test 1

3.3 Controller Design

Many dynamic systems are often controlled by the proportional (P)-integral (I)-derivative (D) controller known as PID controller. The error between the desired state value and the output of the system is feedback to the PID controller. This error is minimized by adjusting the control input, $u(t)$ using optimization. Control inputs are forces produced from right, left and vertical thrusters T_1 , T_2 and T_3 for SAGA. A block diagram of the PID controller is shown in Fig. 3.12.

The control input of the system, $u(t)$ is written as:

$$u(t) = K_p e(t) + K_i \int_0^t e(\tau) d\tau + K_d \frac{de(t)}{dt} \quad (3.4)$$

where

K_p : Proportional gain, a tuning parameter,

K_i : Integral gain, a tuning parameter,

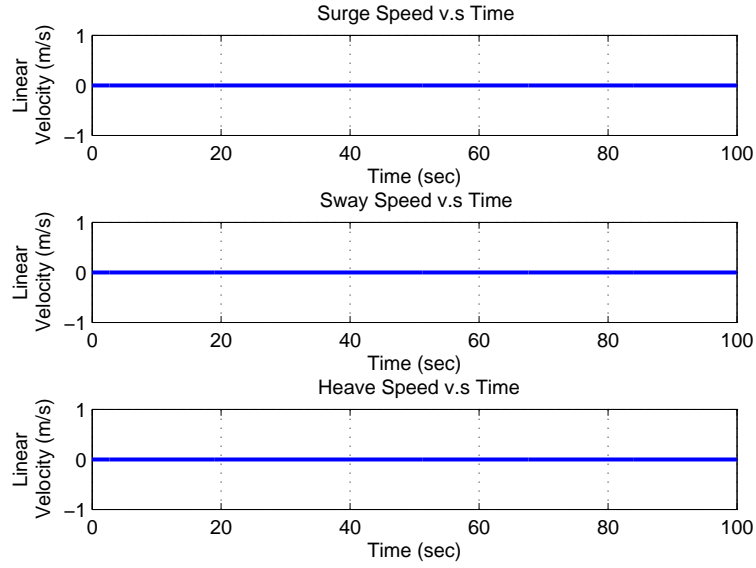


Figure 3.6: Translational velocities in body-fixed frame for test 2

K_d : Derivative gain, a tuning parameter,

e : Error, $e(t) = u(t) - y(t)$,

τ : Variable of integration, takes on values from time 0 to the present t .

A PID controller contains three parameter, K_p , K_d , K_i . A proportional controller, K_p reduces the rise time and the steady-state error. An integral control K_i provides elimination of the steady-state error, but it may increase the overshoot and settling time. A derivative control, K_d improves the stability of the system and it reduces the overshoot [34].

In this thesis, autopilot is designed by using PID controller. Optimal PID gains are obtained using auto-tuning options of MATLAB PID block.

3.3.1 Speed Controller

Since SAGA has two of the translational velocity components, u and w , and one of the rotational velocity components, r , a PID controller is designed in order to control these translational and rotational velocities independently. The output of the speed

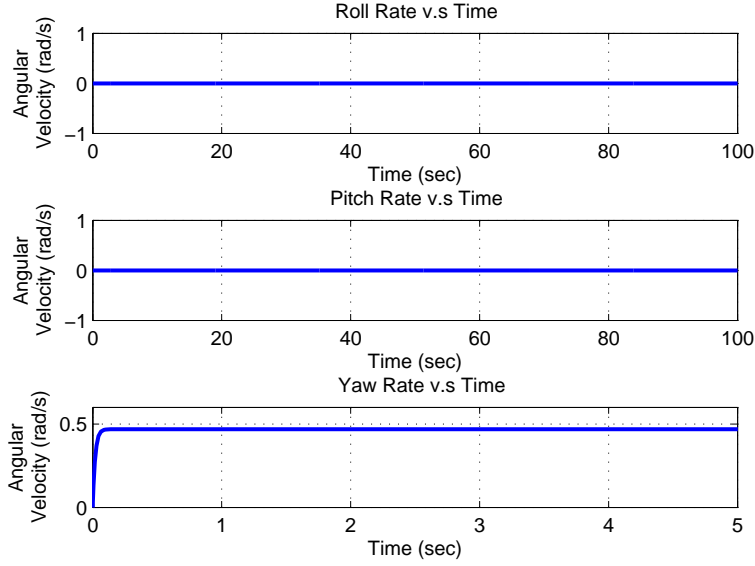


Figure 3.7: Rotational velocities in body-fixed frame for test 2

controller is the desired force. It is assumed that thruster rpm is proportional to the desired force. This desired force is divided between the right, left and vertical thrusters logically. The vertical force is allocated only to the vertical thruster. If only forward force is available, this force is distributed equally to the right and left thrusters in the same direction. If only forward moment is available, this force is distributed equally to the right and left thrusters in the opposite direction. If both forward force and forward moment are available, this force is distributed not equally to the right and left thrusters in the same direction. In this situation, since the right and left thrusters work at different rpm's, this force is divided according to importance of the job denoted by W as [13]

$$\begin{aligned}
 T_{1,rpm} &= k \\
 T_{2,rpm} &= (1 - W)k
 \end{aligned}
 \tag{3.5}$$

where

$$0 < W < 1
 \tag{3.6}$$

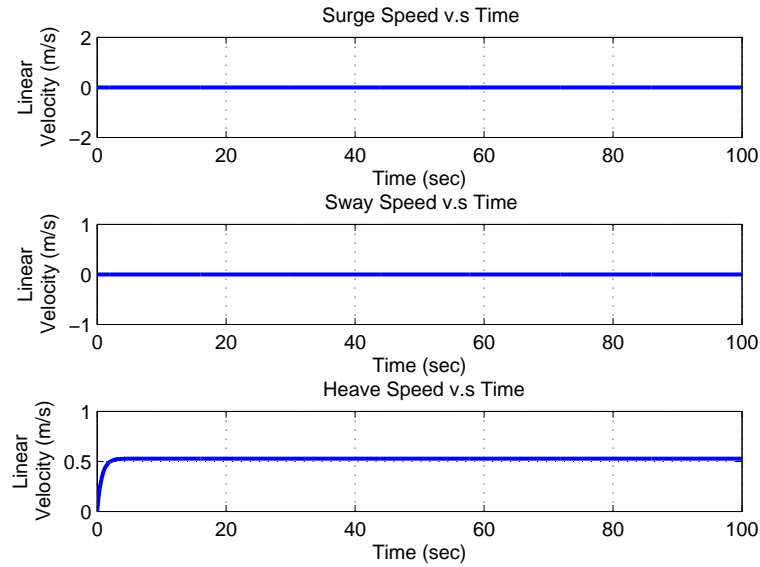


Figure 3.8: Translational velocities in body-fixed frame for test 3

Surge Speed Controller

Figure 3.13 shows the block diagram of the surge speed controller. As seen in Fig. 3.13 error is defined as the difference between the reference and actual surge speed. Optimal PID gains for the surge speed controller are obtained by minimizing the error between desired and actual surge speed values. PID controller related to optimal gains generates the reference forward force for system input. The response of the surge speed controller, right and left thrusters are shown in Figures 3.14, 3.15, respectively. As seen in these figures desired surge speed is set to 1 m/s and the controller reaches the desired value in 3.5 seconds.

Heave Speed Controller

Figure 3.16 shows the block diagram of the heave speed controller. As seen in Fig. 3.16 error is defined as the difference between the reference and actual heave speeds. Optimal PID gains for the heave speed controller are obtained by minimizing the error between desired and actual heave speed values. PID controller related to optimal gains generates the reference vertical force for system input. Heave speed controller and vertical thruster responses are shown in figures 3.17 and 3.18. As seen in these figures, desired heave speed is set to 0.3 m/s and the controller reaches the desired

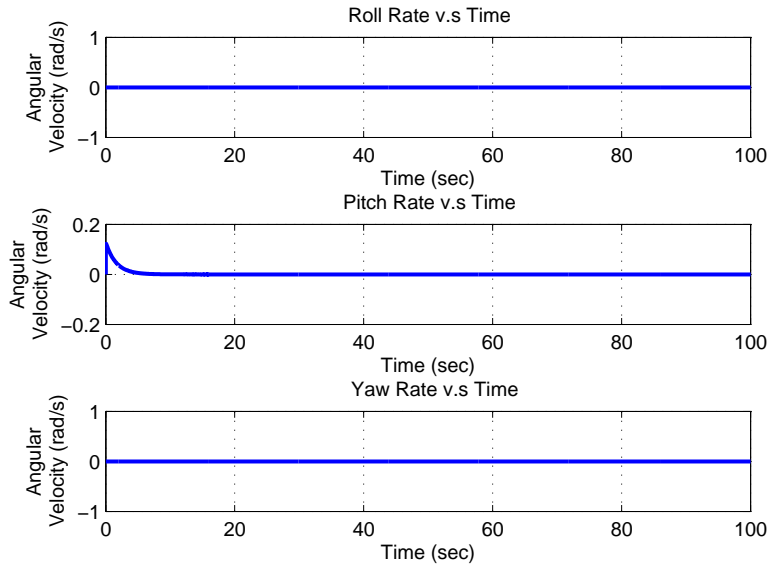


Figure 3.9: Rotational velocities in body-fixed frame for test 3

value in 3 seconds.

Yaw Rate Controller

Figure 3.19 shows the block diagram of the yaw rate controller. As seen in Fig. 3.19 error is defined as the difference between the reference and actual yaw rates. Optimal PID gains for the rotational speed of yaw controller are obtained by minimizing the error between desired and actual yaw rate values. PID controller related to optimal gains generates produces the reference right and left thrusts for system input. Yaw rate controller response and the right and left thrusters are shown in figures 3.20, 3.21, respectively. As seen in these figures, desired yaw rate is set to 0.4 rad/s and the controller reaches the desired value in 5.5 seconds.

3.3.2 Heading Controller

Figure 3.22 shows the block diagram of the yaw angle (heading) controller. As seen in Fig. 3.22 error is defined as the difference between the reference and actual yaw angles. Optimal PID gains for the yaw angle controller are obtained by minimizing the error between desired and actual yaw angle values. PID controller related to

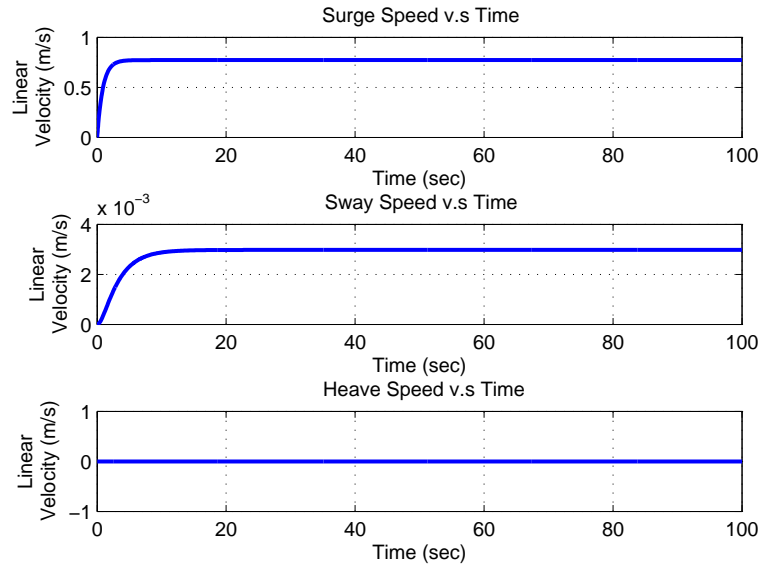


Figure 3.10: Translational velocities in body-fixed frame for test 4

optimal gains produces the reference right and left thrusts for system input. Yaw angle controller response is shown in Fig. 3.23. As seen in figure, desired yaw angle is set to 1 rad and the controller reaches the desired value in 3.5 seconds.

3.3.3 Depth Controller

Figure 3.24 shows the block diagram of the depth controller. As seen in Fig. 3.24 error is defined as the difference between the reference and actual depths. Optimal PID gains for the depth controller are obtained by minimizing the error between desired and actual depth values. PID controller related to optimal gains produces the reference vertical thrust for system input. Depth controller response is shown in Fig. 3.25. As seen in the figure, desired depth is set to 10 m and the controller reaches the desired value in 20 seconds.

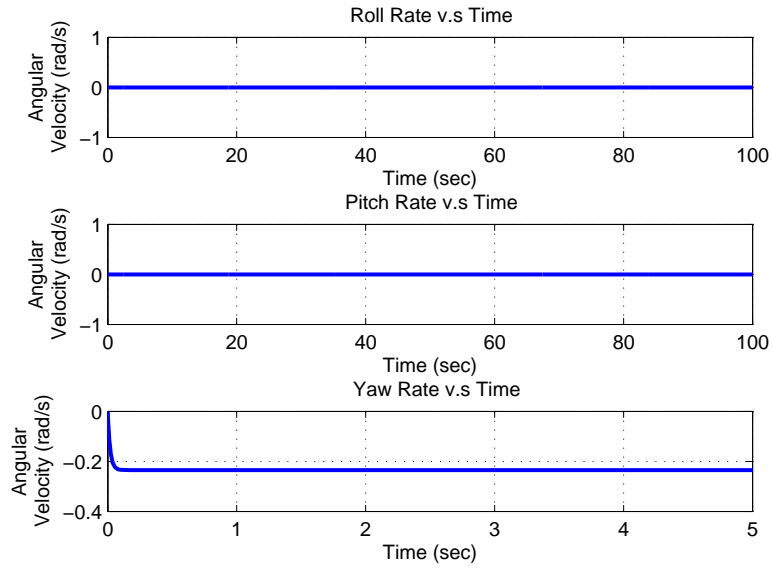


Figure 3.11: Rotational velocities in body-fixed frame for test 4

3.4 Conclusion

The nonlinear model of SAGA is implemented in Matlab/Simulink environment. System response is analyzed from the tests performed by activating different thrusters. The block diagrams of all controllers are shown and input-output signals are defined. As seen from the figures, the desired values are reached in a short time.

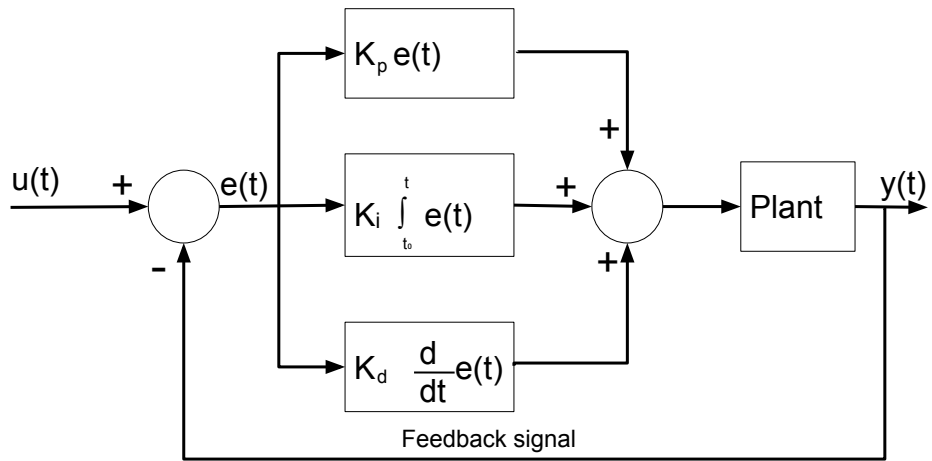


Figure 3.12: Block diagram of the PID controller

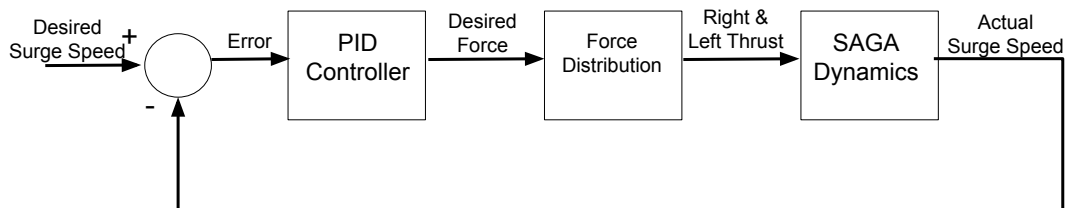


Figure 3.13: The block diagram of surge speed controller of SAGA

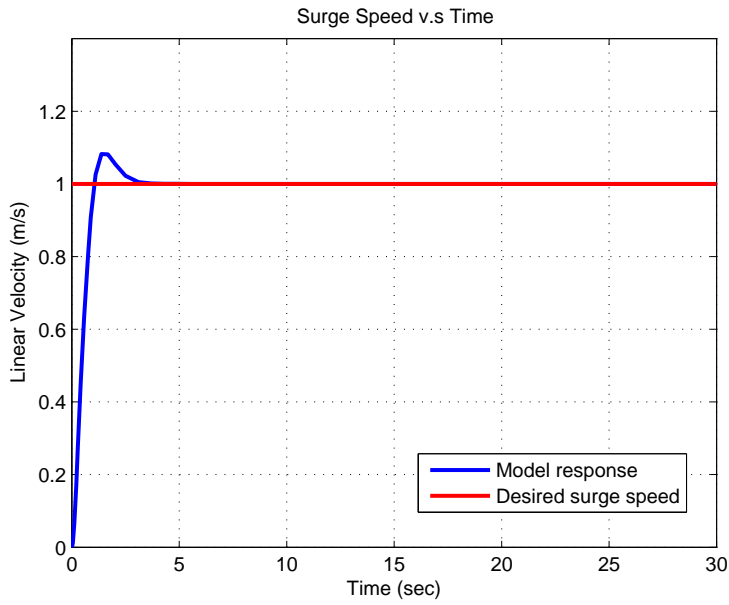


Figure 3.14: Surge speed controller response

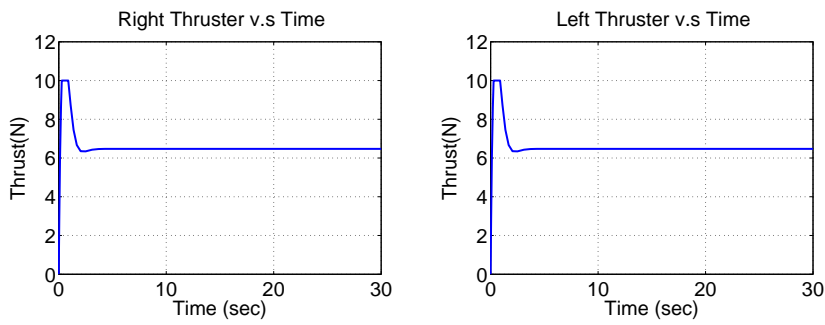


Figure 3.15: Right and left thrusters response

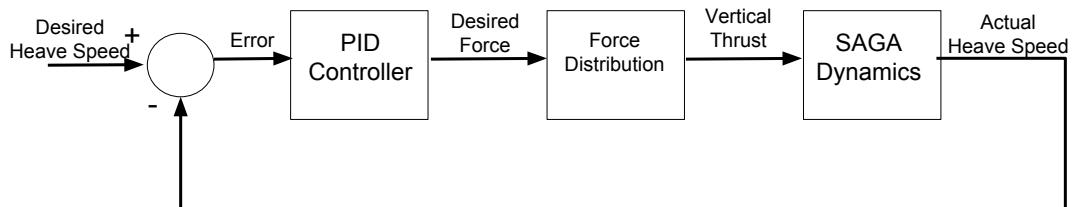


Figure 3.16: The block diagram of heave speed controller of SAGA

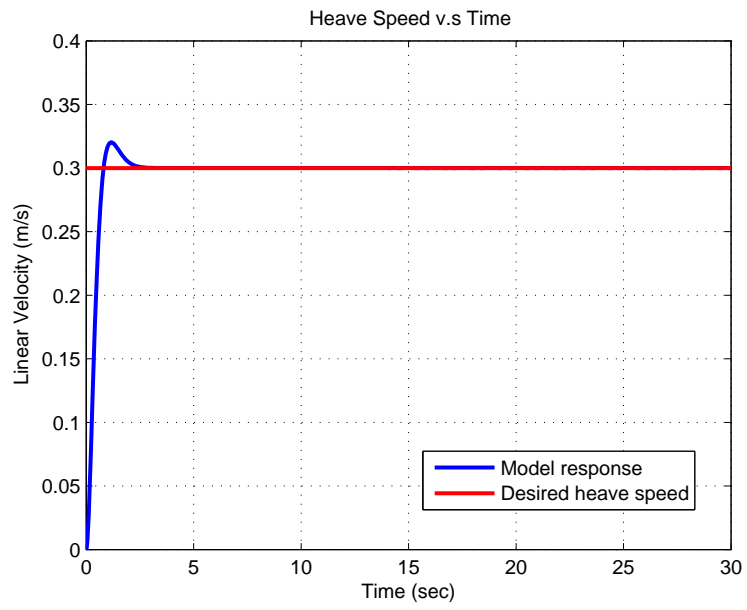


Figure 3.17: Heave speed controller response

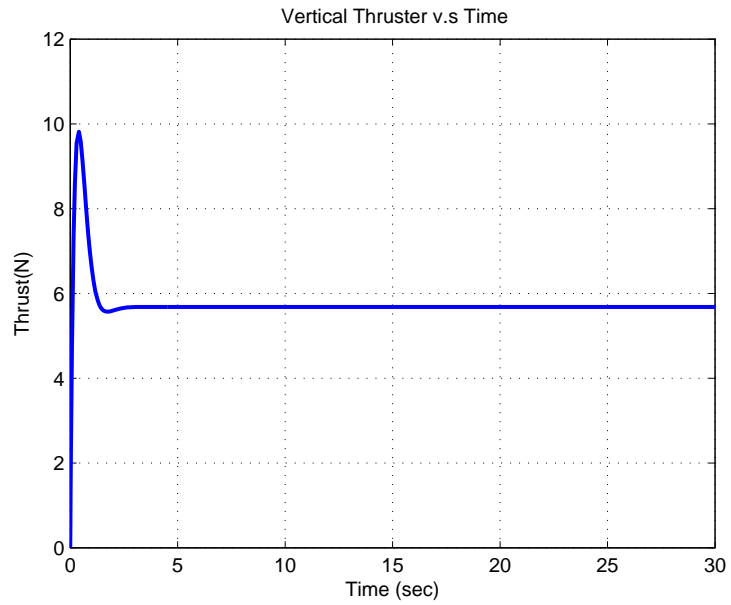


Figure 3.18: Vertical thruster response

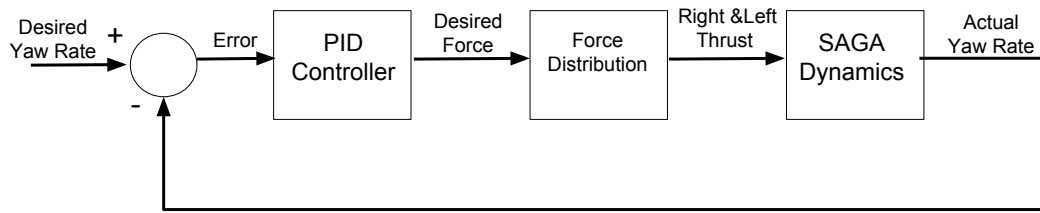


Figure 3.19: The block diagram of yaw rate controller of SAGA

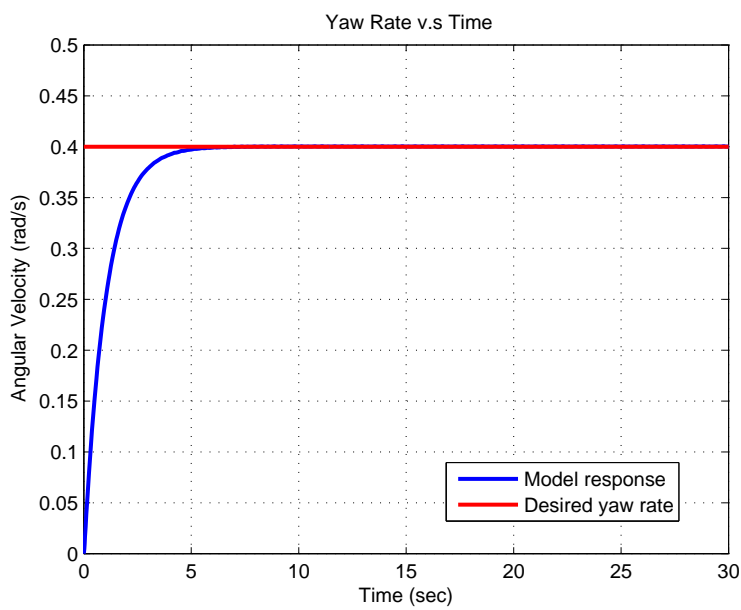


Figure 3.20: Yaw rate controller response

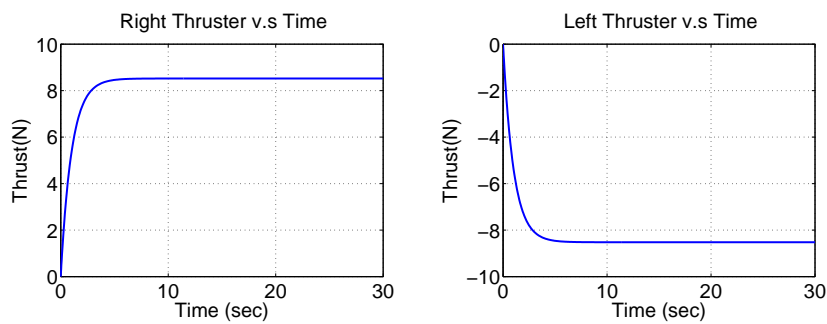


Figure 3.21: Right and left thrusters response

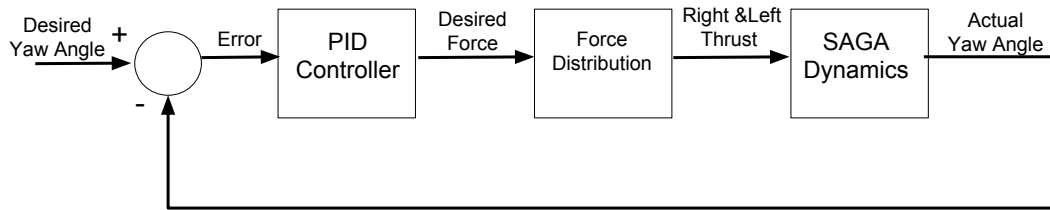


Figure 3.22: The block diagram of yaw angle controller of SAGA

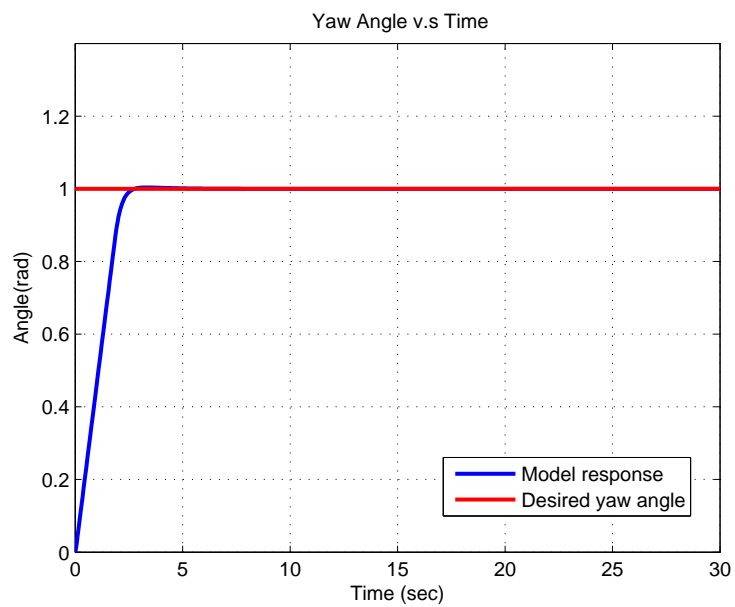


Figure 3.23: Heading angle controller response

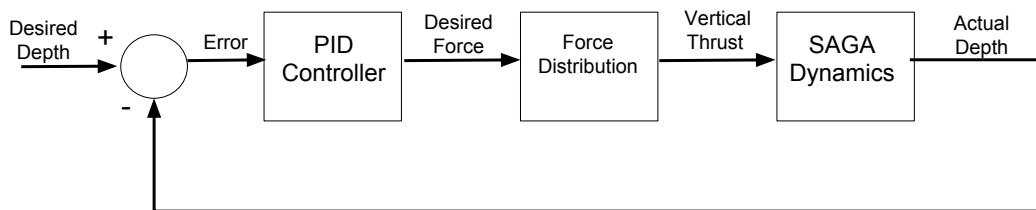


Figure 3.24: The block diagram of depth controller of SAGA

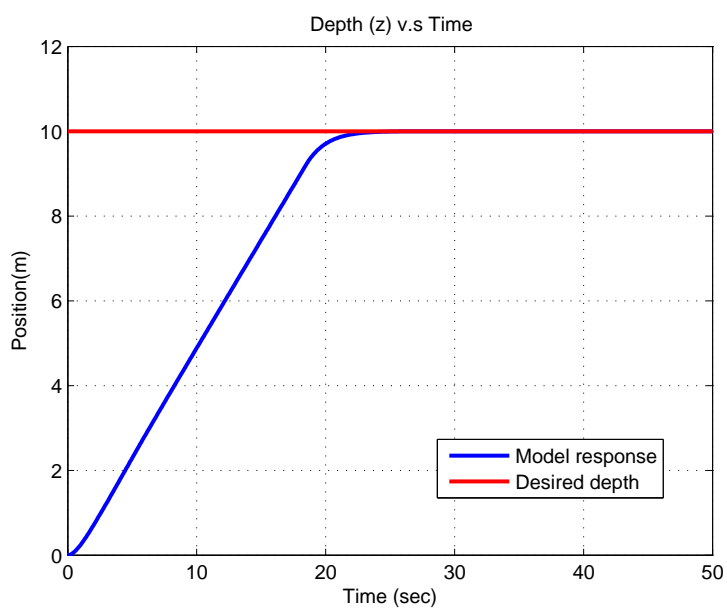


Figure 3.25: Depth controller response

CHAPTER 4

NAVIGATION

4.1 Introduction

Navigation is the determination of the position and velocity of a moving body related to a known reference. A navigation system is composed of navigation tools that determine position and velocity of the moving body. Some navigation systems measure attitude angular rate and acceleration in addition to position and velocity. The output of the navigation system is known as the navigation solution. Position fixing and dead reckoning is the basis any navigation technique. Position fixing determines the position of the moving body related to visual references, radar, celestial and electronic devices. The distance and/or relative direction between the reference objects and the moving body provides generation of position fixes. Global Positioning System (GPS) is a well-known example of a position fixing system. Dead reckoning is the process of calculating current position of the moving body by using a previously determined position and by integrating its velocity measurement. Dead reckoning technique provides a continuous position solution but it has cumulative errors. Inertial Navigation system (INS) is a well-known example for dead reckoning navigation system. For the more accuracy and continuous navigation solution, dead reckoning and position fixing system outputs are integrated [20].

4.2 Inertial Navigation System

An inertial navigation system is composed of the dead reckoning navigation system, inertial measurement unit (IMU) and a navigation processor [20]. Figure 4.2 shows the schematic illustration of an INS implementation. Navigation processor produces the navigation solution composed of position, velocity and attitude data using the integrating of accelerometer and gyroscopes outputs and gravity model after initialization [20].

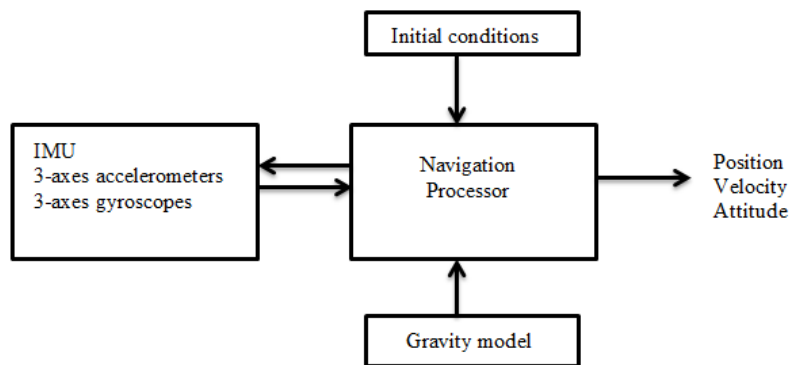


Figure 4.1: The schematic illustration of INS implementation

4.2.1 Inertial Sensors

Accelerometer and gyroscopes in three orthogonal axes are the main part of the inertial measurement unit (IMU). Accelerometer measures the specific force of the IMU body related to the inertial frame resolved along the accelerometer axes, represented by the vector f_{ib}^b . Gyroscope measures rotational speed of the IMU body related to the inertial frame resolved along the gyro axes, represented by the vector w_{ib}^b . The translational and rotational position and translational velocity information of the vehicle are obtained from these measured angular rate and force (acceleration) data by integration [20].

4.2.2 Error Characteristics

Inertial sensors error in estimated Kalman filter approach is the systematic errors. These errors sources are biases, scale factors and misalignment. The other stochastic errors cannot be easily estimated by a Kalman filter because of their random characteristics. These errors source are quantization noise, angular random walk, rate random walk, bias instability and rate ramp. These errors can be analyzed by Allan variance and some other techniques [40].

The systematic error sources are biases, scale factor, cross-coupling error, random noise and further error sources. The bias is a constant error which is not related to measured force and rotational velocity. The vectors, b_a and b_g symbolizes the bias of accelerometer and gyro, respectively. Scale factor errors of accelerometer and gyro are related to the actual specific force and actual rotational velocity. They are represented by the vector $s_a = s_{a,x}, s_{a,y}, s_{a,z}$, $s_g = s_{g,x}, s_{g,y}, s_{g,z}$ respectively. Each accelerometer is sensitive to the specific force along the axes orthogonal to its sensitive axis. The notation, $m_{a,\alpha\beta}$ and $m_{g,\alpha\beta}$ represents the cross-coupling errors of accelerometer and gyro. The scale factor and cross-coupling errors for accelerometer and gyro are defined as [20]

$$M_a = \begin{pmatrix} s_{a,x} & m_{a,xy} & m_{a,xz} \\ m_{a,yx} & s_{a,y} & m_{a,yz} \\ m_{a,zx} & m_{a,zy} & s_{a,z} \end{pmatrix}, M_g = \begin{pmatrix} s_{g,x} & m_{g,xy} & m_{g,xz} \\ m_{g,yx} & s_{g,y} & m_{g,yz} \\ m_{g,zx} & m_{g,zy} & s_{g,z} \end{pmatrix} \quad (4.1)$$

All inertial sensors have random noise. The random noise of accelerometer and gyros are represented by $w_a = w_{a,x}, w_{a,y}, w_{a,z}$, $w_g = w_{g,x}, w_{g,y}, w_{g,z}$ respectively. Spinning mass and vibratory gyros exhibit sensitivity to a specific force known as the g-dependent bias due to mass unbalance. The g-dependent bias for a gyro is represented by G_g [20].

The output information of the accelerometer and gyroscope are modeled by the following equations [20]

$$\tilde{f}_{ib}^b = b_a + (I_3 + M_a) f_{ib}^b + w_a \quad (4.2)$$

$$\tilde{w}_{ib}^b = b_g + (I_3 + M_g) w_{ib}^b + G_g f_{ib}^b + w_g \quad (4.3)$$

where the \tilde{f}_{ib}^b is the measured force from accelerometer output and the f_{ib}^b is the actual value of the force. And, \tilde{w}_{ib}^b is the measured rotational velocity from gyro output and the w_{ib}^b is the actual value of the rotational velocity.

The total acceleration error is defined as

$$\delta f_{ib}^b = \tilde{f}_{ib}^b - f_{ib}^b \quad (4.4)$$

The total gyro error is defined as

$$\delta w_{ib}^b = \tilde{w}_{ib}^b - w_{ib}^b \quad (4.5)$$

4.2.3 Inertial Navigation Processor

Inertial navigation processor produces the navigation solution, position, velocity and attitude data by integrating the measured data from accelerometer and gyro. First the kinematic quantities such as attitude, angular rate, position, velocity and acceleration are expressed before deriving the navigation update equations. In addition, used gravity and earth model will be expressed.

4.2.3.1 Kinematics

4.2.3.1.1 Coordinate Transformation Matrix

The coordinate transformation matrix is a 3×3 matrix. It is represented by C_{α}^{β} . It is used to transform a vector from one set of resolving axes to another, the lower index represents the “from” coordinate frame and the upper index the “to” frame [20]. Hence,

$$x_{\delta\gamma}^{\beta} = C_{\alpha}^{\beta} x_{\delta\gamma}^{\alpha} \quad (4.6)$$

In this notation shows the transformation from α coordinate frame to β coordinate frame. The coordinate transformation matrix properties such as transpose, multiplication and reversing, are given as

$$\begin{aligned} C_{\beta}^{\alpha} &= (C_{\alpha}^{\beta})^T \\ C_{\alpha}^{\gamma} &= C_{\beta}^{\gamma} C_{\alpha}^{\beta} \\ C_{\alpha}^{\gamma} &\neq C_{\alpha}^{\beta} C_{\beta}^{\gamma} \\ C_{\alpha}^{\beta} C_{\beta}^{\alpha} &= I_3 \end{aligned} \quad (4.7)$$

The coordinate transformation matrix from β to α is obtained multiply the rotation transformation matrix around x, y and z direction. So;

$$C_{\beta}^{\alpha} = C_x C_y C_z \quad (4.8)$$

$$C_{\beta}^{\alpha} = \begin{bmatrix} 1 & 0 & 0 \\ 0 & \cos\phi & \sin\phi \\ 0 & -\sin\phi & \cos\phi \end{bmatrix} \begin{bmatrix} \cos\theta & 0 & -\sin\theta \\ 0 & 1 & 0 \\ \sin\theta & 0 & \cos\theta \end{bmatrix} \begin{bmatrix} \cos\varphi & \sin\varphi & 0 \\ -\sin\varphi & \cos\varphi & 0 \\ 0 & 0 & 1 \end{bmatrix} \quad (4.9)$$

$$C_{\beta}^{\alpha} = \begin{bmatrix} c\theta_{\beta\alpha} c\varphi_{\beta\alpha} & c\theta_{\beta\alpha} s\varphi_{\beta\alpha} & -s\theta_{\beta\alpha} \\ -c\phi_{\beta\alpha} s\varphi_{\beta\alpha} + s\phi_{\beta\alpha} s\theta_{\beta\alpha} c\varphi_{\beta\alpha} & c\phi_{\beta\alpha} c\varphi_{\beta\alpha} + s\phi_{\beta\alpha} s\theta_{\beta\alpha} s\varphi_{\beta\alpha} & s\phi_{\beta\alpha} c\theta_{\beta\alpha} \\ s\phi_{\beta\alpha} s\varphi_{\beta\alpha} + c\phi_{\beta\alpha} s\theta_{\beta\alpha} c\varphi_{\beta\alpha} & -s\phi_{\beta\alpha} c\varphi_{\beta\alpha} + c\phi_{\beta\alpha} s\theta_{\beta\alpha} s\varphi_{\beta\alpha} & c\phi_{\beta\alpha} c\theta_{\beta\alpha} \end{bmatrix} \quad (4.10)$$

If the Euler angles and the coordinate transformation matrix represent a small angular perturbation, the Equation 4.11 becomes [20]

$$C_{\beta}^{\alpha} = \begin{bmatrix} 1 & \psi_{\beta\alpha} & -\theta_{\beta\alpha} \\ -\psi_{\beta\alpha} & 1 & \phi_{\beta\alpha} \\ \theta_{\beta\alpha} & -\phi_{\beta\alpha} & 1 \end{bmatrix} = I_3 - [\psi_{\beta\alpha} \wedge] \quad (4.11)$$

4.2.3.1.2 Angular Rate

The angular rate vector $w_{\beta\alpha}^\gamma$ is the rate of rotation of the α frame axes with respect to the β frame axes, resolved about the γ frame axes. The angular rate vector is represented by the skew-symmetric form in navigation equation [20].

$$\Omega_{\beta\alpha}^\gamma = [w_{\beta\alpha}^\gamma \wedge] = \begin{bmatrix} 0 & -w_{\beta\alpha 3}^\gamma & w_{\beta\alpha 2}^\gamma \\ w_{\beta\alpha 3}^\gamma & 0 & w_{\beta\alpha 1}^\gamma \\ w_{\beta\alpha 2}^\gamma & w_{\beta\alpha 1}^\gamma & 0 \end{bmatrix} \quad (4.12)$$

Using the small angle approximation applied in the limit $\delta t \rightarrow 0$, the time derivative of the coordinate transformation matrix is obtained as

$$\dot{C}_\beta^\alpha = -C_\beta^\alpha \Omega_{\beta\alpha}^\beta = -\Omega_{\beta\alpha}^\alpha C_\beta^\alpha = C_\beta^\alpha \Omega_{\alpha\beta}^\beta = \Omega_{\alpha\beta}^\alpha C_\beta^\alpha \quad (4.13)$$

4.2.3.1.3 Position

A Cartesian position of the frame α with respect to the origin of frame β , resolved about the axes of frame γ is $r_{\beta\alpha}^\gamma = (x_{\beta\alpha}^\gamma, y_{\beta\alpha}^\gamma, z_{\beta\alpha}^\gamma)$, where x, y and z are the components of position in the x, y and z axes of the γ frame [20].

The object and reference frame of a Cartesian position can be transposed with the same resolving frame:

$$r_{\beta\alpha}^\gamma = -r_{\alpha\beta}^\gamma \quad (4.14)$$

If two Cartesian positions are resolved in the same frame, they are simply added:

$$r_{\beta\alpha}^\gamma = r_{\beta\delta}^\gamma + r_{\delta\alpha}^\gamma \quad (4.15)$$

Also, the Cartesian position can be resolved in other frames by multiplying the coordinate transformation matrix as:

$$r_{\beta\alpha}^\delta = C_\gamma^\delta r_{\beta\alpha}^\gamma \quad (4.16)$$

Considering specific frames, the origins of the ECI and ECEF frames coincide as local and body frames [20]. Thus,

$$r_{ie}^{\gamma} = r_{nb}^{\gamma} = 0 \quad (4.17)$$

and

$$r_{ib}^{\gamma} = r_{eb}^{\gamma} = r_{in}^{\gamma} = r_{en}^{\gamma} = 0 \quad (4.18)$$

4.2.3.1.4 Velocity

Velocity is defined as the rate of change of the position of the origin of an object frame with respect to the origin and axes of a reference frame. So, the velocity of frame α with respect to frame β , resolved about the axes of frame γ , is defined as [20]:

$$v_{\beta\alpha}^{\gamma} = C_{\beta}^{\gamma} \dot{r}_{\beta\alpha}^{\beta} \quad (4.19)$$

The time derivative of the position is,

$$\dot{r}_{\beta\alpha}^{\gamma} = \dot{C}_{\beta}^{\gamma} r_{\beta\alpha}^{\beta} + v_{\beta\alpha}^{\gamma} \quad (4.20)$$

As seen in equation 4.19, velocity, $v_{\beta\alpha}^{\gamma}$ is not equal to time derivative of position, $\dot{r}_{\beta\alpha}^{\gamma}$. Velocity may be resolved in other frames by multiplying the related coordinate transformation matrix as:

$$v_{\beta\alpha}^{\delta} = C_{\gamma}^{\delta} v_{\beta\alpha}^{\gamma} \quad (4.21)$$

If the reference frames rotate with respect to each other, velocities are not added [20]:

$$v_{\beta\alpha}^{\gamma} \neq v_{\beta\delta}^{\gamma} + v_{\delta\alpha}^{\gamma} \quad (4.22)$$

4.2.3.1.5 Acceleration

Acceleration is defined as the second time derivative of the position of the origin of one frame with respect to the origin and axes of another frame. The acceleration of frame α with respect to frame β , resolved about the axes of frame γ is expressed as [20]:

$$a_{\beta\alpha}^{\gamma} = C_{\beta}^{\gamma} \ddot{r}_{\beta\alpha}^{\beta} \quad (4.23)$$

The acceleration is not equal to the time derivative of $v_{\beta\alpha}^{\gamma}$ or the second time derivative of $r_{\beta\alpha}^{\gamma}$:

$$\dot{v}_{\beta\alpha}^{\gamma} = \dot{C}_{\beta}^{\gamma} \dot{r}_{\beta\alpha}^{\beta} + a_{\beta\alpha}^{\gamma} \quad (4.24)$$

$$\ddot{r}_{\beta\alpha}^{\gamma} = \ddot{C}_{\beta}^{\gamma} r_{\beta\alpha}^{\beta} + \dot{C}_{\beta}^{\gamma} \dot{r}_{\beta\alpha}^{\beta} + \dot{v}_{\beta\alpha}^{\gamma} \quad (4.25)$$

$$\ddot{r}_{\beta\alpha}^{\gamma} = \ddot{C}_{\beta}^{\gamma} r_{\beta\alpha}^{\beta} + 2\dot{C}_{\beta}^{\gamma} \dot{r}_{\beta\alpha}^{\beta} + a_{\beta\alpha}^{\gamma} \quad (4.26)$$

The first term on the right hand side of equation 4.26 is the centrifugal acceleration and the second term is the Coriolis acceleration. From 4.13 and 4.16,

$$\ddot{C}_{\beta}^{\gamma} r_{\beta\alpha}^{\beta} = (\Omega_{\beta\gamma}^{\gamma} \Omega_{\beta\gamma}^{\gamma} - \dot{\Omega}_{\beta\gamma}^{\gamma}) r_{\beta\alpha}^{\gamma} \quad (4.27)$$

and, from 4.20, 4.13 and 4.16

$$\dot{C}_{\beta}^{\gamma} \dot{r}_{\beta\alpha}^{\beta} = -\Omega_{\beta\gamma}^{\gamma} \Omega_{\beta\gamma}^{\gamma} r_{\beta\alpha}^{\gamma} - \Omega_{\beta\gamma}^{\gamma} \dot{r}_{\beta\alpha}^{\gamma} \quad (4.28)$$

The equations 4.27 and 4.28 are substituted into 4.26,

$$\ddot{r}_{\beta\alpha}^{\gamma} = -(\dot{\Omega}_{\beta\gamma}^{\gamma} + \Omega_{\beta\gamma}^{\gamma} \Omega_{\beta\gamma}^{\gamma}) r_{\beta\alpha}^{\gamma} - 2\Omega_{\beta\gamma}^{\gamma} \dot{r}_{\beta\alpha}^{\gamma} + a_{\beta\alpha}^{\gamma} \quad (4.29)$$

The acceleration is transformed to other set of axes by applying the related coordinate transformation matrix:

$$a_{\beta\alpha}^{\delta} = C_{\gamma}^{\delta} a_{\beta\alpha}^{\gamma} \quad (4.30)$$

if the reference frames rotate with respect to each other accelerations are not added [20]:

$$a_{\beta\alpha}^{\gamma} \neq a_{\beta\delta}^{\gamma} + a_{\delta\alpha}^{\gamma} \quad (4.31)$$

4.2.3.2 Earth Model

For the navigation solution, Earth model and Earth's surface are needed. The coordinates of position with respect to reference surface, longitude, latitude and height are required. Measurements coming from the inertial navigation system with respect to Earth referenced coordinate frame and Earth's rotation should be taken into account.

4.2.3.2.1 The Ellipsoid Model of the Earth's Surface

The surface of the Earth can be approximated as an ellipsoid fitted in the main sea level. The ellipsoid is commonly defined in terms of the equatorial radius and the eccentricity of the ellipsoid, e [20]. The eccentricity is defined by

$$e = \sqrt{1 - \frac{R_p^2}{R_0^2}} \quad (4.32)$$

where R_0 is the length of semi-major axis and R_p is the length of semi-minor axis. According to World Geodetic System 1984 (WGS84):

$$R_0 = 6378137.0 \text{ m}$$

$$R_p = 6356752.3142 \text{ m}$$

$$e = 0.0818191908425$$

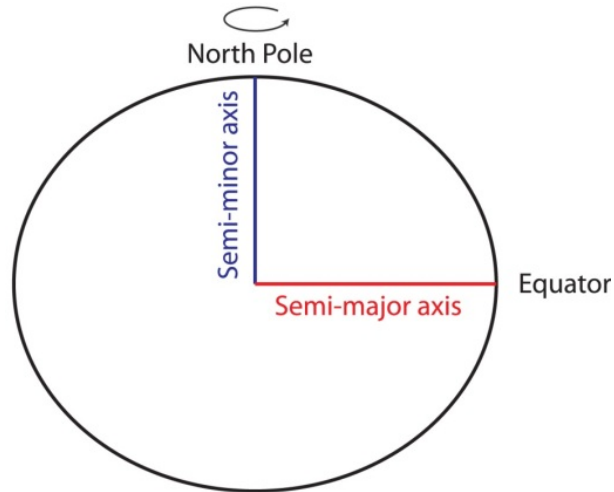


Figure 4.2: Cross-section of the ellipsoid representing the Earth's surface [20]

4.2.3.2.2 Curvilinear position

Position with respect to the Earth's surface is described using three mutually orthogonal coordinates, aligned with the axes of the local navigation frame, height (h), the latitude (L), and the longitude (λ) known as curvilinear position. Height or altitude is the distance from the body to the surface in the normal direction. Latitude is the north-south axis coordinate of the point on the surface where that normal intersects. Longitude is the coordinate of that point in the east-west axis as seen in Fig. 4.3.

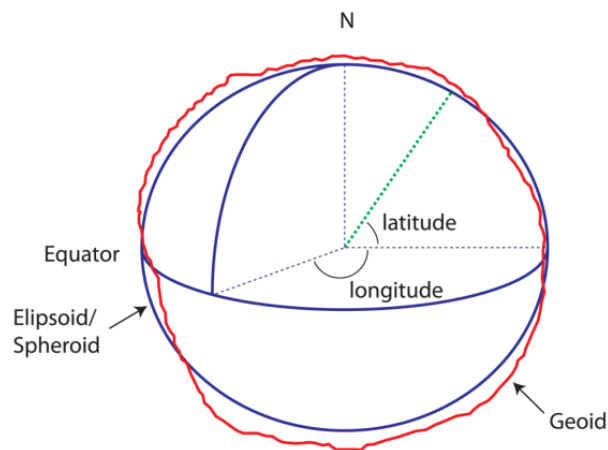


Figure 4.3: Geocentric and geodetic latitude [20]

The transverse radius of curvature is needed to obtain curvilinear position from Cartesian ECEF position. It is given by

$$\frac{R}{E}(L) = \frac{R_0}{\sqrt{1 - e^2 \sin^2 L}} \quad (4.33)$$

Then, the curvilinear position is

$$\sin L_b = \frac{z_{eb}^e}{(1 - e^2)R_E(L_b) + h_b} \quad (4.34)$$

$$\tan \lambda_b = \frac{y_{eb}^e}{x_{eb}^e} \quad (4.35)$$

$$h_b = \frac{\sqrt{(x_{eb}^e)^2 + (y_{eb}^e)^2}}{\cos L_b} - R_E(L_b) \quad (4.36)$$

4.2.3.2.3 Earth Rotation

Earth rotates, with respect to space, clockwise about the common z-axis of the ECI and ECEF frames. The Earth-rotation vector resolved in these axes is given by

$$w_{ie}^i = w_{ie}^e = \begin{pmatrix} 0 \\ 0 \\ w_{ie} \end{pmatrix} \quad (4.37)$$

According to WGS 84 the value of the Earth's angular velocity is

$$w_{ie} = 7.292115 \times 10^{-5} \text{ rad s}^{-1}$$

4.2.3.2.4 Specific Force, Gravitation, and Gravity

Specific force is the non-gravitational force, sum of all forces acting on a body with respect to an inertial frame. It is measured by accelerometers in the body axes represented by f_{ib} . Gravitation is the fundamental mass attraction force and it does not incorporate any centripetal components. Acceleration due to gravitational force is

represented by γ_{ib}^γ . The specific force is related to acceleration, a , and the acceleration due to the gravitational force, γ [20].

$$f_{ib}^\gamma = a_{ib}^\gamma - \gamma_{ib}^\gamma \quad (4.38)$$

If the object is stationary with respect to rotating frame, the velocity, acceleration and position properties are

$$v_{eb}^e = 0 \quad a_{eb}^e = 0 \quad (4.39)$$

$$\dot{r}_{ib}^e = \dot{r}_{eb}^e = 0 \quad \ddot{r}_{ib}^e = \ddot{r}_{eb}^e = 0 \quad (4.40)$$

Then, the specific force of stationary object is the reaction to the acceleration due to gravity defined as

$$g_b^\gamma = \Upsilon_{ib}^\gamma - \Omega_{ie}^\gamma \Omega_{ie}^\gamma r_{eb}^\gamma \quad (4.41)$$

4.2.3.3 Inertial Navigation Equations

The inertial navigation equation is obtained in four steps. They are attitude update, transformation of the specific force resolving axes, velocity update and position update. In addition, the gravity model is needed for velocity update. The outputs of the IMU are force and angular rate in the body-axes. The attitude is updated by integrating measured angular rate from gyros. The velocity is updated by integrating measured force data from accelerometers. The position is updated by integrating velocity. In this thesis, the reference frame and resolving axes are chosen as ECEF frame. Thus, the navigation solution is expressed in ECEF frame. The block diagram of the inertial navigation equation is shown in Fig. 4.22. The symbols $(-)$ and $(+)$ represent the beginning and end of navigation equations processing cycle respectively at all of the following update equations.

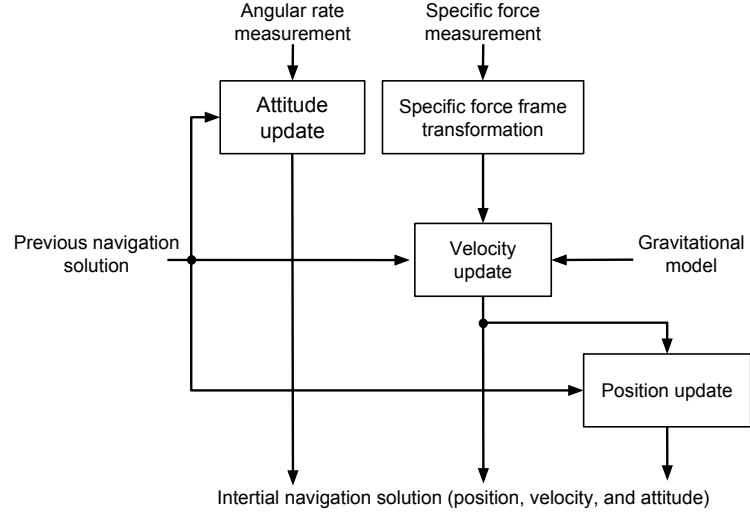


Figure 4.4: Schematic of an inertial navigation processor

4.2.3.3.1 Attitude Update

The time derivative of the earth frame coordinate transformation matrix is expressed with respect to earth rotation and angular rate coming from gyros.

$$\begin{aligned} C_b^e &= C_b^e \Omega_{eb}^b \\ \dot{C}_b^e &= C_b^e \Omega_{ib}^b - \Omega_{ie}^e C_b^e \end{aligned} \quad (4.42)$$

where Ω_{ib}^b is the skew-symmetric matrix of angular rate measured from gyros. The Earth rotation skew-symmetric matrix represented by Ω_{ie}^e is given by

$$\Omega_{ie}^e = \begin{pmatrix} 0 & -w_{ie} & 0 \\ w_{ie} & 0 & 0 \\ 0 & 0 & 0 \end{pmatrix} \quad (4.43)$$

By integrating of the equation 4.42 from t to $t + \tau_i$, where τ_i is the sampling interval of the inertial sensors, Earth-frame coordinate transformation matrix is updated as

$$C_b^e(+)\approx C_b^e(-)\left(I_3+\Omega_{ib}^b\tau_i\right)-\Omega_{ie}^e C_b^e(-)\tau_i \quad (4.44)$$

4.2.3.3.2 Specific-Force Frame Transformation

The specific force measured by accelerometers in the body-axes is transformed to ECEF using the approximate coordinate transformation matrix as

$$\begin{aligned} f_{ib}^e(t) &= C_b^e(t) f_{ib}^b(t) \\ f_{ib}^e(t) &\cong \frac{1}{2}(C_b^e(+)+C_b^e(-))f_{ib}^b \end{aligned} \quad (4.45)$$

4.2.3.3.3 Velocity Update

Since the reference and resolving frames are the same (earth frame), the time derivative of the velocity is defined as

$$\ddot{v}_{eb}^e = a_{eb}^e = \ddot{r}_{eb}^e \quad (4.46)$$

Applying 4.29, assuming the Earth's rotation rate is constant, we can rewrite equation 4.46 as:

$$\dot{V}_{eb}^e = -(\Omega_{ie}^e \Omega_{ie}^e r_{ib}^e) - 2\Omega_{ie}^e \dot{r}_{ib}^e + a_{ib}^e \quad (4.47)$$

Applying equations 4.18 and 4.19

$$\dot{v}_{eb}^e = -(\Omega_{ie}^e \Omega_{ie}^e r_{eb}^e) - 2\Omega_{ie}^e v_{eb}^e + a_{ib}^e \quad (4.48)$$

Substituting Equation 4.38 and Equation 4.41, in Equation 4.48, the final expression for the velocity update differential equation is expressed as:

$$v_{eb}^e = f_{ib}^e + g_b^e(r_{eb}^e) - 2\Omega_{ie}^e v_{eb}^e \quad (4.49)$$

Integrating the equation 4.49 gives

$$v_{eb}^e (+) = v_{eb}^e (-) + v_{ib}^e + g_b^e (r_{eb}^e (-)) - 2\Omega_{ie}^e v_{eb}^e (-) \tau_i \quad (4.50)$$

4.2.3.3.4 Position Update

Since the reference and resolving frames are the same at the ECEF frame, the time derivative of the position is expressed as

$$\dot{r}_{\beta e}^e = v_{eb}^e \quad (4.51)$$

Assuming that the velocity varies linearly over the integration interval, integrating equation 4.51 gives

$$r_{eb}^e (+) = r_{eb}^e (-) + (v_{eb}^e (-) + v_{eb}^e (+)) \frac{\tau_i}{2} \quad (4.52)$$

4.2.3.4 INS Error Propagation

The inertial navigation system integrates the output of the accelerometers and gyros to produce the navigation solution. Because of this, the error of the INS grows with time. INS position and velocity errors are defined as

$$\delta r_{\beta\alpha}^\gamma = r_{\beta\alpha}^\gamma - \tilde{r}_{\beta\alpha}^\gamma \quad (4.53)$$

$$\delta v_{\beta\alpha}^\gamma = v_{\beta\alpha}^\gamma - \tilde{v}_{\beta\alpha}^\gamma \quad (4.54)$$

The attitude error can be calculated using the coordinate transformation matrix:

$$\delta C_\beta^\alpha = \tilde{C}_\beta^\alpha C_\alpha^\beta \quad (4.55)$$

where the small angle approximation applies. The attitude error can be expressed in terms of the coordinate transform as:

$$[\partial\psi_{\beta\alpha}^\alpha \wedge] \approx I_3 - \delta C_\beta^\alpha \quad (4.56)$$

$$[\partial\psi_{\beta\alpha}^\beta \wedge] \approx \delta C_\alpha^\beta - I_3 \quad (4.57)$$

4.3 Global Navigation Satellite System (GNSS)

Global navigation satellite systems provide the user with a three-dimensional positioning solution by passive ranging using radio signals transmitted by orbiting satellites. The most well-known is the Navigation by Satellite Ranging and Timing (NAVSTAR) Global Positioning System (GPS) operated by U.S while the Russian GLONASS is also operational [20].

Global navigation satellite system is composed of three segments, the space segment, the control segment and the user segment as shown in Fig. 4.5. The space segment consists of the satellites which are distributed between a number of medium Earth orbits, inclined at roughly 60° to the equator with two orbits per day. These satellites transmit radio signals composed of the ranging codes and navigation data messages. The ranging codes are used by the user equipment in order to determine the time at which the received signals were transmitted from. The data message gives the information is related to the satellite orbits and it contains timing parameters [20].

The control segment is composed of data uploading stations, monitor stations and master control stations. Ranging measurements from satellites are obtained from monitor stations. The monitor stations send these measurements to the master control stations. The master control stations adjust the satellite's orbit parameters and calibrate the satellite clocks since the location of the control segments are known and they have synchronized clocks. Master control stations transmit adjusting orbit parameters and time corrections to satellites through uploading stations [20].

The user segment consists of antenna, receiver, ranging processor and navigation pro-

processor. The antenna converts the incoming GNSS radio signals to electrical signals. These are input to the receiver, which demodulates the signals using a clock to provide a time reference. The ranging processor uses acquisition and tracking algorithms to determine the range from antenna to each of the satellites used from the receiver outputs. It also controls the receiver and decodes the navigation messages. Finally, the navigation processor compute the user position and velocity solution by the using the ranging measurements and it calibrates the receiver clock errors [20].

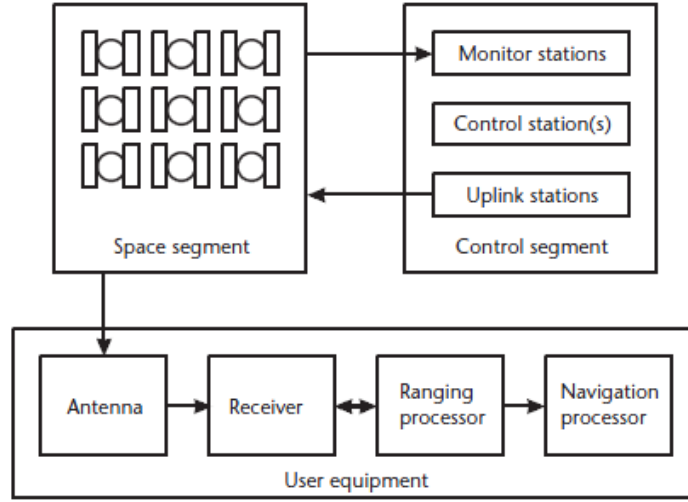


Figure 4.5: GNSS system components. [20]

Figure 4.6 shows the producing the position solution using four satellite navigation signals. Each pseudo range measurement, $\tilde{\rho}_{Cj}$, is defined related to each satellite position, $r_{is,j}^i$, user antenna position, r_{ia}^i , and range of the receiver clock error, $\Delta\rho_{rj}$. The three dimensional position and velocity of the GNSS user equipment is solved using the pseudo-ranges and pseudo-range rates [20].

GNSS solution is the estimated position and velocity with respect to the earth frame. It is defined in the vector from as

$$\hat{x}_G = \begin{pmatrix} \hat{r}_{eaG}^e \\ \hat{v}_{eaG}^e \end{pmatrix} \quad (4.58)$$

The accuracy of the GNSS position error is related to signal frequency, multipath

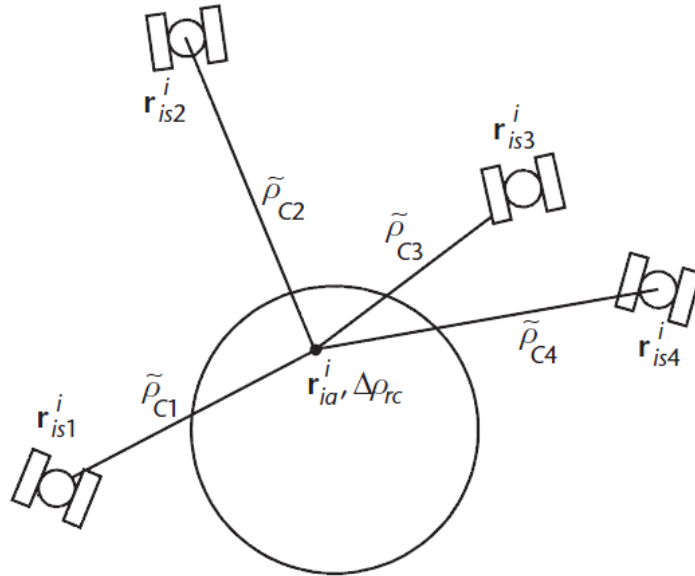


Figure 4.6: Position solution geometry using four satellite navigation signals [20]

environment and the modulation scheme.

4.4 Acoustic-based Navigation System

Acoustic based navigation system can be accomplished in more than one way. In the first method, the system is composed of hydrophones and a pinger. The second one utilizes an Ultra Short Base Line (USBL) device. In this thesis, since the first explained system is designed in the pool, it is used as the acoustic-based navigation system.

Our Acoustic-based Navigation System

Acoustic-based measurement system is composed of the pinger, hydrophones and a data card. Pinger is located on the vehicle. Hydrophones are located at known positions in the pool. Data card is outside the pool. Pinger has adjustable frequency around 20-50 kHz. It sends acoustic signals at frequencies from 20 up to 50 kHz at each second. Four hydrophones are necessary to obtain the position of the vehicle. For more accurate results, eight hydrophones can be used. Data card has many input

and output ports. The cable of each hydrophone is connected to an output port of the data card. The signals can be collected synchronously using this data card.

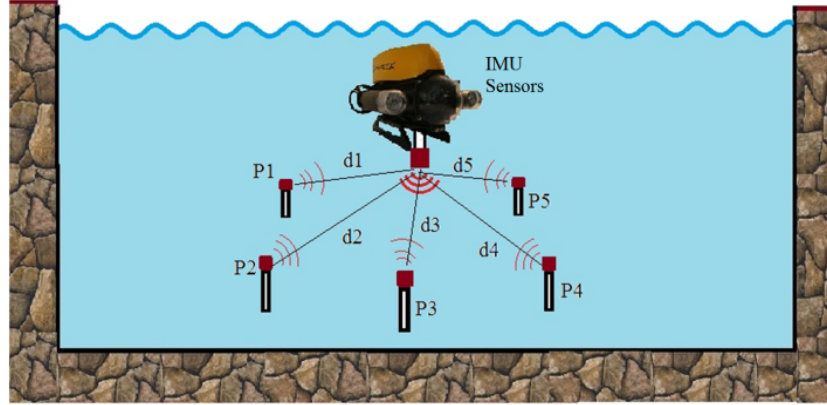


Figure 4.7: The schematic illustration of the acoustic-based navigation system

The symbolic diagram of the acoustic-based navigation system is shown in fig. 4.7. Eight hydrophones are used. Each hydrophone is located at a known position in the pool, P_i . Pinger is located in SAGA. While the vehicle moves in the pool, each hydrophone receives acoustic signal sent from the pinger. The distance between the vehicle and each hydrophone is obtained from the speed of the acoustic signal and the time of flight of signals. The distance between each hydrophone and the vehicle is obtained as

$$d_i = c(t_i - t_p) = \sqrt{(x - x_i)^2 + (y - y_i)^2 + (z - z_i)^2} \quad (4.59)$$

i : The index of each hydrophone,

$P_{vehicle} = (x, y, z)$: The unknown position of the vehicle,

$P_i = (x_i, y_i, z_i)$: The position of the i th hydrophone,

d_i : The distance between the vehicle and i th hydrophone,

c : The speed of the acoustic signal in the water,

t_p : The sending time of the acoustic signal from pinger,

t_i : The receiving time of the received signal from i th hydrophone.

The function f_i is obtained from Eqn. 4.59 for each hydrophone.

$$f_i(x, y, z, t_p) = \sqrt{(x - x_i)^2 + (y - y_i)^2 + (z - z_i)^2} - c(t_i - t_p) \quad (4.60)$$

The unknown position of the vehicle and the sending time of the acoustic signal from the pinger are found using optimization with the `fmincon` algorithm in MATLAB. The receiving time of signal for each hydrophone, t_i is needed to obtain position of the vehicle. Since the receiving signal of each hydrophone is noisy, they are filtered around 20 kHz using a bandpass filter. In order to obtain the receiving time, t_i for each hydrophone, peak times are detected from each filtered signal.

After the detection of the peak times of each receiving signals, the position of the vehicle in the acoustic-based measurement system is obtained using optimization with `fmincon` algorithm where the objective function, J defined in 4.61 is minimized:

$$\text{Minimize } J = \sum_{i=1}^n [d1_i - d2_i]^2 \quad (4.61)$$

subject to

$$\begin{aligned} 0 &\leq x \leq 6 \\ 0 &\leq y \leq 9 \\ 0 &\leq z \leq 2 \end{aligned}$$

where

$$d1_i = c(t_i - t_p) \quad (4.62)$$

$$d2_i = \sqrt{(x - x_i)^2 + (y - y_i)^2 + (z - z_i)^2} \quad (4.63)$$

Ultra Short Baseline (USBL)

This type of acoustic navigation systems vary according to the length of the baseline that is the distance between the active sensing acoustic transceivers. They are long baseline (LBL), short baseline (SBL) and ultra-short baseline (USBL). The baseline length of LBL and SBL are 100 - 6000 m and 20 - 50 m, respectively. The baseline length of USBL is less than 10 cm [37].

The USBL system consists of a transceiver and a transponder device. The transceiver device is located on a surface platform which generally is a vessel. The transponder device is located on the underwater vehicle, the position of which is unknown. The transceiver device is composed of three or more transducers. They are separated by the length of the baseline. The USBL measures both the range and the angle from the vehicle to the transceiver array as seen in Figure 4.8.

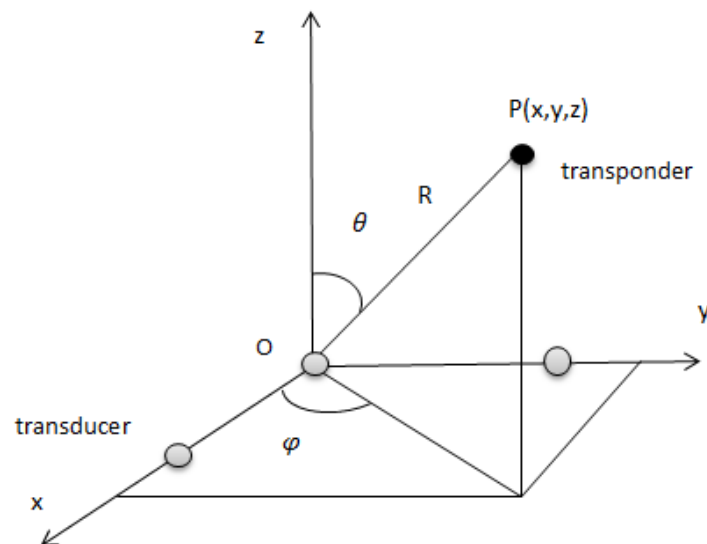


Figure 4.8: USBL range and angle measurement

Transceiver located on the surface vehicle transmits the acoustic signal. The transponder located on the underwater vehicle detects this acoustic signal and replies this signal. The transceiver array detects this return signal. The time of arrival is measured and converted into a range between underwater vehicle and surface vehicle [33].

The azimuth angle φ is expressed as the angle between the positive x - axis and the position vector of the underwater vehicle projected onto the horizontal $x - y$ plane.

The phase difference of the signal from underwater vehicle between two receivers in the array is measured with respect to the array's baseline. The azimuth angle, φ is defined from this measured phase difference. The elevation angle, θ is expressed as the angle between the positive z - *axis* and the position vector of the underwater vehicle. If a third receiver is used, the elevation angle can be obtained. Thus, the Cartesian coordinate of the underwater vehicle is obtained as [42]:

$$\begin{aligned}x &= R\sin\theta\cos\varphi \\y &= R\sin\theta\sin\varphi \\z &= R\cos\theta\end{aligned}\tag{4.64}$$

where

R : The distance between underwater vehicle and origin,

θ : The angle between the baseline of OP and positive z axis,

φ : The angle between the baseline of OP and positive x -axis.

4.5 Vision-based Navigation System

Vision-based navigation system consists of a camera. This camera is located above of the pool. Firstly, the four points are marked in the pool. While the vehicle moves around this square area, camera records position of the vehicle. The coordinates of the position data coming from camera is image coordinates. This position in the image coordinates should be transformed to world coordinates. The position data record from camera has some inaccuracy because of the light refraction and the surface mapping. The vehicle appears higher than the actual depth because of the light refraction. The position of the vehicle is recorded from the camera with light refraction effect. The depth of the vehicle appears at the point of z' in camera vision.

$$z' = z \frac{n_{weather}}{n_{water}}\tag{4.65}$$

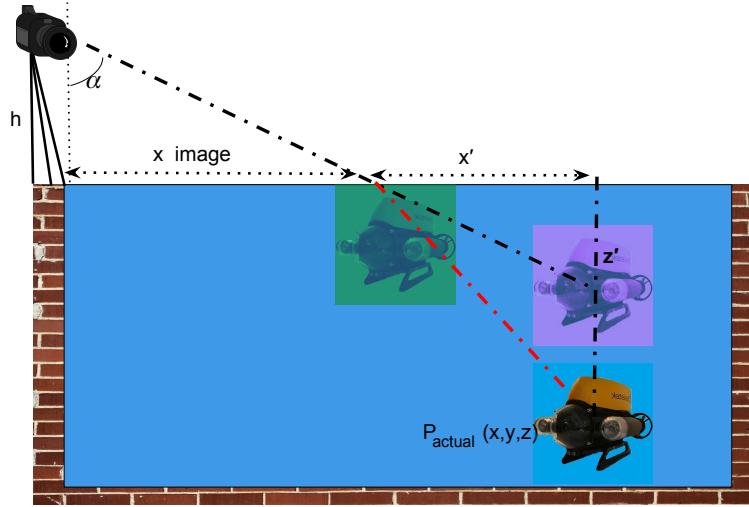


Figure 4.9: The schematic illustration of the vision-based navigation system

$$z' = 0.75z \quad (4.66)$$

where

z : Actual depth of the vehicle,

z' : Visible depth of the vehicle since light refraction,

$n_{weather}$: Refraction factor of the weather,

n_{water} : Refraction factor of the water.

Vision data has 2D coordinates (x and y -axes) and the position of the vehicle has 3 coordinates (x , y , z -axes). Image data does not include depth information. Because of this, the position coordinates of the vehicle which come from camera vision are mapped to surface coordinates. As seen from Fig. 4.9, from using the similarity of two triangles, surface coordinates of the vehicle are obtained.

$$\frac{h}{0.75z} = \frac{x_{image}}{x'} \quad (4.67)$$

$$x_{surface} = x_{image} + x' \quad (4.68)$$

$$y_{surface} = y_{image} \quad (4.69)$$

where

h : Height of the camera,

x_{image} : Vehicle position in the x-direction from camera vision,

y_{image} : Vehicle position in the y-direction from camera vision,

$x_{surface}$: Actual position in the x-axis of the vehicle,

$y_{surface}$: Actual position in the y-axis of the vehicle,

z : Actual depth of the vehicle.

4.6 External Aids

Magnetic compass, depth sensor and pitot tube are used for external aids. The attitude information of the vehicle comes from the magnetic compass. The pitot tube measures the velocity. Pressure sensor is used to support depth information.

4.7 Integrated Navigation

The advantages of using INS are that they send information nearly continuously, with a very high bandwidth and low short term noise. It measures the attitude and acceleration information of the vehicle. The position, linear and angular velocity are obtained by integration of these measured data. However, since the inertial errors increase with respect to time, the accuracy of the inertial navigation solution is low. Besides this, the accuracy of the vision-based and acoustic-based navigations is higher than the navigation solution of INS. The inertial navigation system, vision-based navigation system and acoustic-based navigation systems can be integrated to produce more

accuracy. In addition, the attitude, velocity and depth data are supported using the aiding sensors. All of these measured data are noisy; noise removal is done in the state estimation by using a Kalman filter algorithm. Multisensor data are fused using the direct Kalman filter algorithm. It is assumed that the data collection time of INS, magnetic compass, camera, acoustic-based navigation, pitot tube and depth sensor are $100Hz$, $10Hz$, $1Hz$, $10Hz$, $10Hz$, $10Hz$ respectively. IMU bias and random noise parameters are selected as $0.0001m/s^2$ and $0.0001(m/s^2)^2/Hz$, respectively.

4.7.1 Integration Architectures

Loosely-coupled integration architecture is used because of its simplicity and redundancy. The basic configuration of the integration architecture is shown in Figure 4.10. The integration algorithm is the indirect Kalman filter algorithm which compares the inertial navigation solution with the outputs of the vision-based and acoustic-based navigations and the outputs of the aiding sensors which are attitude, velocity and depth measurements. Also, the integration algorithm estimates corrections to inertial position, velocity and attitude solution. This corrected INS navigation solution forms the integrated navigation solution [20].

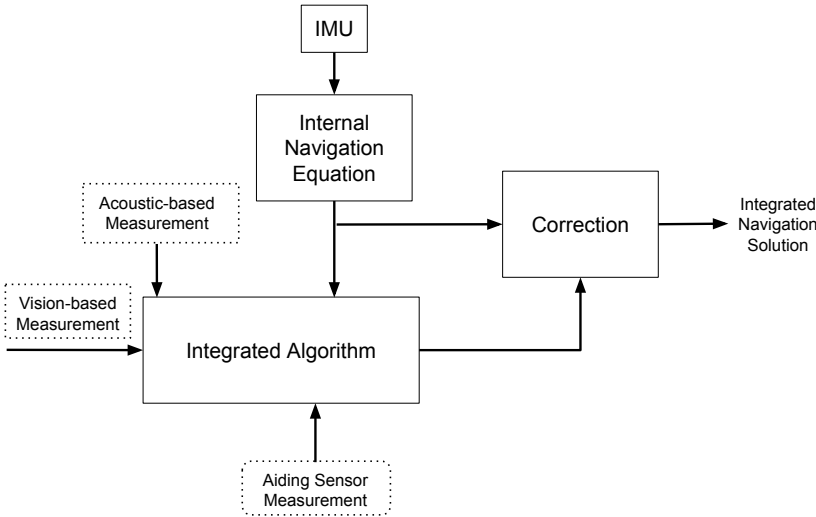


Figure 4.10: Integrated Navigation Architecture

4.7.2 Correction

INS correction architecture varies with respect to open-loop and closed-loop configurations. Although, in the closed loop configuration Kalman filter outputs; estimated, position, velocity and attitude errors, are fed back to inertial navigation processor, in the open-loop configuration, they are not fed back to the INS. In this study, the open-loop configuration is adopted.

The corrected inertial navigation solution, $\hat{C}_b^e, \hat{v}_b^e, \hat{r}_b^e$, are obtained using the raw inertial navigation solution, $\tilde{C}_b^e, \tilde{v}_b^e, \tilde{r}_b^e$ and integration algorithm solution, $\delta\hat{C}_b^e, \delta\hat{v}_b^e, \delta\hat{r}_b^e$. Since the reference and resolving frames are chosen as the Earth frame, they are expressed in the ECEF frame coordinates [20].

$$\hat{C}_b^e = \delta\hat{C}_b^e \tilde{C}_b^e \quad (4.70)$$

$$\hat{v}_{eb}^e = \tilde{v}_{eb}^e - \delta\hat{v}_b^e \quad (4.71)$$

$$\hat{r}_{eb}^e = \tilde{r}_{eb}^e - \delta\hat{r}_{eb}^e \quad (4.72)$$

If a small angle approximation is made, applicable, attitude error yields:

$$\hat{C}_b^e \approx \left(I_3 - \left[\delta\hat{\psi}_{eb}^e \wedge \right] \right) \tilde{C}_b^e \quad (4.73)$$

where $\delta\hat{\psi}_{eb}^e$ is the estimated attitude error of INS body frame with respect to earth frame and resolving about the earth frame. It comes from the output of the Kalman filter algorithm.

4.7.3 System Model and State Selection

Error state estimation is adopted in the indirect Kalman filter algorithm. The error states are chosen as the error of attitude, velocity and position of the vehicle which

are expressed in the ECEF frame coordinates, $\delta\varphi_{eb}^e$, δv_{eb}^e , δr_{eb}^e respectively. The bias error of the accelerometer, b_a and the bias of the gyroscope, b_g are added in the error states. Thus, the state vector is comprised of 15 states as [20]

$$x = \begin{pmatrix} \delta\varphi_{eb}^e \\ \delta v_{eb}^e \\ \delta r_{eb}^e \\ b_a \\ b_g \end{pmatrix} \quad (4.74)$$

The attitude error is defined with respect to angular rate error and corrected transformation matrix is given by

$$\dot{\delta\varphi}_{eb}^e = \hat{C}_b^e (\tilde{w}_{eb}^b - w_{eb}^e) \quad (4.75)$$

Estimated quantities are represented by ($\hat{\quad}$) and the measured quantities are represented by ($\tilde{\quad}$). Applying the equations 4.55 and 4.56,

$$\begin{aligned} \dot{\delta\varphi}_{eb}^e &= \hat{C}_b^e \delta w_{ib}^b - \hat{C}_b^e (\tilde{C}_e^b - C_e^b) w_{ie}^e \\ \dot{\delta\varphi}_{eb}^e &= \hat{C}_b^e \delta w_{ib}^b - \Omega_{ie}^e \delta\varphi_{eb}^e \end{aligned} \quad (4.76)$$

The rate of change of the attitude error is written in terms of the Kalman filter states as

$$\partial\dot{\varphi}_{eb}^e = \hat{C}_b^e b_g - \Omega_{ie}^e \partial\varphi_{eb}^e \quad (4.77)$$

The time derivative of the Earth-referenced velocity was given as

$$v_{eb}^e (+) = v_{eb}^e (-) + v_{ib}^e + g_b^e (r_{eb}^e (-)) - 2\Omega_{ie}^e v_{eb}^e (-) \tau_i \quad (4.78)$$

The rate of change of the velocity error is

$$\delta \dot{v}_{eb}^e \approx - \left(\hat{C}_b^e \hat{f}_{ib}^b \right) \wedge \delta \varphi_{eb}^e - 2\Omega_{ie}^e \delta v_{eb}^e + \frac{2g_0 \left(\hat{L}_b \right)}{r_{eS}^e \left(\hat{L}_b \right)} \frac{\hat{r}_{eb}^e}{|\hat{r}_{eb}^e|^2} \hat{r}_{eb}^{eT} \delta r_{eb}^e + \hat{C}_b^e b_a \quad (4.79)$$

Since the gravity error depends on the position error, and variation of gravity due to change in local position is small in our application, they are neglected. Hence, the rate of change of the velocity error is

$$\partial \dot{v}_{eb}^e = \hat{C}_b^e b_a - \left(\hat{C}_b^e \hat{f}_{ib}^b \right) \wedge \partial \varphi_{eb}^e - 2\Omega_{ie}^e \partial v_{eb}^e \quad (4.80)$$

The time derivative of the position error is expressed in the ECEF frame as

$$\partial \dot{r}_{eb}^e = \partial v_{eb}^e \quad (4.81)$$

The time derivative of the accelerometer and gyro biases is assumed as zero.

$$\dot{b}_a = 0 \quad \dot{b}_g = 0 \quad (4.82)$$

In the end, the system model is written in the standard form as

$$\dot{x} = Fx + Qw \quad (4.83)$$

$$\begin{bmatrix} \delta \dot{\varphi}_{eb}^e \\ \delta \dot{v}_{eb}^e \\ \delta \dot{r}_{eb}^e \\ \dot{b}_a \\ \dot{b}_g \end{bmatrix} = \begin{bmatrix} -\Omega_{ie}^e & 0_3 & 0_3 & 0_3 & \hat{C}_b^e \\ -\hat{C}_b^e \hat{f}_{ib}^b \wedge & -2\Omega_{ie}^e & 0_3 & \hat{C}_b^e & 0_3 \\ 0_3 & I_3 & 0_3 & 0_3 & 0_3 \\ 0_3 & 0_3 & 0_3 & 0_3 & 0_3 \\ 0_3 & 0_3 & 0_3 & 0_3 & 0_3 \end{bmatrix} \begin{bmatrix} \delta \varphi_{eb}^e \\ \delta v_{eb}^e \\ \delta r_{eb}^e \\ b_a \\ b_g \end{bmatrix} \quad (4.84)$$

where w is the system noise which is assumed to be zero-mean Gaussian noise and Q is the system noise covariance matrix defined as [20].

$$Q = \begin{pmatrix} S_{rg}^2 I_3 & 0_3 & 0_3 & 0_3 & 0_3 \\ 0_3 & S_{ra}^2 I_3 & 0_3 & 0_3 & 0_3 \\ 0_3 & 0_3 & 0_3 & 0_3 & 0_3 \\ 0_3 & 0_3 & 0_3 & S_{bad}^2 I_3 & 0_3 \\ 0_3 & 0_3 & 0_3 & 0_3 & S_{bgd}^2 I_3 \end{pmatrix} \tau_s \quad (4.85)$$

where S_{rg} , S_{ra} , S_{bad} and S_{bgd} are the power spectral densities of gyro random noise, accelerometer random noise, accelerometer bias variation and gyro bias variation, respectively. They are defined as [20]

$$S_{rg} = \sigma_{rg}^2 \tau_i \quad S_{ra} = \sigma_{ra}^2 \tau_i \quad (4.86)$$

$$S_{bad} = \frac{\sigma_{bad}^2}{\tau_{bad}} \quad S_{bgd} = \frac{\sigma_{bgd}^2}{\tau_{bgd}} \quad (4.87)$$

The values of σ_{rg}^2 , σ_{ra}^2 are the standard deviation of the noise on the accelerometer specific force measurement and gyro angular rate measurement, respectively. The values of S_{bad}^2 and S_{bgd}^2 are the standard deviation of the accelerometer and gyro dynamic biases, respectively. The value of τ_i is the interval between the input of the successive accelerometer and gyro outputs to the inertial navigation equations [20].

The digital implementation of the integrated navigation system requires discrete representation of the state and error model. The discrete equivalent of the continuous differential equations can be expressed as:

$$x_{k+1} = \Phi_k x_k + w_k \quad (4.88)$$

The state transition matrix Φ_k is derived from the system dynamics matrix F and time range $\Delta t = t_{k+1} - t_k$ [9]. This matrix is assumed to be constant during the sampling interval. The second and higher order terms in the expansion below are neglected.

$$\Phi_k = e^{F\Delta t} = I + F\Delta t + \frac{(F\Delta t)^2}{2!} + \dots \quad (4.89)$$

4.7.4 Measurement Model

Since the measurements are taken at discrete intervals, the measurement vector is modeled as:

$$z_k = H_k x_k + v_{mk} \quad (4.90)$$

where H_k is the measurement matrix, x_k is the state vector and v_{mk} represents the white noise sources and k represents the measurement update iteration. The measurement model is composed of the attitude, velocity and position errors. The attitude data comes from IMU and magnetic compass. The velocity data comes from IMU and pitot tube. The position data is comes from IMU and the vision-based and acoustic-based measurement system. In addition, the depth information is supported with depth sensor. The vision and acoustic based measurement system act like GPS in order to support the position of the vehicle. The IMU data rate is taken as the reference data rate (i.e., the highest data collection rate among measurements). The measurement noise is assumed as the zero mean Gaussian noise. The measurement matrix for the Kalman filter in the open loop architecture is given by:

$$z = \tilde{m}_{sensor_i} - \tilde{m}_{imu} \quad (4.91)$$

where the value of \tilde{m}_{imu} is the measured data which comes from inertial sensor and the value of \tilde{m}_{sensor_i} is the measured data which comes from i th sensor. The attitude error is the difference between the magnetic compass data and the inertial sensor data. The velocity error is the difference between pitot tube data and inertial sensor data. The position error is difference between the i th sensor and inertial sensor. The position data comes from more than two sensors. The position data of i th sensor is taken from vision-based measurement system, acoustic-based measurement system and the depth sensor, respectively. IMU, camera, acoustic-based measurement system and depth sensor are added according to their accuracy to the indirect Kalman filter algorithm, respectively. The position error becomes the difference between the i th sensor data and the estimated (corrected) position data which comes from previous integrated navigation solution as sensors are added.

In order to obtain the measurement matrix, H_k , the measurement innovation vector should be defined. The measurement innovation vector is composed of the differences between the i th sensor which acts like GPS and the corrected inertial attitude, velocity and position solutions, accounting for the lever arm from the INS to the GNSS antenna, l_{ba}^b . The measurement innovation vector related to the earth frame is obtained for loosely coupled integration as [20]

$$\partial z_k^e = \begin{bmatrix} \delta\varphi_{eb}^e \\ \delta v_{eb}^e \\ \delta r_{eb}^e \end{bmatrix} = \begin{bmatrix} \hat{\varphi}_{mc}^e - \hat{\varphi}_{ebIMU}^e \\ \hat{v}_{pt}^e - \hat{v}_{ebIMU}^e - \hat{C}_b^e (\hat{w}_{ib}^b \wedge l_{ba}^b) + \Omega_{ie}^e \hat{C}_b^e l_{ba}^b \\ \hat{r}_{sensor_i}^e - \hat{r}_{ebIMU}^e - \hat{C}_b^e l_{ba}^b \end{bmatrix} \quad (4.92)$$

The measurement matrix is obtained as

$$H_k = \left. \frac{\partial h(x)}{\partial x} \right|_{x=\hat{x}_k^-} = \left. \frac{\partial z(x)}{\partial x} \right|_{x=\hat{x}_k^-} \quad (4.93)$$

Using the measurement innovation vector and the state vector, the measurement matrix in the ECEF frame becomes as [20]

$$H_k = \begin{bmatrix} -I_3 & 0_3 & 0_3 & 0_3 & 0_3 \\ [(\hat{C}_b^e (\hat{w}_{ib}^b \wedge l_{ba}^b) - \Omega_{ie}^e \hat{C}_b^e l_{ba}^b) \wedge] & -I_3 & 0_3 & 0_3 & \hat{C}_b^e [l_{ba}^b \wedge] \\ [\hat{C}_b^e l_{ba}^b \wedge] & 0_3 & -I_3 & 0_3 & 0_3 \end{bmatrix} \quad (4.94)$$

Since the lever arm is weak, the relationship of attitude errors and gyro biases is weak. Hence, the measurement matrix is simplified as [20]

$$H_k^e = \begin{bmatrix} -I_3 & 0_3 & 0_3 & 0_3 & 0_3 \\ 0_3 & -I_3 & 0_3 & 0_3 & 0_3 \\ 0_3 & 0_3 & -I_3 & 0_3 & 0_3 \end{bmatrix} \quad (4.95)$$

The diagonal terms of the measurement covariance matrix R are the variances of each measurement, and the off-diagonal terms represent the correlation between the different components of the measurement noise. In this application, the noise on each

component of the measurement vector is independent. So, R is a diagonal matrix as [20]

$$R = \begin{bmatrix} R_a I_3 & 0_3 & 0_3 \\ 0_3 & R_v I_3 & 0_3 \\ 0_3 & 0_3 & R_p I_3 \end{bmatrix} \quad (4.96)$$

The value of the R_a , R_v and R_p are related to the standard deviation of the measured attitude, measured velocity, and measured position, σ_a , σ_v , σ_p respectively. Since the accuracy of the each sensor is different, this matrix is changed as a new sensor is added.

4.7.5 Estimation Algorithm

A Kalman Filter is an estimation algorithm is used to produce error estimates and measurement estimates of the states and integrate the INS-indicated quantities with the available external measurements. The Kalman Filter is an efficient recursive filter that estimates the state of a linear dynamic system from a series of noisy measurements. It uses the system model to propagate the state and error covariance in time. Then, using the measurement and the corresponding measurement error information, and comparing those with the predicted measurements, the state estimate and state error covariance are updated in an optimal way. Indirect Kalman filter algorithm is defined as follow [16].

Discrete time state space model is formed as:

$$x_{k+1} = \Phi_k x_k + w_k$$

$$y_k = H_k x_k + v_k$$

where w_k is the system noise and v_k is the measurement noise. The value of w_k and v_k are independent, zero-mean Gaussian noise. Q_k is the system covariance matrix and R_k is the measurement covariance matrix.

Initialization of state and error covariance, for $k = 0$ is set:

$$\hat{x}_0 = E[x_0]$$

$$P_0 = E[(x_0 - E[x_0])(x_0 - E[x_0])^T]$$

Propagation and update computation for $k = 1, 2, \dots$, is performed as:

State estimation propagation

$$\hat{x}_{k+1}^- = \Phi_k \hat{x}_k^+$$

Error covariance propagation

$$P_{k+1}^- = \Phi_k P_k^+ \Phi_k^T + Q_k$$

Kalman gain matrix is

$$K_{k+1} = P_{k+1}^- H_{k+1}^T [H_{k+1} P_{k+1}^- H_{k+1}^T + R_{k+1}]^{-1}$$

State estimate update using measurement matrix, z_{k+1}

$$\hat{x}_{k+1}^+ = \hat{x}_{k+1}^- + K_{k+1} [z_{k+1} - H_{k+1} \hat{x}_{k+1}^-]$$

Error covariance update

$$P_{k+1}^+ = [I - K_{k+1} H_{k+1}] P_{k+1}^-$$

4.7.6 Simulation Results

The 3D motion is realized by a suitable combination of the right, left and vertical thrusters. The actual position, velocity and attitudes coming from mathematical model response are shown in Figures 4.11, 4.12 and 4.13, respectively.

The actual acceleration coming from model response and the measured (generated) acceleration from IMU are shown in Figure 4.14. The actual angular rate coming from model response and the measured (generated) angular rate from IMU are shown in Figure 4.15.

The translational velocities of the IMU are obtained by integrating the measured translational accelerations. Figure 4.16 shows the obtained velocity of IMU and the measured velocity from pitot tube and the actual velocity from model response.

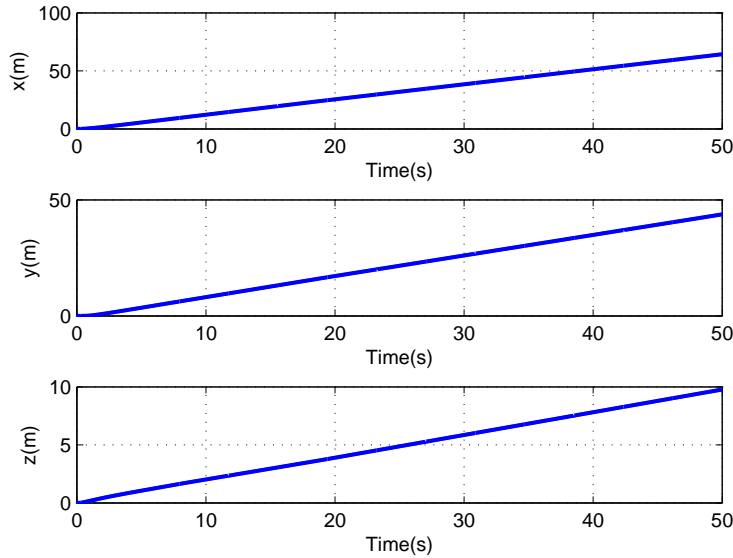


Figure 4.11: Actual position with respect to time in the Earth frame

The rotational positions (attitudes) of the IMU are obtained by integrating the measured rotational velocity data. Figure 4.17 shows the obtained attitudes of IMU and the measured attitude data coming from the magnetic compass and the actual attitude data coming from the model response.

The translational positions of the IMU are obtained by integrating the translational velocity data. Figure 4.18 shows the obtained translational position of IMU.

Figure 4.19 shows the actual and the estimated surge, sway and heave velocity error in the Earth frame. These estimated translational velocities are used for correction. The inertial navigation solution (output of the correction), corrected translational velocities, are shown in Figure 4.20.

Figure 4.21 shows the actual and the estimated roll, pitch, yaw angle errors in the Earth frame. These estimated rotational positions are used for correction. The inertial navigation solution (output of the correction), corrected rotational positions, are shown in Figure 4.22.

Figures 4.23 and 4.24 show the actual translational position and the estimated (corrected) translational position in x and y axes, respectively. Firstly, IMU and camera

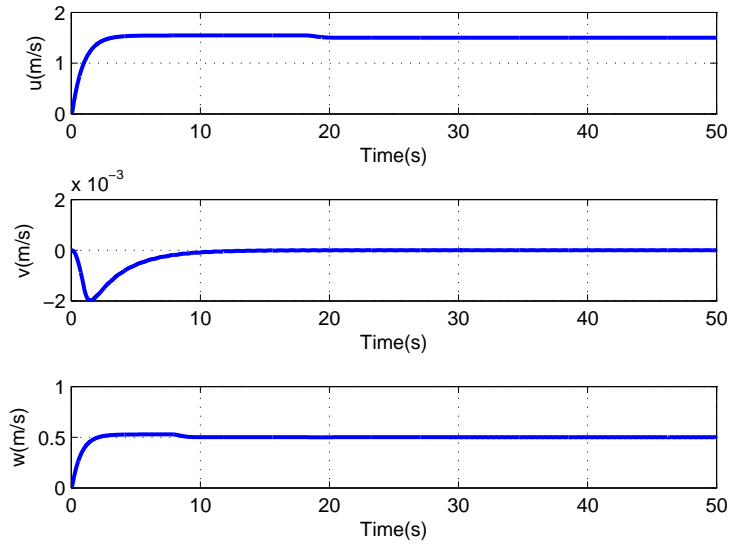


Figure 4.12: Actual velocity with respect to time in the body coordinate frame

data are integrated. Its navigation solution, corrected position, is shown with green line. Then, this corrected data and acoustic data are integrated. Its navigation solution, corrected position in x and y-axes are shown with red line in Fig. 4.23 and Fig. 4.24, respectively.

Since the vision data does not have depth information, the camera cannot use the integrating navigation solution for the translational position in the z-axis. Fig. 4.25 shows the actual depth and the estimated (corrected) depth, respectively. Firstly, IMU and acoustic data are integrated. Its navigation solution, corrected depth, is shown with green line. Then, this corrected data and the data from depth sensor are integrated. Its navigation solution, corrected depth is shown with red line in Fig. 4.25.

4.8 Conclusion

The navigation data is important for system identification. There are many navigation system for the obtaining the position of the vehicle. In this study, state propagation equations of the inertial navigation system are used as an artificial vehicle model. The acoustic-based navigation system, vision-based navigation systems are used to

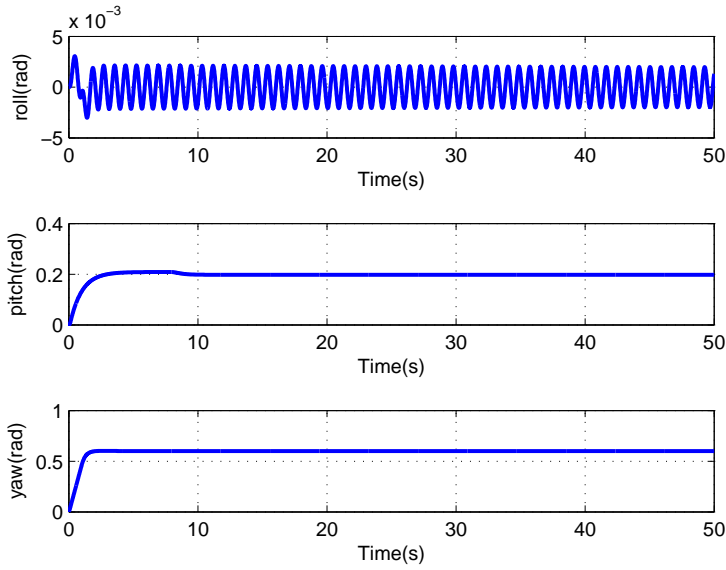


Figure 4.13: Actual attitude with respect to time in the Earth frame

act like GPS and the aiding sensors are used to support the attitude and depth data. Since the accuracy of the obtaining the position from inertial sensor is low an integrated navigation system is composed. Measured data are generated from model response of the vehicle according to accuracy of their measurements. System and measurement models have been constructed for estimation. The error state implementation is adopted in the Kalman filter algorithm. The outputs of the Kalman filter are the estimated state errors. They are used for correction. The inertial navigation solutions are corrected states. They are used in Chapter 7 in simulation-based system identification study.

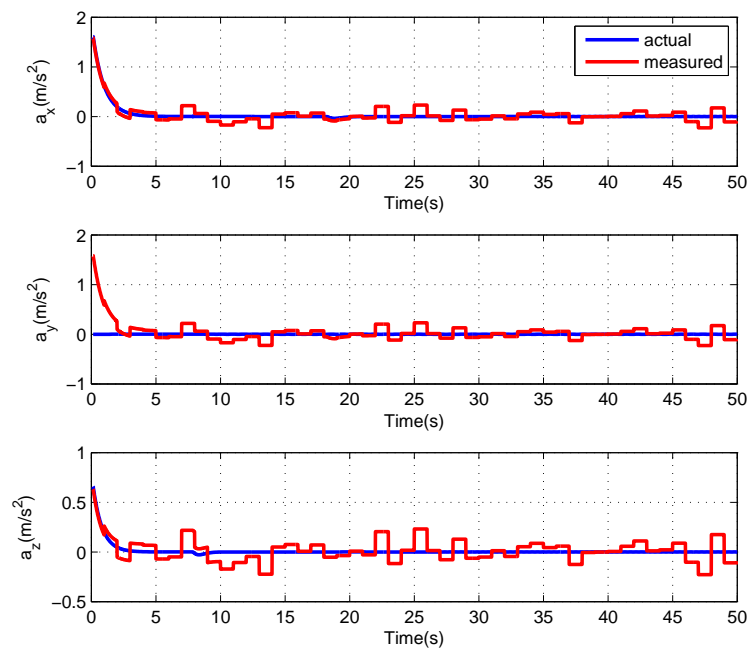


Figure 4.14: Actual and measured acceleration from IMU in the body coordinate frame

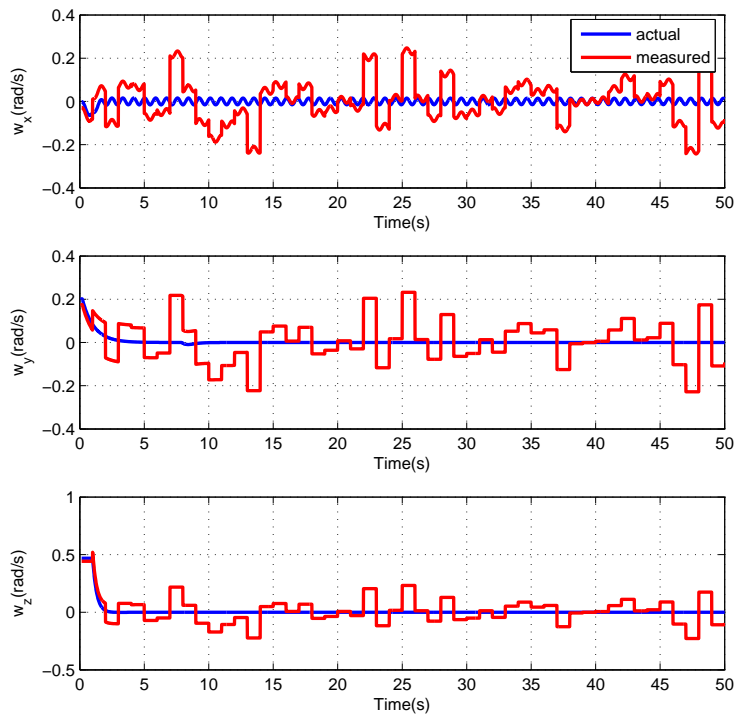


Figure 4.15: Actual and measured angular rate from IMU in the body coordinate frame

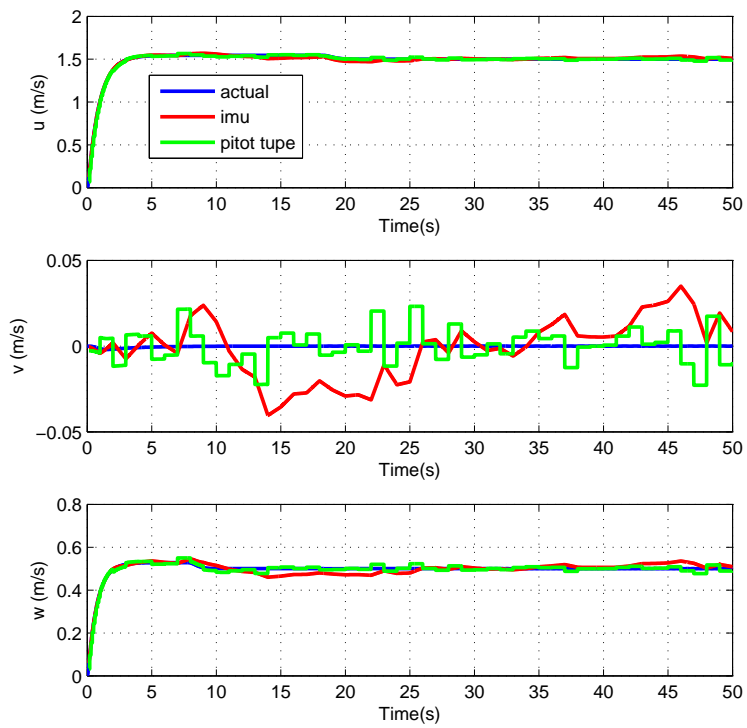


Figure 4.16: Actual velocity (blue line) and obtained velocity from IMU (red line) and the measured velocity from pitot tupe (green line) in the body coordinate frame

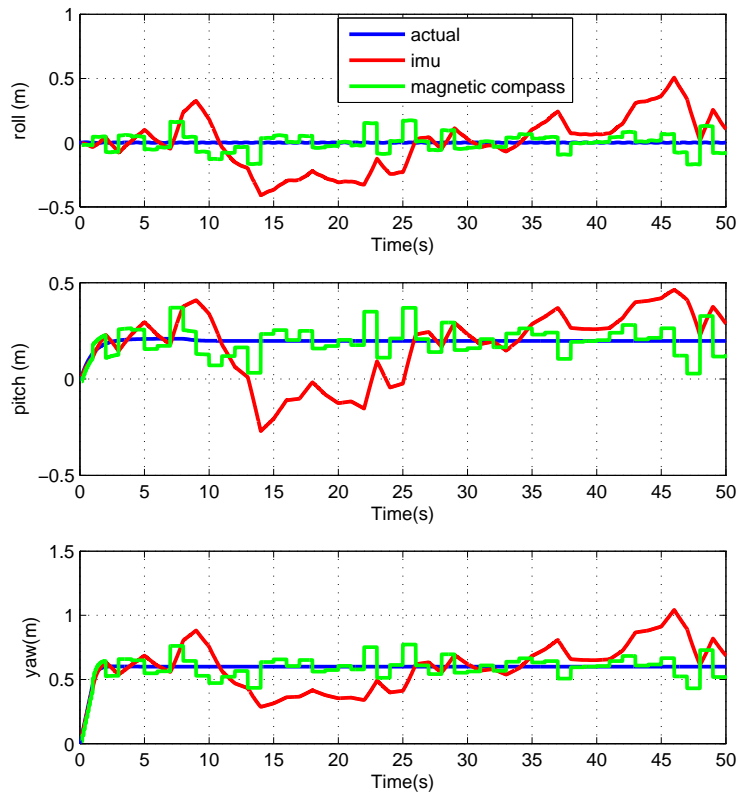


Figure 4.17: Actual attitude (blue line) and obtained attitude from IMU (red line) and the measured attitude from magnetic compass (green line) in the Earth coordinate frame

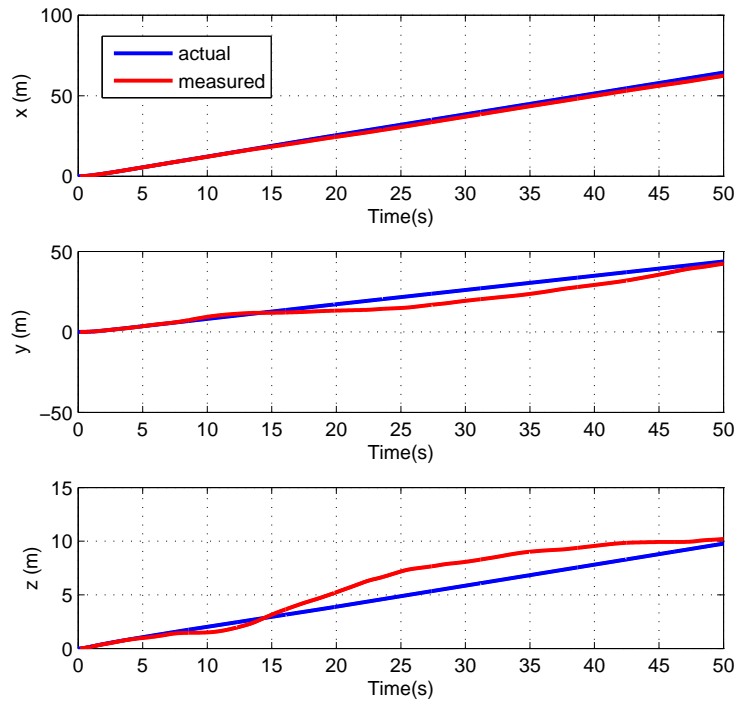


Figure 4.18: Actual and obtained position from IMU in the ECEF coordinate frame

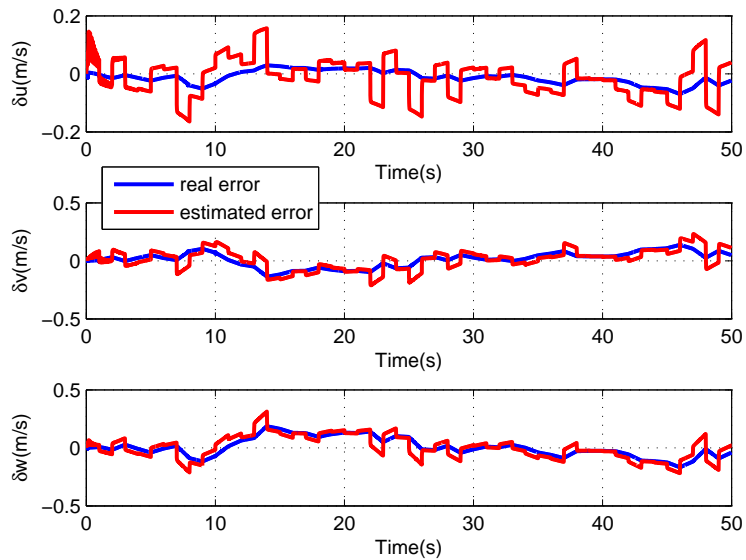


Figure 4.19: Estimated surge, sway and heave speed error from solution of the integrating IMU and pitot tube data (red line) and the actual error (blue line)

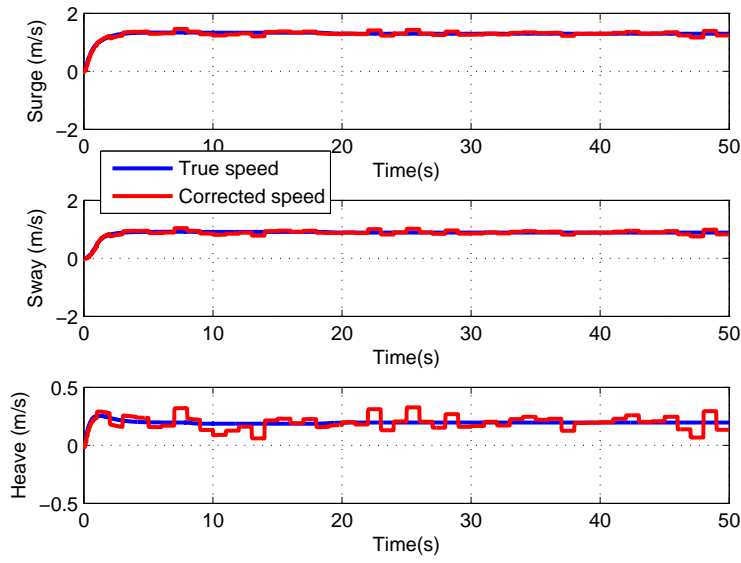


Figure 4.20: The actual surge, sway and heave speed (blue line) and the corrected surge, sway and heave speed (red line)

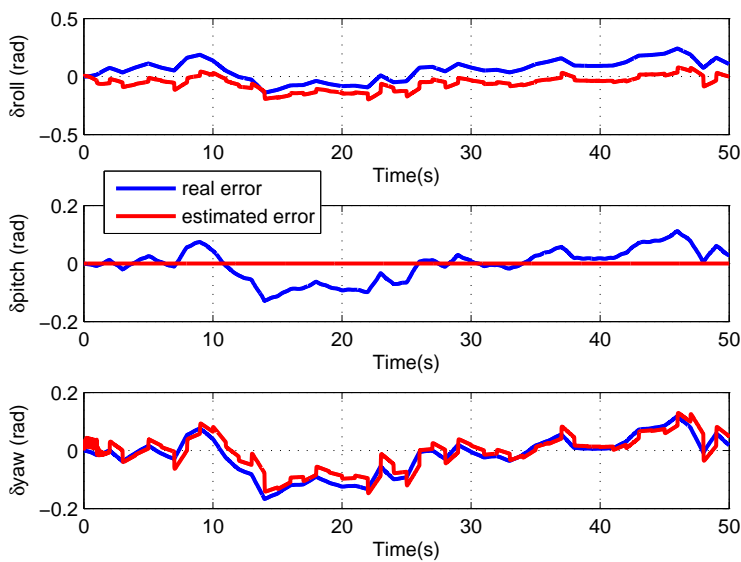


Figure 4.21: Estimated roll, pitch and yaw angle error from solution of the integrating IMU and magnetic compass data (red line) and the real error (blue line)

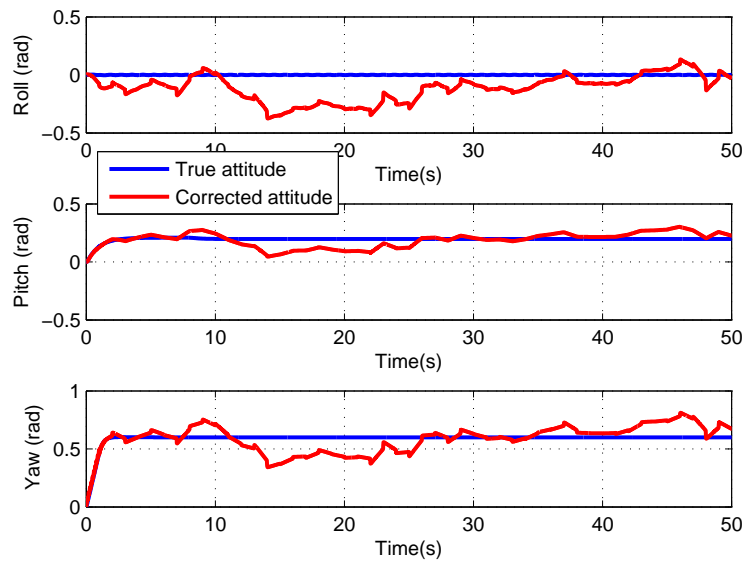


Figure 4.22: The actual roll, pitch and yaw angle (blue line) and the corrected roll, pitch and yaw angle (red line)

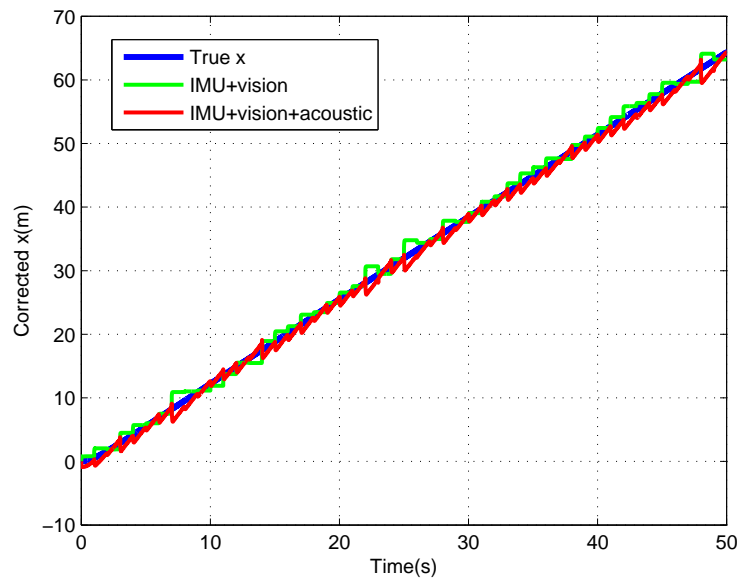


Figure 4.23: The actual position in the x-axis (blue line), Estimated (corrected) position in the x axis for 2 cases: integrating IMU data and camera data (green line), integrating IMU data, vision data and acoustic data (red line)

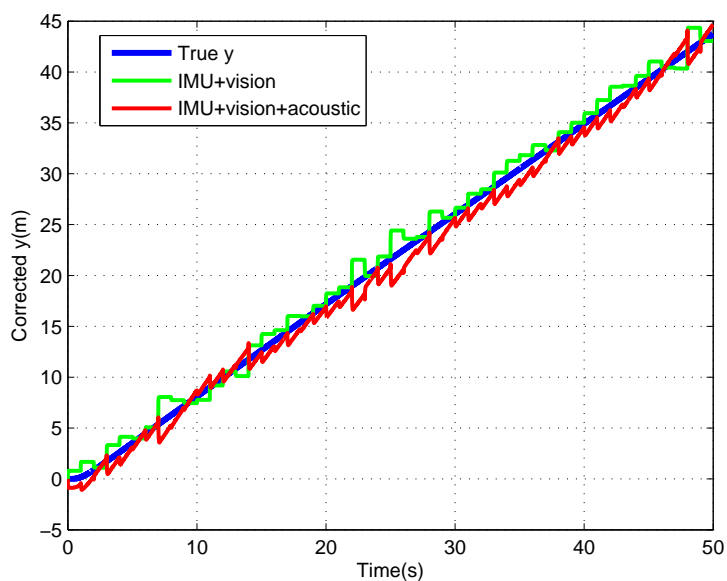


Figure 4.24: The actual position in the y-axis (blue line), Estimated (corrected) position in the y axis for 2 cases: integrating IMU data and vision data (green line), integrating IMU data, vision and acoustic data (red line)

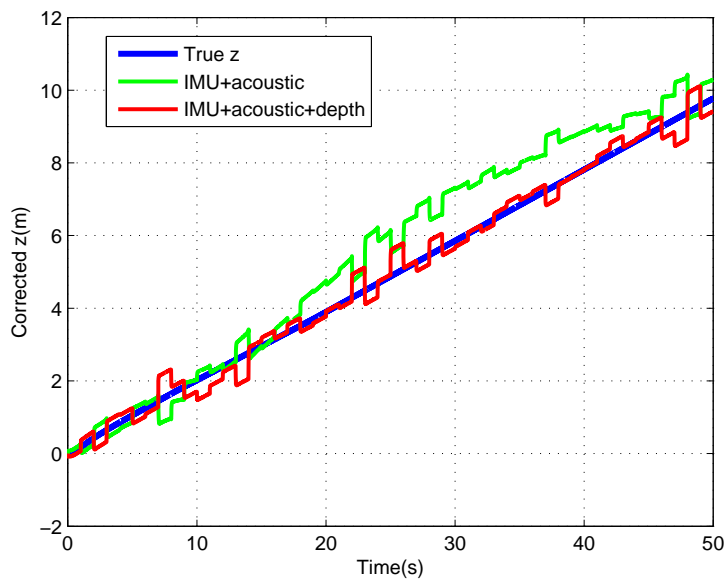


Figure 4.25: The actual depth (blue line), Estimated (corrected) depth for 2 cases: integrating depth data coming from inertial navigation and acoustic-based navigation (green line), integrating depth data coming from inertial navigation, acoustic-based navigation and depth sensor (red line)

CHAPTER 5

GUIDANCE

5.1 Introduction

The guidance system of an underwater vehicle is the key to achieve autonomous operation as well as to optimize energy, time etc. during the missions. Some important UUV guidance found in the literature are [3]:

- Way point guidance by line of sight,
- Vision based guidance.
- Lyapunov based guidance,
- Guidance using chemical signals,
- Proportional navigation guidance for AUV's,
- Guidance using magnetometers for cable tracking,
- Electromagnetic guidance.

The way point guidance by line of sight strategy is the most widely used. In this study, the algorithm of the way point guidance by line of sight (LOS) is used for the yaw and pitch planes and the 3D motion for SAGA. In addition, the guidance based on optimal control for the 3D motion are examined. While the vehicle moves, measured position, velocity and attitude data come from sensors. The desired position and the actual position come from navigation system are the reference value of the guidance system. The output of the guidance system, command speed and position values and

the measured data from sensors are the reference values of the controllers. Then, the output of the controller is the force input of the vehicle's dynamics. For the general view of SAGA, the navigation system, guidance, controller and ROV dynamic model are combined. The schematic illustration of the combined system of SAGA is shown in Fig. 5.1.

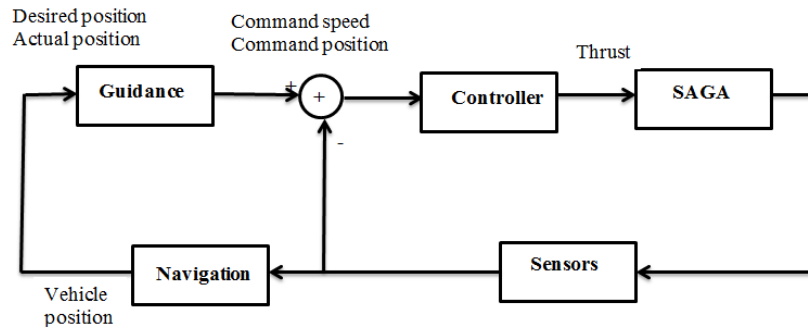


Figure 5.1: The schematic illustration of the combined system, navigation, controller, guidance and vehicle dynamics

5.2 Way Point Guidance by LOS

Basic line of sight algorithm described by Lienard, Healey [21] and Fossen is the simplest of waypoint guidance methods. The algorithm in $2D$ guidance is improved between two points $x_d(t_0), y_d(t_0)$ and $x_d(t_f), y_d(t_f)$ by splitting the path between those into a number of way points $x_d(k), y_d(k)$ for $k = 1, 2, \dots, N$ as shown in Fig. 5.2. First target way point is called as the actual way point. Then, if the vehicle reaches a location close to the first target way point, the next target. This procedure is continued until the vehicle reaches the final target point.

In a similar way, for the $3D$ motion implementation, guidance problem is redefined as the path between two points $x_d(t_0), y_d(t_0), z_d(t_0)$ and $x_d(t_f), y_d(t_f), z_d(t_f)$ by splitting the path between those into a number of way points $x_d(k), y_d(k), z_d(k)$ for $k = 1, 2, \dots, N$.

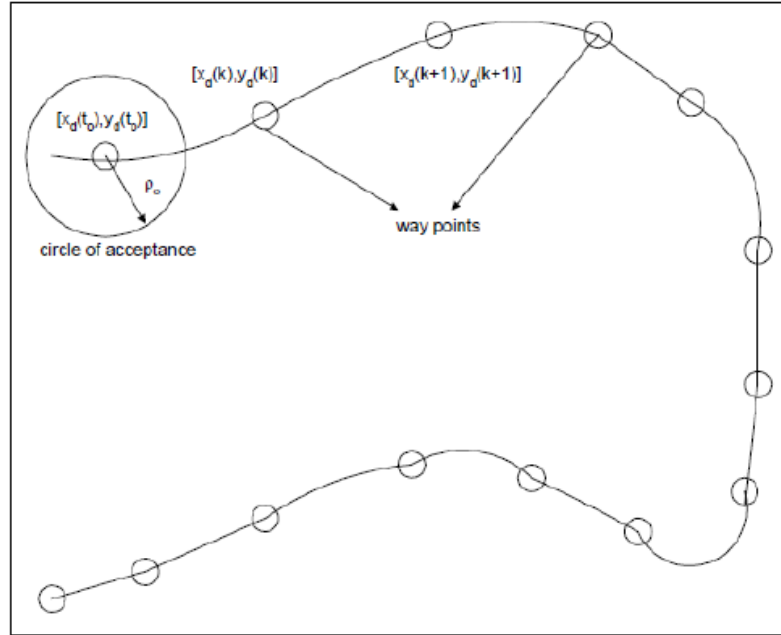


Figure 5.2: Way point guidance and circle of acceptance [21]

5.2.1 Way Point Guidance in the Yaw Plane

The schematic illustration of the yaw plane motion is shown in Fig. 5.3. While the vehicle moves, measured data data which comes from sensor are estimated with navigation system. The outputs of the navigation system are the estimated position of the vehicle in the x-axis and the estimated yaw angle. These estimated data and the desired position in x and y axes are the input of the guidance system. The way point guidance system produces the command position in the x-axis and the command yaw angle. They are the input values of the controllers. Controllers produce force for the right and left thrusters. They are inputs of the vehicle's model.

Basic line of sight algorithm produces the reference yaw angle and the reference position-x. In the Fig. 5.4, $P(x, y)$ represents the current position of the vehicle (actual position) and $P_i = (x_i, y_i)$ represents the current way point position. Distance between the actual position of the vehicle and the current way point is defined by d_{pi} . The reference yaw angle and LOS angle are represented by φ_r and φ_{r0} respectively. The radius of circle of acceptance is denoted by ρ_0 [3].

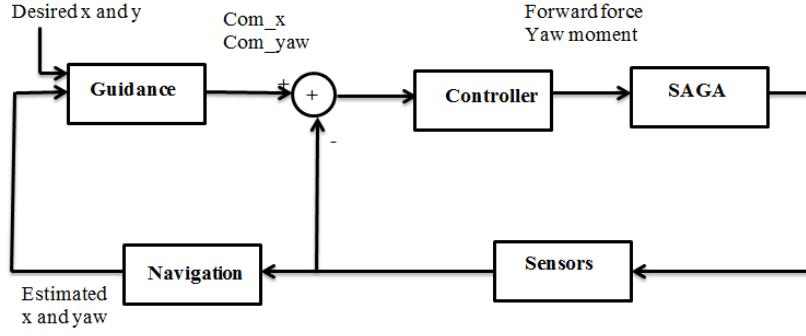


Figure 5.3: The schematic illustration of the combined system for the yaw plane motion

Since the difference between the reference yaw angle and the LOS angle is zero, $\varphi_r = \varphi_{r0}$, the way point is located in front of the vehicle. The LOS angle, φ_{r0} is computed as in Equation 5.1 by the four quadrant inverse tangent function [3].

$$\tan(\psi_{r0}) = \frac{y_i - y}{x_i - x} \quad (5.1)$$

When the vehicle enters a circle of acceptance around the way point, the current way point P_i is accepted to have been reached. This condition occurs when the distance d_{pi} is smaller than ρ_0 as defined in Eqn. 5.2, then, the next way point is selected.

$$d_{pi} = \sqrt{(x_i - x)^2 + (y_i - y)^2} < \rho_0 \quad (5.2)$$

Way point guidance by LOS is designed in Simulink/Matlab environment. As an example, the desired points are given as:

$$\begin{aligned} x_i &= [0 \quad 20 \quad 40 \quad 70 \quad 90 \quad 110 \quad 120 \quad 140 \quad 160] \\ y_i &= [0 \quad 40 \quad 90 \quad 70 \quad 50 \quad 80 \quad 120 \quad 110 \quad 60] \end{aligned} \quad (5.3)$$

The Figure 5.5 shows the simulation result for the way point guidance by LOS for the yaw plane motion. As seen in the Fig. 5.5, the vehicle reaches the desired points the using navigational data. If the weight of the thruster of the vehicle is small, the vehicle moves smoother path [13]. But, if the weight of thrusters of the vehicle is

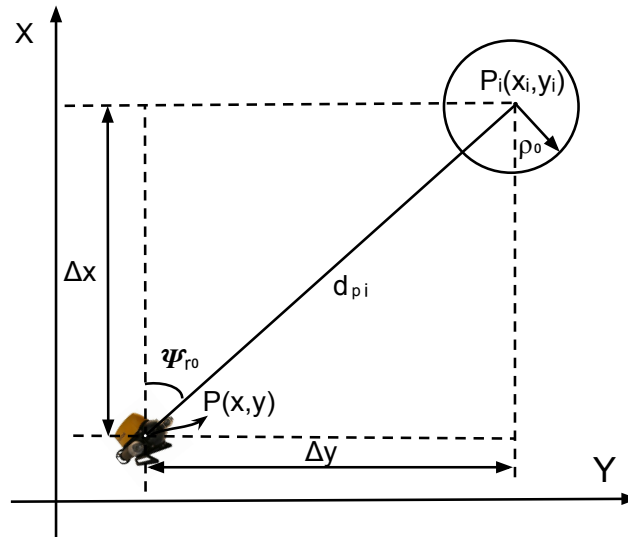


Figure 5.4: Basic Line of Sight Guidance for the yaw plane

very large, some the desired way point cannot be reached. This problem was solved by V. Bakaric, Z. Vukic, and R. Antonic [3].

Figure 5.6 shows the guidance between points, (x, y) from $(0, 0)$ to $(20, 40)$. As seen figure, the vehicle first rotates with desired attitude then goes to the desired point with the way point algorithm by LOS.

5.2.2 Way Point Guidance in the Pitch Plane

The schematic illustration of the pitch plane motion is shown in Fig. 5.7. While the vehicle moves, measured data which comes from the sensors are estimated with the navigation system. The outputs of the navigation system are the estimated position of the vehicle in x and z axes. These estimated data and the desired position in x and z axes are the input of the guidance system. The way point guidance system produces the command position in x and z axes. They are the input values of the controllers. Controllers produce force for the right and left thrusters (equal force and same direction) and the vertical thruster. They are inputs of the vehicle's model.

The LOS angle in the pitch angle θ is obtained from the vehicle from its current

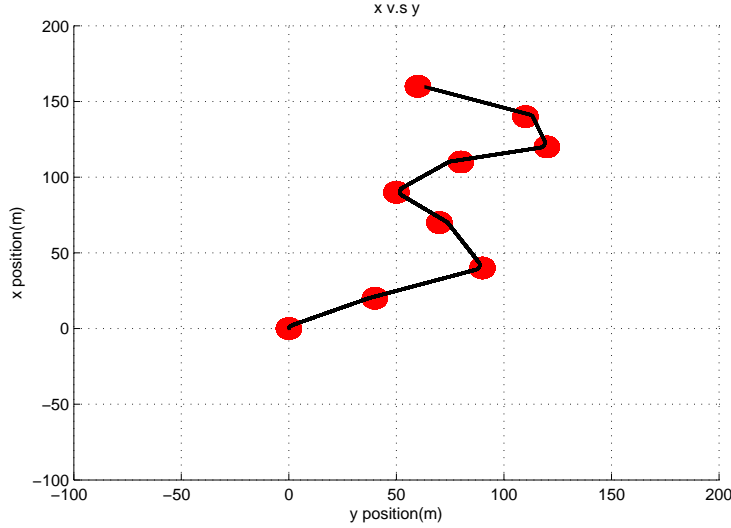


Figure 5.5: Way point guidance by LOS in the yaw plane

position $V(x, z)$ towards the current way point $P_i = (x_i, z_i)$ as

$$\tan(\theta) = \frac{z_i - z}{x_i - x} \quad (5.4)$$

Since the vertical thruster of the SAGA is located near the CG (center of gravity), it does not have any controller for the pitch angle. Way point guidance in the pitch plane algorithm produces the surge command and the heave speed in order to reach the final point. These surge command and the heave speed are the input value of surge and heave speed controllers. In addition, actual surge and heave speed come from the output of the navigation solution. They are also input values of the controllers. When the vehicle enters a circle of the acceptance around the way point, the current way point P_i is accepted to have been reached. If the condition defined in Equation 5.5 is satisfied, the next way point is selected.

$$d_{pi} = \sqrt{(x_i - x)^2 + (z_i - z)^2} \leq \rho_0 \quad (5.5)$$

The desired points for the pitch plane way point guidance are given as:

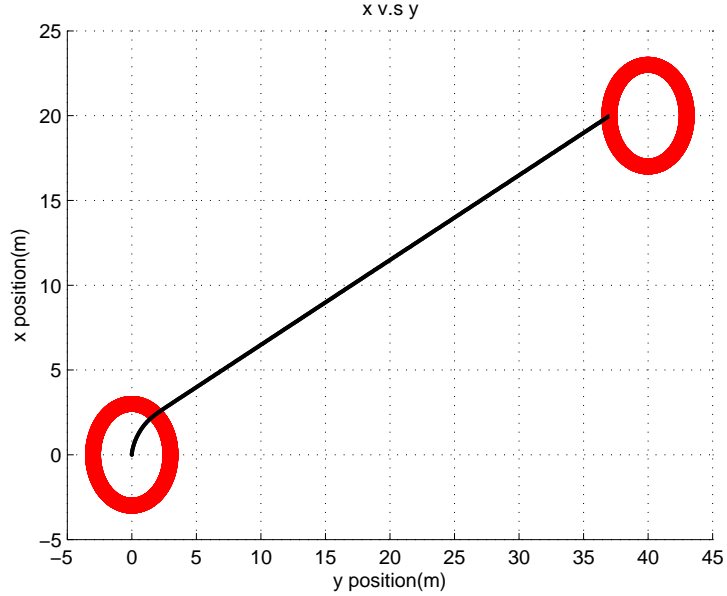


Figure 5.6: Way point guidance by LOS in the yaw plane for two reference points

$$\begin{aligned} x_i &= [0 \ 30 \ 50 \ 70 \ 90 \ 120 \ 140 \ 160 \ 180] \\ z_i &= [0 \ 10 \ 30 \ 50 \ 70 \ 95 \ 80 \ 60 \ 40] \end{aligned} \quad (5.6)$$

Figure 5.8 shows the simulation result for the way point guidance by LOS for the pitch plane motion. As seen in Fig. 5.8, vehicle reaches the desired points with the using navigational data.

5.2.3 Way Point Guidance in the 3D Motion

The schematic illustration of the 3D motion is shown in Fig. 5.9. While the vehicle moves, measured data data which comes from the sensors are estimated with the navigation system. The output of the navigation system are the estimated position of the vehicle in x, y and z axes. These estimated data and the desired position in x, y and z axes are the input of the guidance system. The way point guidance system produces the surge command and the heave speeds and the yaw angle commands. They are the input values of the controllers. Controllers produce force for the right and left thrusters (different value) and the vertical thrusters. They are inputs of the

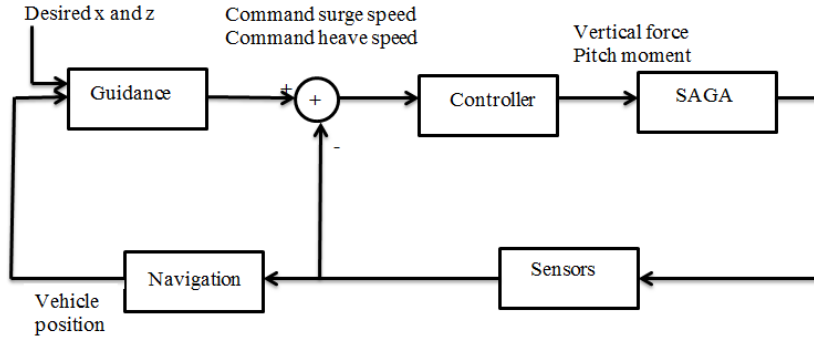


Figure 5.7: The schematic illustration of the combined system for the pitch plane motion

vehicle's model.

Way point guidance by LOS algorithm for 3D is a combination of the algorithm for yaw and pitch planes. Sphere of acceptance is used instead of circle of acceptance. When the vehicle enters a sphere of the acceptance around the way point, the current way point P_i is accepted to have been reached. If the condition is defined in Equation 5.7 is satisfied, the next way point is selected.

$$d_{pi} = \sqrt{(x_i - x)^2 + (y_i - y)^2 + (z_i - z)^2} \leq \rho_0 \quad (5.7)$$

The desired way points for 3D motion are given as

$$\begin{aligned} x_i &= [0 \quad 50 \quad 80 \quad 120 \quad 160 \quad 110] \\ y_i &= [0 \quad 40 \quad 70 \quad 90 \quad 120 \quad 80] \\ z_i &= [0 \quad 30 \quad 90 \quad 110 \quad 150 \quad 70] \end{aligned} \quad (5.8)$$

Figure 5.10 shows the simulation result for the way point guidance by LOS for the 3D motion. As seen in Fig. 5.10, vehicle reaches the desired points with the using the navigational data.

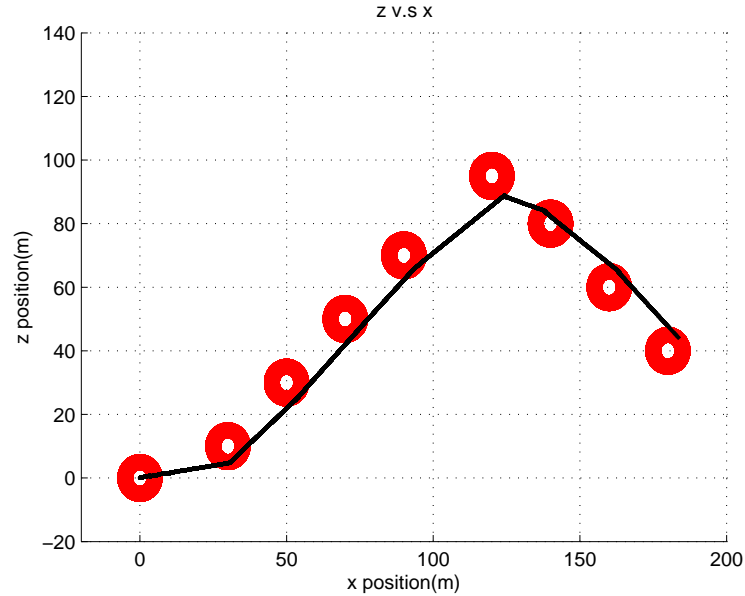


Figure 5.8: Way point guidance by LOS in the pitch plane

5.3 Optimal Guidance

An optimal autopilot-guidance algorithm is designed to perform 3D motion. The vehicle can reach the desired position by following many different tracking routes and with many different speeds. Different forces are produced from thrusters for each different route. The vehicle has limited energy either because of having a battery, or instantaneous power utilization is limited. It is aimed that the vehicle consumes energy economically while the design objectives are satisfied. The optimal autopilot(s) stands on a level between the guidance and the real autopilots. Depending on the guidance requirements a reference constructed by interpolation of the already calculated optimal inputs is generated for the real autopilots to drive the system (sub-optimally). In this way, the vehicle is supposed to reach the desired position and the yaw angle with desired velocity by consuming minimum energy [24].

The surge speed, heave speed and yaw angle of the vehicle are controlled by using PID controllers. The system input u , is generated from the outputs of these PID controllers. In the simulations, the input values of these controllers are differences between the actual system responses (from the mathematical model) and the reference

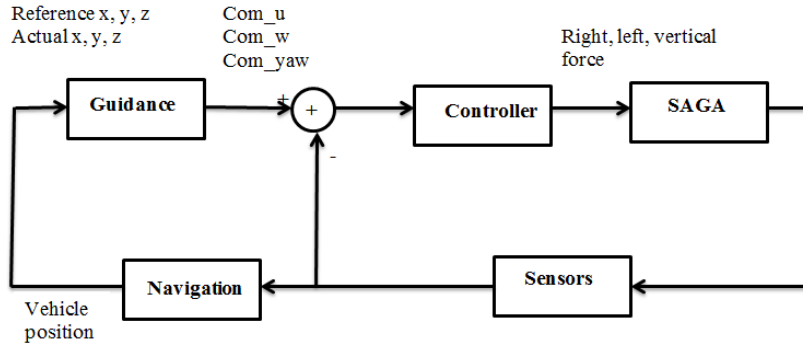


Figure 5.9: The schematic illustration of the combined system for the 3D motion

signals produced from a genetic algorithm. The consumed power for each thruster can be determined in terms of the produced forces from thrusters (u_i), (i.e., system inputs), as [38]:

$$P_i = \frac{2\pi\rho D_i^5 K_{Q_i}(J_0)}{\sqrt{\rho} D_i |K_{T_i}(J_0)|^{1.5}} |u_i|^{1.5} \quad (5.9)$$

where D is diameter of propeller, K_Q is torque coefficient, K_T is thruster coefficient and J_0 is advanced ratio.

An approximation to the power formula is given and the detailed formulation was given in [38]:

$$P_i = \alpha_i |u_i|^{1.5} \quad (5.10)$$

The constant α_i is the weighting factor which may be different for each thruster.

An optimal control problem is defined in such a way that vehicle arrives the desired position and rotation with desired initial and final velocities by consuming minimum energy. Optimal paths to move with minimum energy expenditure are constructed and these results are inserted in a database. This database is later to be used to generate optimal (probably quasi-optimal) guidance comments to guide the vehicle with minimum energy expenditure. In real time, the guidance algorithm is supposed to interpolate the stored information in the database (positions are separated as near, middle

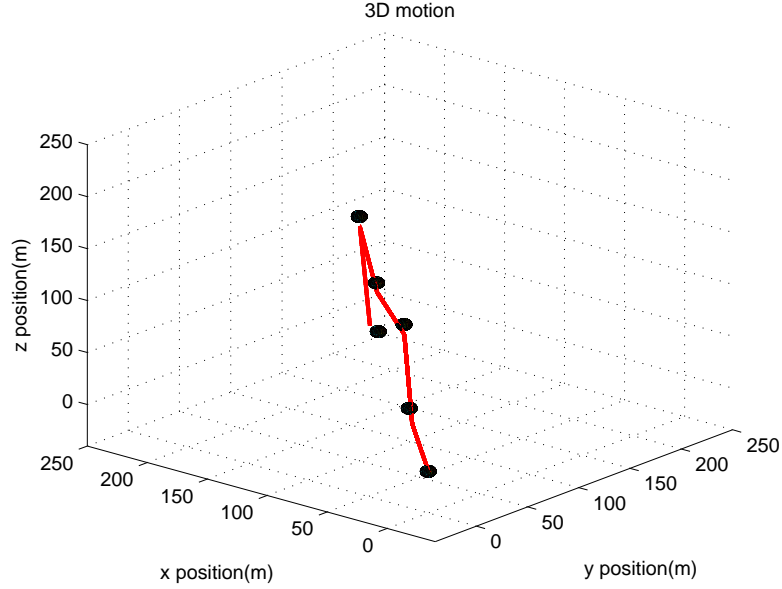


Figure 5.10: Way point guidance by LOS in the 3D motion

and far distances, rotations are stored as big, small, middle-big and small-middle yaw angles). This database will be used under the waypoint guidance algorithm. In this study, database is not completed, some optimal paths are generated only for certain motions. In this way, optimal paths are generated for different distances and different attitudes [24].

The optimal control problem with initial and final state constraints is formulated by using Eqn. 5.11 as the main part of the cost function. In this study, a genetic algorithm is used to produce the reference values of the surge speed, heave speed and yaw angle (u, w, φ) in a time interval [26].

$$\min J_0 = \frac{1}{2}(\Delta\bar{x}(t_f))^T S \Delta\bar{x}(t_f) + k \int_{t_0}^{t_f} \sum_{i=1}^3 |u_i|^{1.5} dt \quad (5.11)$$

subject to

$$\begin{aligned}
0 &\leq u \leq 1.5 \text{ m/s} \\
-\pi &\leq \varphi \leq \pi \text{ rad} \\
0 &\leq w \leq 0.5 \text{ m/s}
\end{aligned} \tag{5.12}$$

The initial and boundary conditions are specified as:

$$\bar{x}_{(t_0)} = \begin{bmatrix} x_0 \\ y_0 \\ z_0 \\ u_0 \\ w_0 \\ \psi_0 \end{bmatrix}, \bar{x}_f = \begin{bmatrix} x_f \\ y_f \\ z_f \\ u_f \\ w_f \\ \psi_f \end{bmatrix} \tag{5.13}$$

$$\Delta \bar{x}(t_f) = \bar{x}(t_f) - \bar{x}(f) \tag{5.14}$$

$$|u_i| \sim |T_i| \tag{5.15}$$

where,

t_0 : Initial time,

t_f : Final time,

$\Delta \bar{x}(t_f)$: Difference between desired final state and actual final state,

$\bar{x}(f)$: The final value of vector,

$\bar{x}(t_f)$: The value of vector at reaching final time,

$S > 0$ is a diagonal weighting matrix and $k > 0$ scalar weighting factor.

Since time consumption is not critical, fixed final step is used. This leads to a Two Point Boundary Value Problem, (TPBVP). In order to generate the trajectory with consuming min. energy, the surge, heave speed and yaw angle, u , w , φ , are adjusted at each time interval. Optimal solution for OCP in Equation 5.11 is obtained

by changing states at each time interval. Because of this, traveling time is divided into n equal intervals and reference values, u , w , φ , for each time interval are generated. Hence, total number of variables of OCP in Equation 5.11 is equal to $3n$. The illustration of the optimal solution for OCP is shown in Fig. 5.11.

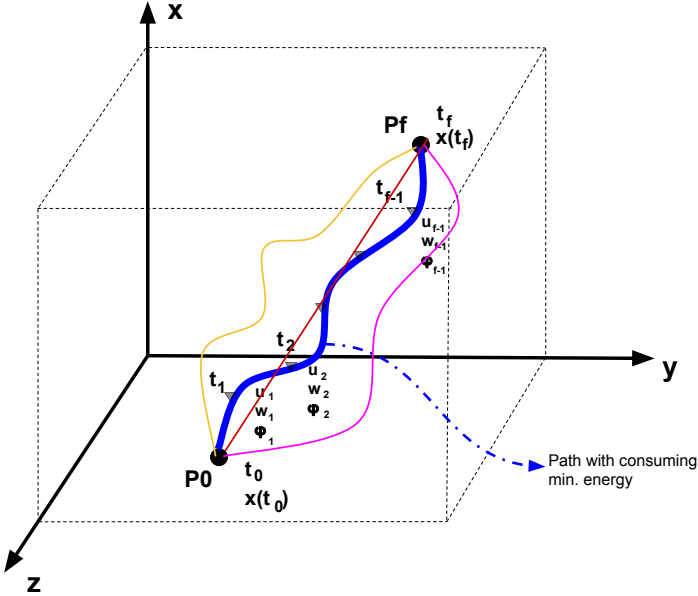


Figure 5.11: Path possibilities and the illustration of the optimal solution for OCP

Since the optimal control problem in Equation 5.11 is a constrained one, it is solved by using constrained non-linear optimization techniques. There are many iterative methods for solving the nonlinear optimal control problems such as neighboring externals methods, quasilinear methods and gradient methods [10] and [27].

5.3.1 Constrained Nonlinear Optimization

In this study, the constrained nonlinear optimal control problem defined in Eq. 5.11 is solved using a genetic algorithm. Genetic algorithms based on natural selection process are used both for solving constrained and unconstrained optimization problems. This process is explained as:

1. Selection of the initial population randomly.
2. Fitness evaluation.

3. If the stopping criterias are satisfied, algorithm stops and the results is the optimal solution.
4. If the stopping criteria are not satisfied, a new population is generated.
5. To generate the new population, elite individuals after crossover and mutation operations are chosen. Hence, the new population is formed by the gathering of high-fit individuals from the previous population.
6. The fitness is evaluated for each member of the new population. This procedure continues until the criteria in step 3 are satisfied.

5.3.2 Simulation Results for Optimal Guidance

In the simulation study, the system is composed of the nonlinear model of the vehicle and the PID controllers. The initial and boundary conditions for the simulations are given as:

$$\begin{bmatrix} x_f \\ y_f \\ z_f \\ \psi_f \end{bmatrix} = \begin{bmatrix} 40 \text{ m} \\ 20 \text{ m} \\ 10 \text{ m} \\ \pi/6 \end{bmatrix} \quad (5.16)$$

$$\begin{bmatrix} x_0 \\ y_0 \\ z_0 \\ \psi_0 \end{bmatrix} = \begin{bmatrix} 0 \\ 0 \\ 0 \\ 0 \end{bmatrix} \quad (5.17)$$

$$u_{f(i)} = u_{0(i)} = \begin{bmatrix} 0.5 & 1 & 1.5 \end{bmatrix} \quad (5.18)$$

$$w_{f(i)} = w_{0(i)} = \begin{bmatrix} 0.1 & 0.3 & 0.5 \end{bmatrix} \quad (5.19)$$

Many simulations have been performed to cover the velocity range and distance between initial and final points. In the continuation of this study, to simplify the com-

putational complexity, distance and velocity ranges will be divided into three basic values each as “very close”, “medium range”, “far”, “low speed”, “medium speed” and “fast”. Of course, there are parameters to be chosen to give meanings to these linguistic variables. In this way, the path which has a minimum performance index can be obtained for different initial and different final velocities by interpolating. MATLAB, optimization toolbox is used to obtain the solutions of optimal control problems by using a genetic algorithm.

Figure 5.12 shows three different paths that the vehicle follows by consuming minimum energy with different heave speeds starting at the initial surge velocity $0.5m/s$. As seen from the figure that the consumed energy is the least when $u_0 = 0.5$ and $w_0 = 0.1$. Figures 5.13, 5.14 and 5.15 show the tracked path for $u_0 = 0.5m/s$ with different heave velocities in X-Y, X-Z and Y-Z respectively.

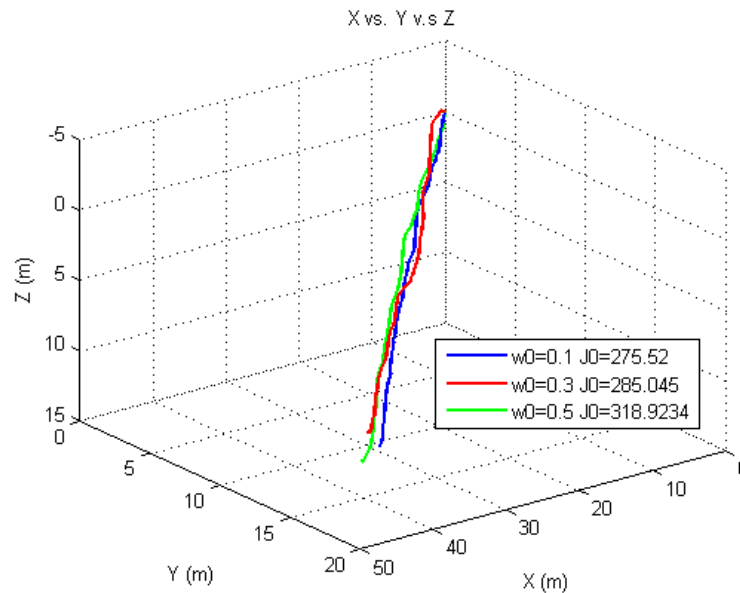


Figure 5.12: The tracked path for $u_0 = 0.5m/s$ with a different heave velocity, w_0

Figure 5.16 shows three different paths that the vehicle follows by consuming minimum energy with different heave speeds starting at the initial surge velocity $1m/s$. As seen from the figure that the consumed energy is the least when $u_0 = 1$ and $w_0 = 0.1$.

Fig. 5.17 shows three different paths that the vehicle follows by consuming minimum energy with different heave speeds starting at the initial surge velocity $1.5m/s$. As seen from the figure that the consumed energy is the least when $u_0 = 1.5$ and

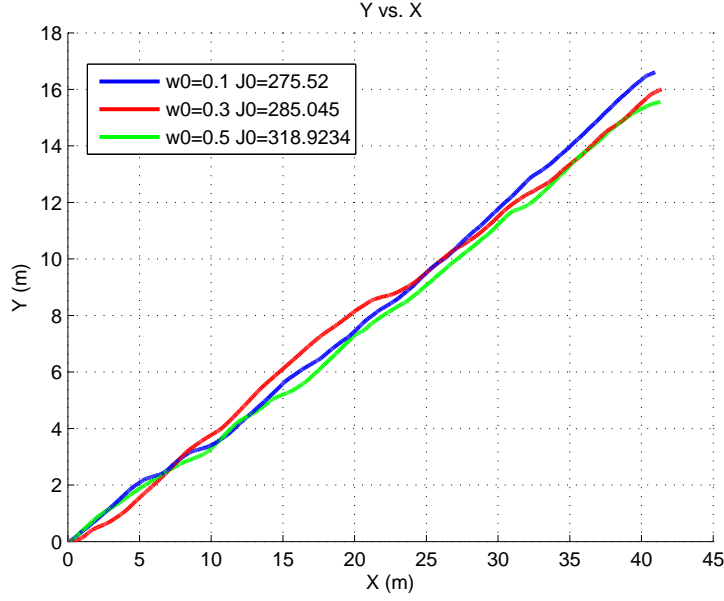


Figure 5.13: The tracked path for $u_0 = 0.5m/s$ in the x-y view

$w_0 = 0.1$.

For the other case, initial and boundary conditions for the simulations are given as:

$$\begin{bmatrix} x_f \\ y_f \\ z_f \\ \psi_f \end{bmatrix} = \begin{bmatrix} 50 \text{ m} \\ 25 \text{ m} \\ 15 \text{ m} \\ \pi/3 \end{bmatrix} \quad (5.20)$$

$$\begin{bmatrix} x_0 \\ y_0 \\ z_0 \\ \psi_0 \end{bmatrix} = \begin{bmatrix} 0 \\ 0 \\ 0 \\ 0 \end{bmatrix} \quad (5.21)$$

Figure 5.18 shows three different paths that the vehicle follows by consuming minimum energy with different heave speeds starting at the initial surge velocity $0.5m/s$. As seen from the figure that the consumed energy is the least when $u_0 = 0.5$ and $w_0 = 0.3$.

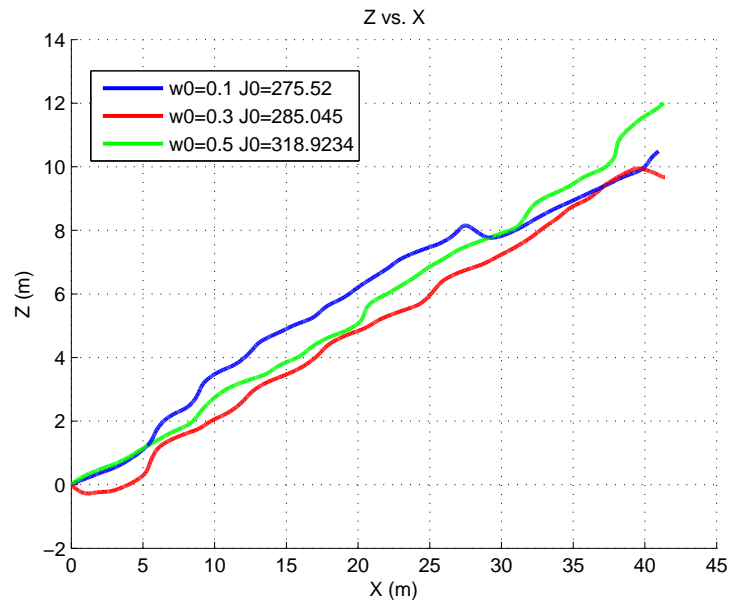


Figure 5.14: The tracked path for $u_0 = 0.5m/s$ in the x-z view

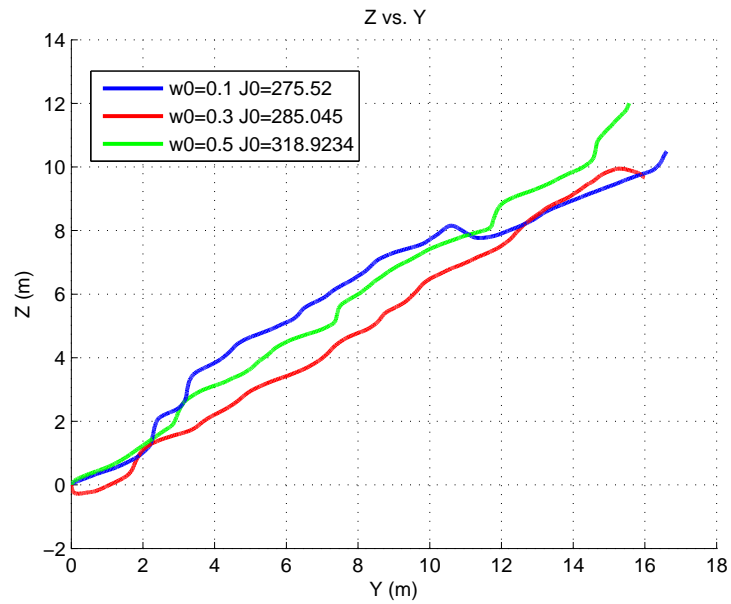


Figure 5.15: The tracked path for $u_0 = 0.5m/s$ in the y-z view

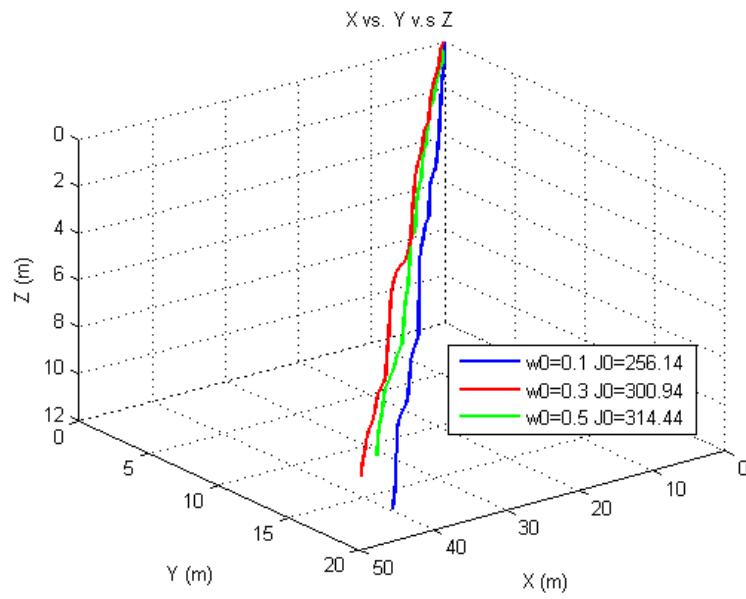


Figure 5.16: The tracked path for $u_0 = 1\text{m/s}$ with a different heave velocity, w_0

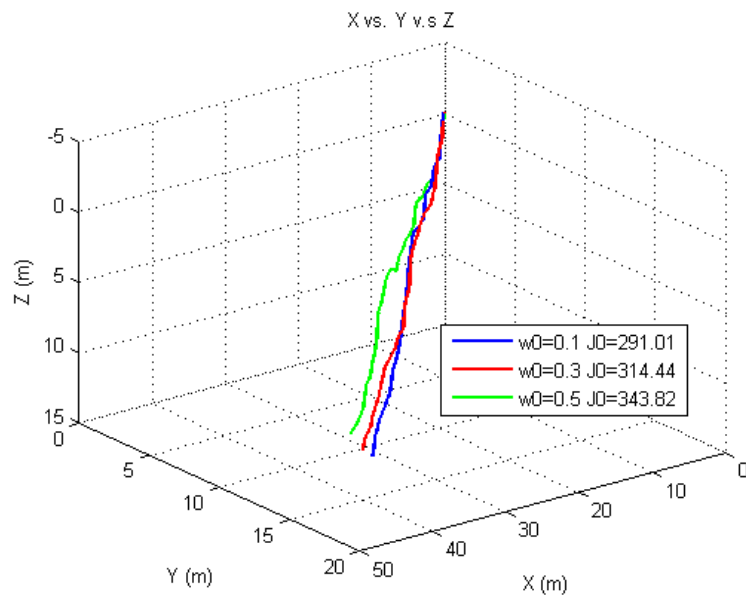


Figure 5.17: The tracked path for $u_0 = 1.5\text{m/s}$ with a different heave velocity, w_0

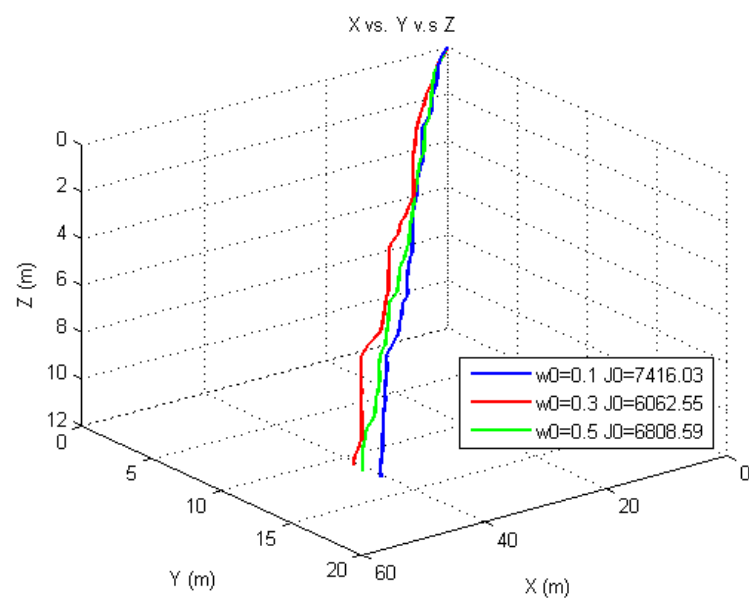


Figure 5.18: The tracked path for $u_0 = 0.5m/s$ with a different heave velocity, w_0

CHAPTER 6

EXPERIMENTS

6.1 Introduction

The navigation data of the vehicle is required for the system identification study. Navigation data should be obtained from real experiments instead of generating it from vehicle's model response. In this chapter, the acoustic-based navigation experiment in the pool of the Middle East Technical University (METU) shown in Fig. 6.1 is designed to obtain the vehicle's position. Since the measured data is noisy, it is improved by a Kalman filter algorithm. Before filtering, the system and measurement model are defined for indirect Kalman filter algorithm. This estimated position and attitude data will be used for the system identification study. The details of the acoustic-based measurement system will be presented in this chapter.



Figure 6.1: Navigation experiment of the SAGA in the pool of METU

6.2 Acoustic-based Navigation Experiment of SAGA

Acoustic-based measurement system is composed of pinger, hydrophones and a data card. The pinger used in the experiments is shown in Fig. 6.2. Its frequency is adjustable around 20-50 kHz. In this experiment, pinger sends signals with 20 kHz at each second.



Figure 6.2: Pinger used in the experiment

Fig. 6.3 shows the hydrophone used in this experiment. Four hydrophones are necessary in order to obtain position of the vehicle. For more accurate results, eight hydrophones can also be used in the experiment.

Data card used in the experiment is shown in Fig. 6.4. It has many input and output ports. The cable of each hydrophone is connected to an output port of the data card. The signals can be collected at 100 kHz synchronously in this experiment using this data card.

Fig. 6.5 shows the experimental setup. Each hydrophone is located at a known position in the pool. Pinger is located on the SAGA. While the vehicle moves in the pool, each hydrophone receives the acoustic signal sent from the pinger. The distance between the vehicle and the each hydrophone is obtained from the speed of the acoustic signal and the TOD of signals.

The distance between each hydrophone and the vehicle is obtained as:

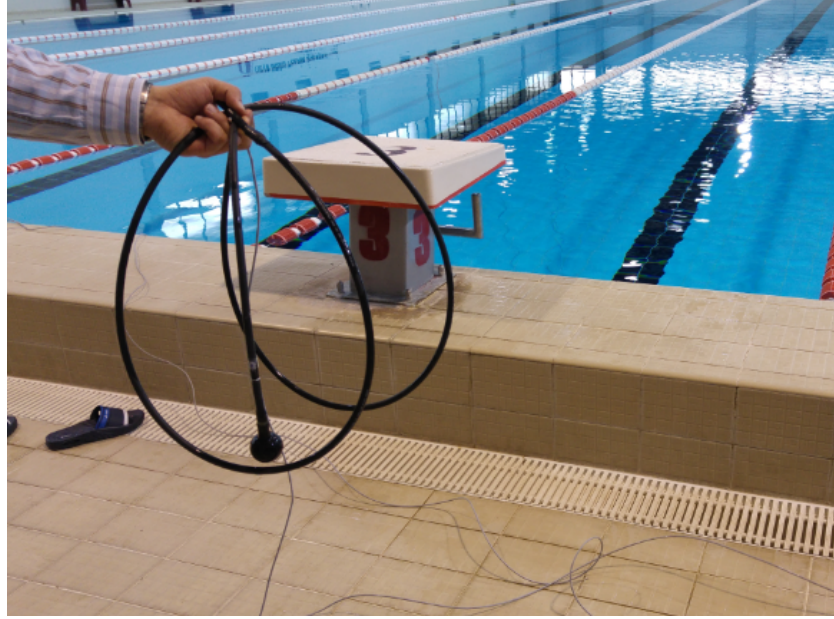


Figure 6.3: Hydrophone used in the experiment

$$d_i = c(t_i - t_p) = \sqrt{(x - x_i)^2 + (y - y_i)^2 + (z - z_i)^2} \quad (6.1)$$

i : The index of each hydrophone,

$P_{vehicle} = (x, y, z)$: The unknown position of the vehicle,

$P_i = (x_i, y_i, z_i)$: The position of the i th hydrophone,

d_i : The distance between the vehicle and i th hydrophone,

c : The speed of the acoustic signal in the water,

t_p : The sending time of the acoustic signal from pinger,

t_i : The receiving time of the received signal from i th hydrophone.

$P_1 = (x_1, y_1, z_1)$: The position of the first hydrophone,

$P_1 = (2, 3.18, 0.4)$

$P_2 = (x_2, y_2, z_2)$: The position of the second hydrophone,

$P_2 = (3, 5.72, 0.4)$

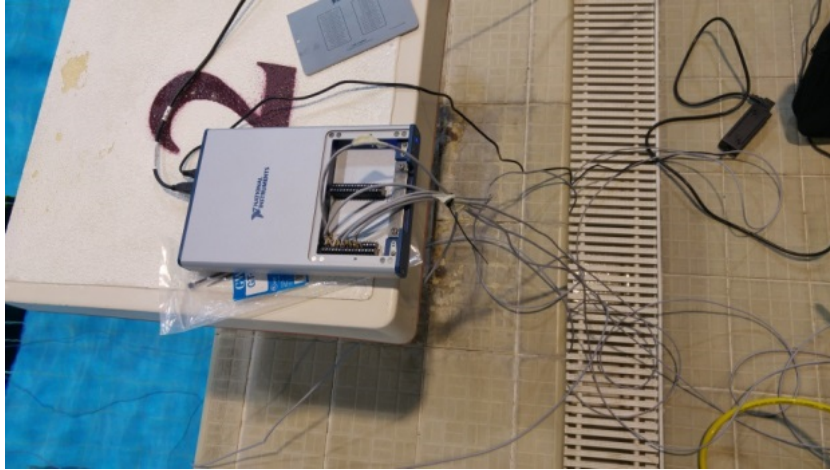


Figure 6.4: Data card used in the experiment

$P_3 = (x_3, y_3, z_3)$: The position of the third hydrophone,

$$P_3 = (6, 5.72, 0.4)$$

$P_4 = (x_4, y_4, z_4)$: The position of the fourth hydrophone,

$$P_4 = (2, 8.26, 0.4)$$

$P_5 = (x_5, y_5, z_5)$: The position of the fifth hydrophone,

$$P_5 = (6, 8.26, 0.4)$$

$P_6 = (x_6, y_6, z_6)$: The position of the sixth hydrophone,

$$P_6 = (6, 3.18, 0.4)$$

$P_7 = (x_7, y_7, z_7)$: The position of the seventh hydrophone,

$$P_7 = (4, 8.26, 0.4)$$

$P_8 = (x_8, y_8, z_8)$: The position of the eight hydrophone,

$$P_8 = (4, 3.18, 0.4)$$

Distance between the vehicle and each hydrophone is obtained as:

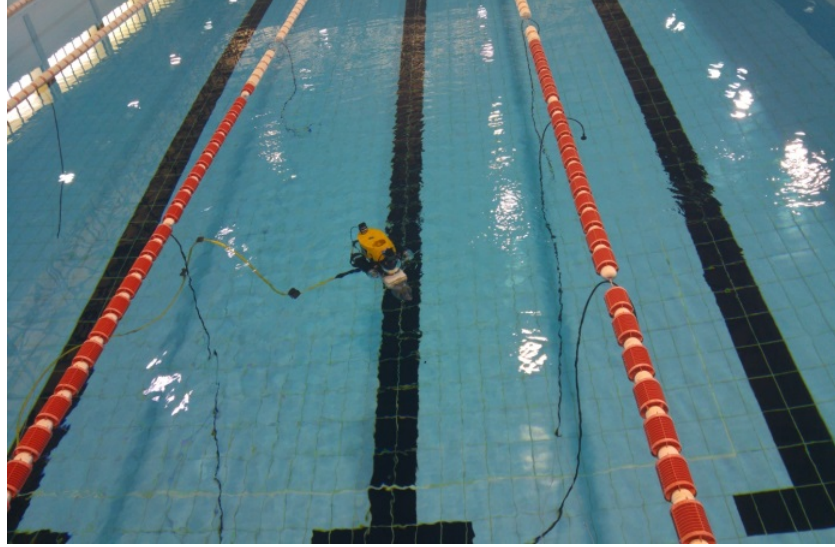


Figure 6.5: Pool experiment set-up composed of pinger and hydrophones

$$\begin{aligned}
 d_1 &= c(t_1 - t_p) = \sqrt{(x - x_1)^2 + (y - y_1)^2 + (z - z_1)^2} \\
 d_2 &= c(t_2 - t_p) = \sqrt{(x - x_2)^2 + (y - y_2)^2 + (z - z_2)^2} \\
 d_3 &= c(t_3 - t_p) = \sqrt{(x - x_3)^2 + (y - y_3)^2 + (z - z_3)^2} \\
 d_4 &= c(t_4 - t_p) = \sqrt{(x - x_4)^2 + (y - y_4)^2 + (z - z_4)^2} \\
 d_5 &= c(t_5 - t_p) = \sqrt{(x - x_5)^2 + (y - y_5)^2 + (z - z_5)^2} \\
 d_6 &= c(t_6 - t_p) = \sqrt{(x - x_6)^2 + (y - y_6)^2 + (z - z_6)^2} \\
 d_7 &= c(t_7 - t_p) = \sqrt{(x - x_7)^2 + (y - y_7)^2 + (z - z_7)^2} \\
 d_8 &= c(t_8 - t_p) = \sqrt{(x - x_8)^2 + (y - y_8)^2 + (z - z_8)^2}
 \end{aligned}
 \tag{6.2}$$

The function f_i is obtained from Eqn. 6.1 for each hydrophone.

$$f_i(x, y, z, t_p) = \sqrt{(x - x_i)^2 + (y - y_i)^2 + (z - z_i)^2} - c(t_i - t_p) \tag{6.3}$$

$$\begin{aligned}
f_1(x, y, z, t_p) &= \sqrt{(x - x_1)^2 + (y - y_1)^2 + (z - z_1)^2} - c(t_1 - t_p) \\
f_2(x, y, z, t_p) &= \sqrt{(x - x_2)^2 + (y - y_2)^2 + (z - z_2)^2} - c(t_2 - t_p) \\
f_3(x, y, z, t_p) &= \sqrt{(x - x_3)^2 + (y - y_3)^2 + (z - z_3)^2} - c(t_3 - t_p) \\
f_4(x, y, z, t_p) &= \sqrt{(x - x_4)^2 + (y - y_4)^2 + (z - z_4)^2} - c(t_4 - t_p) \\
f_5(x, y, z, t_p) &= \sqrt{(x - x_5)^2 + (y - y_5)^2 + (z - z_5)^2} - c(t_5 - t_p) \\
f_6(x, y, z, t_p) &= \sqrt{(x - x_6)^2 + (y - y_6)^2 + (z - z_6)^2} - c(t_6 - t_p) \\
f_7(x, y, z, t_p) &= \sqrt{(x - x_7)^2 + (y - y_7)^2 + (z - z_7)^2} - c(t_7 - t_p) \\
f_8(x, y, z, t_p) &= \sqrt{(x - x_8)^2 + (y - y_8)^2 + (z - z_8)^2} - c(t_8 - t_p)
\end{aligned}
\tag{6.4}$$

The unknown position of the vehicle and the sending time of the acoustic signal from the pinger are found using optimization with the fmincon algorithm in MATLAB environment. As seen from Eqn. 6.3, the receiving time of signal for each hydrophone, t_i is needed to obtain the position of the vehicle. The receiving signal of the first, second...eight hydrophone is shown in Figures from Fig. 6.6 up to Fig. 6.13.

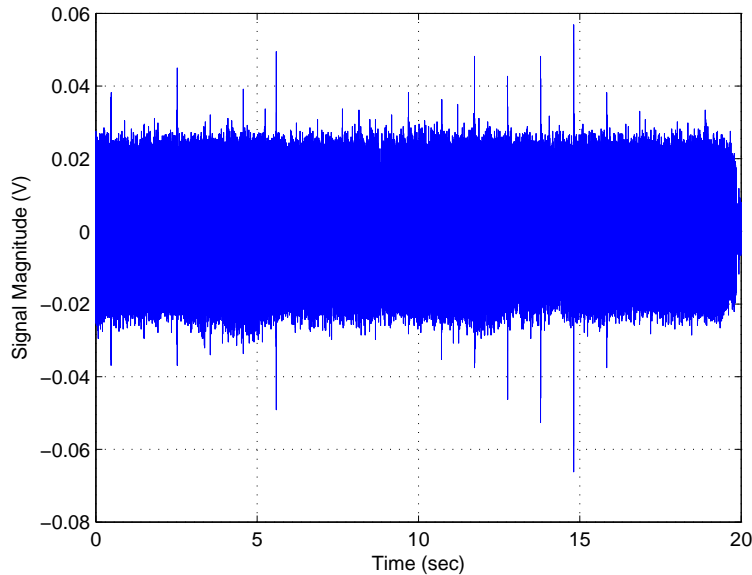


Figure 6.6: Received signal from the 1st hydrophone with respect to time

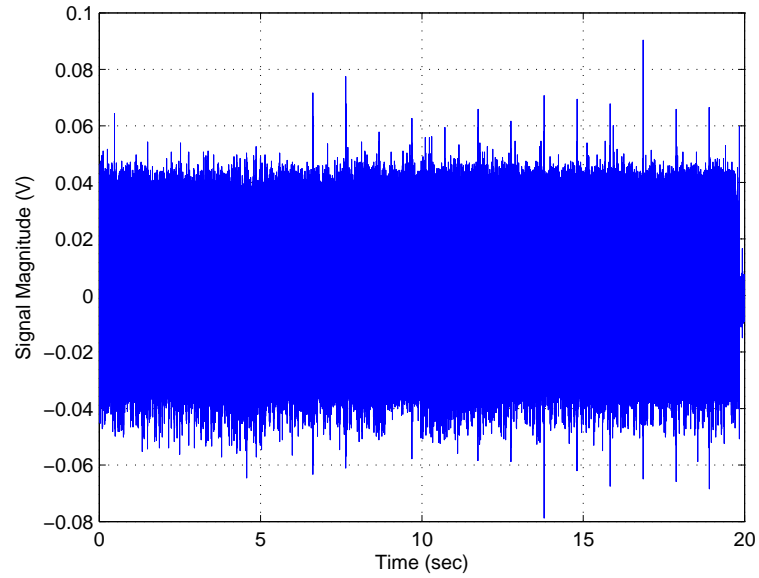


Figure 6.7: Received signal from the 2nd hydrophone with respect to time

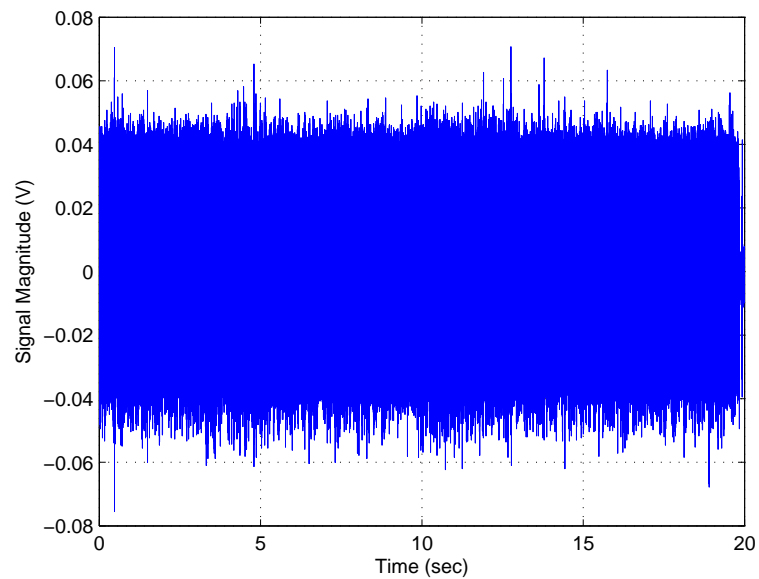


Figure 6.8: Received signal from the 3rd hydrophone with respect to time

Since the pinger sends the acoustic signal at 20 kHz, each receiving signal is filtered around 20 kHz using a bandpass filter (using 'fir1' command of Matlab). Then, the peak times are detected from each filtered signal in order to determine the receiving time, t_i for each hydrophone. The peak times are detected using 'findpeaks' command

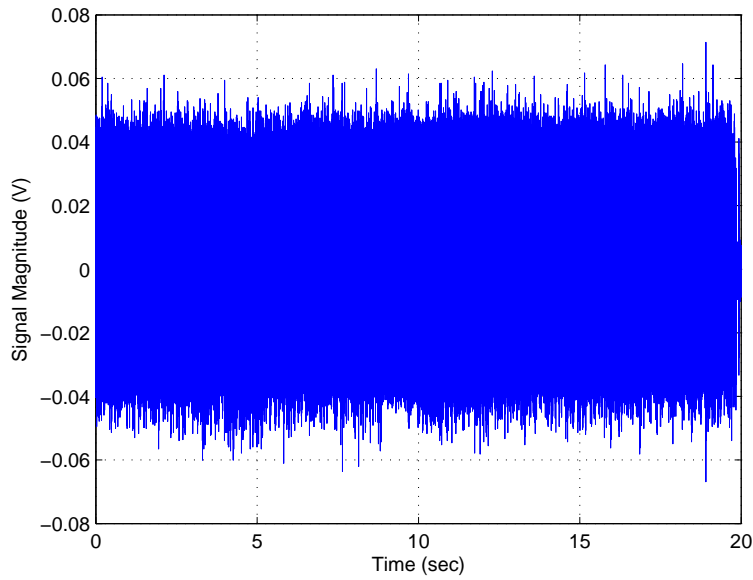


Figure 6.9: Received signal from the 4th hydrophone with respect to time

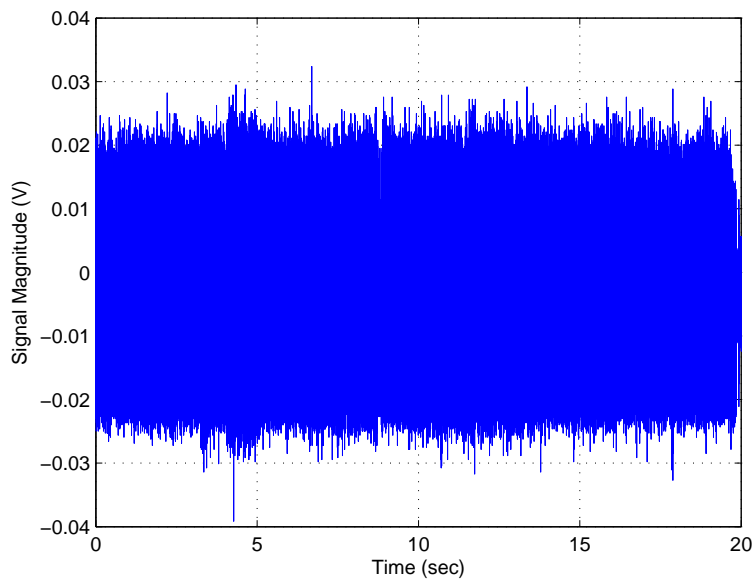


Figure 6.10: Received signal from the 5th hydrophone with respect to time

of Matlab. This filtered and peak times of the first, second...eight received signals are shown in figures from Fig.6.14 to Fig 6.21.

Peaks times of all received signals are shown in tables 6.1 and 6.2. $t_1, t_2, t_3, t_4, t_5,$

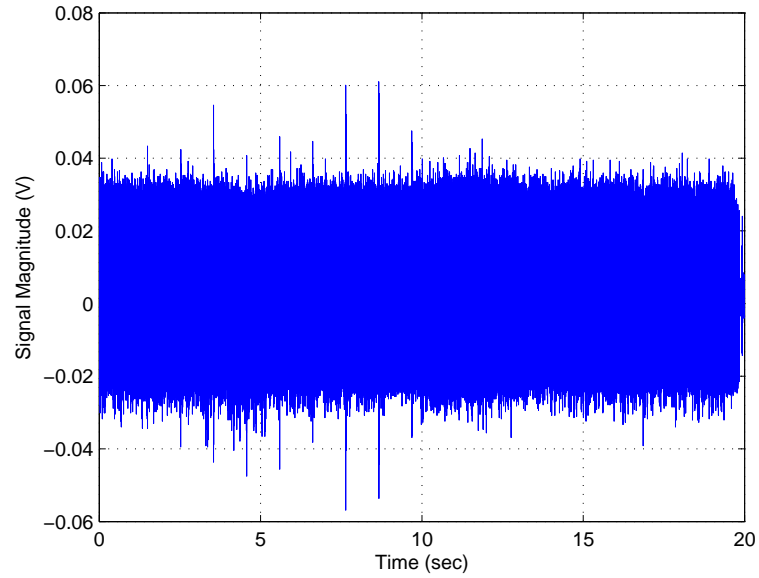


Figure 6.11: Received signal from the 6th hydrophone with respect to time

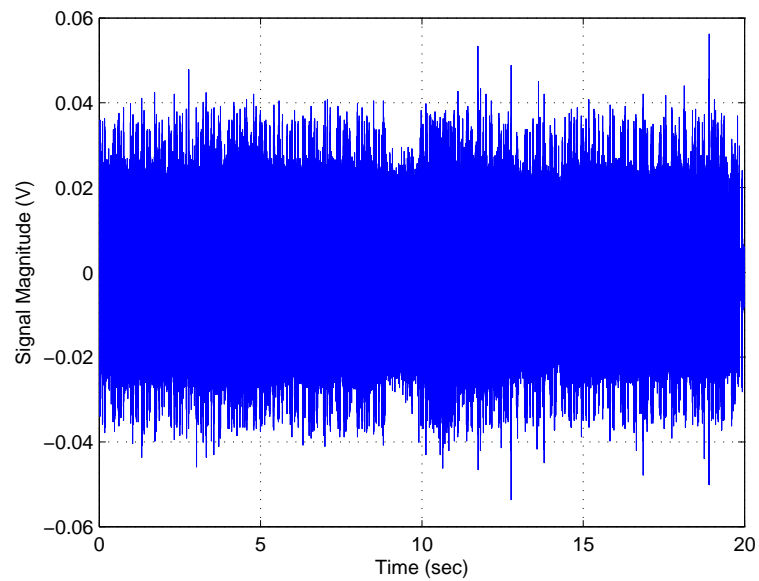


Figure 6.12: Received signal from the 7th hydrophone with respect to time

t_6, t_7, t_8 are the peak times of the received signals from 1th, 2nd, 3rd, 4th, 5th, 6th, 7th, 8th hydrophones, respectively.

After the detection of peak times of the each receiving signals, the position of the

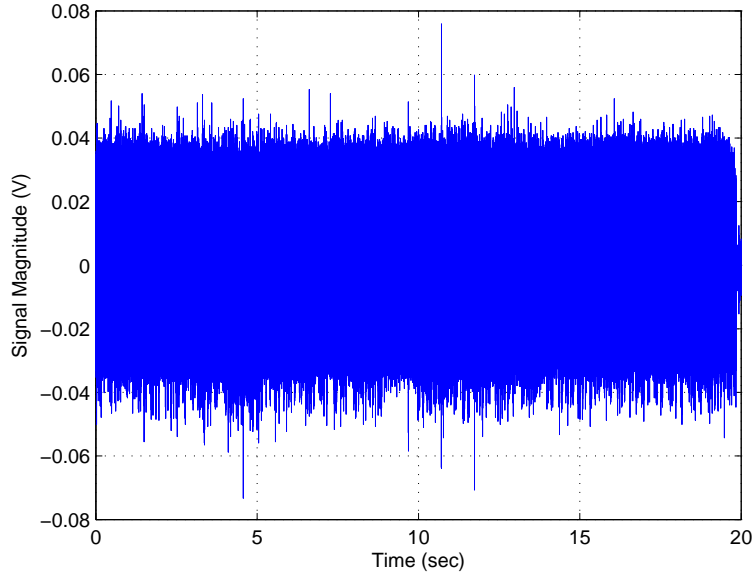


Figure 6.13: Received signal from the 8th hydrophone with respect to time

vehicle in the acoustic-based measurement system is obtained using optimization with `fmincon` algorithm solving the optimization problem with the objective function J given below:

$$\begin{aligned} \text{Minimize } J &= \sum_{i=1}^n [d1_i - d2_i]^2 \\ &\text{subject to} \\ &0 \leq x \leq 6 \\ &0 \leq y \leq 9 \\ &0 \leq z \leq 2 \end{aligned} \quad (6.5)$$

where

$$d1_i = c(t_i - t_p) \quad (6.6)$$

$$d2_i = \sqrt{(x - x_i)^2 + (y - y_i)^2 + (z - z_i)^2} \quad (6.7)$$

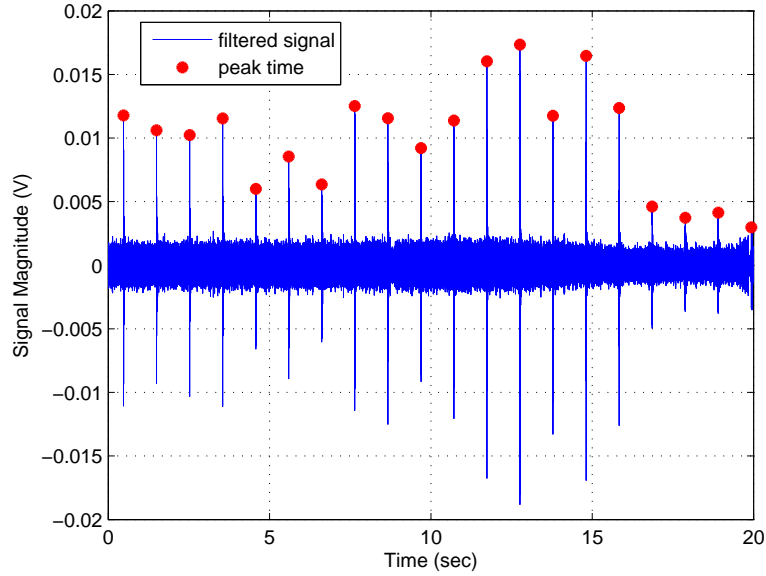


Figure 6.14: Filtered signal of received signal from the 1st hydrophone with respect to time and the peak times of this filtered signal

The obtained positions of the vehicle during the experiment in x axes and y axes are shown in figures 6.22 and 6.23.

6.2.1 Inertial Measurement System and Aiding Sensor

Inertial measurement system used in the experiment is UM7 as shown in Fig. 6.24. UM7 is a 3rd-generation attitude and heading reference system (AHRS). The UM7 combines triaxial accelerometer, rate gyro, and magnetometer data using a sophisticated Extended Kalman Filter to produce attitude and heading estimates and measures acceleration in the x,y and z-axes.

In this experiment, the attitude data, roll, pitch and yaw angles and the acceleration in x, y and z-axes are measured from UM7. The measured roll, pitch and yaw angles and the fitted polynomial of degree 4 are shown in figures 6.25, 6.26 and 6.27, respectively. The angular velocity can be obtained by taking the derivative of the measured attitude data. For this purpose, the measured attitude data is interpolated first.

The measured accelerations in x, y and z-axes come from IMU, UM7, are shown

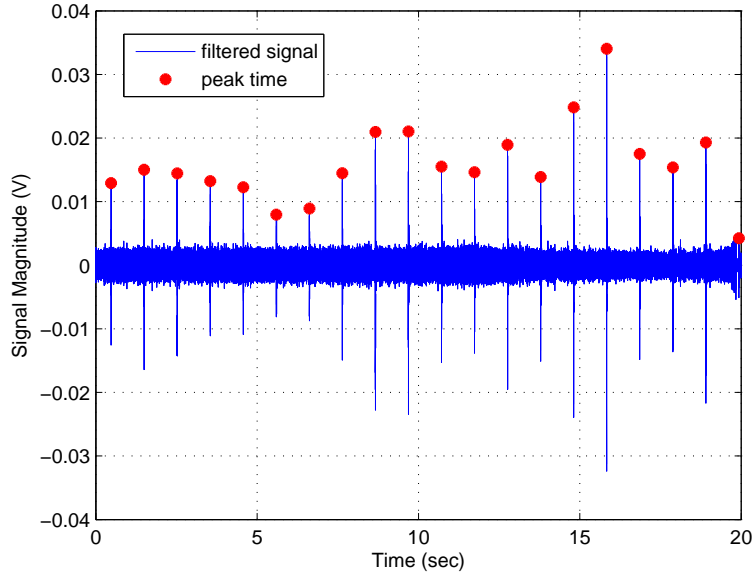


Figure 6.15: Filtered signal of received signal from the 2nd hydrophone with respect to time and the peak times of this filtered signal

in Fig.6.28. in the body frame. Translational velocities, surge, sway and heave, are obtained by integrating the measured accelerations. The translational positions are obtained by integrating the translational velocities and they are transformed to the earth frame. The obtained translational positions in x, y and z-axes are shown in Fig. 6.29.

Using the acoustic-based measurement system, depth sensor and IMU compose the integrated navigation system. Since all measured data have noisy, they are estimated with a Kalman filter. Firstly, system and states are defined, then measurement model is constructed for this experimentally integrated navigation system.

6.2.2 System Model and State Selection for Acoustic-based Navigation Experiment of SAGA

States are chosen as the rotational position (attitude), translational velocity, translational position errors and the biases of the accelerometer and gyroscope with respect to earth frame for the integrated navigation experiment. It is defined as the following vector:

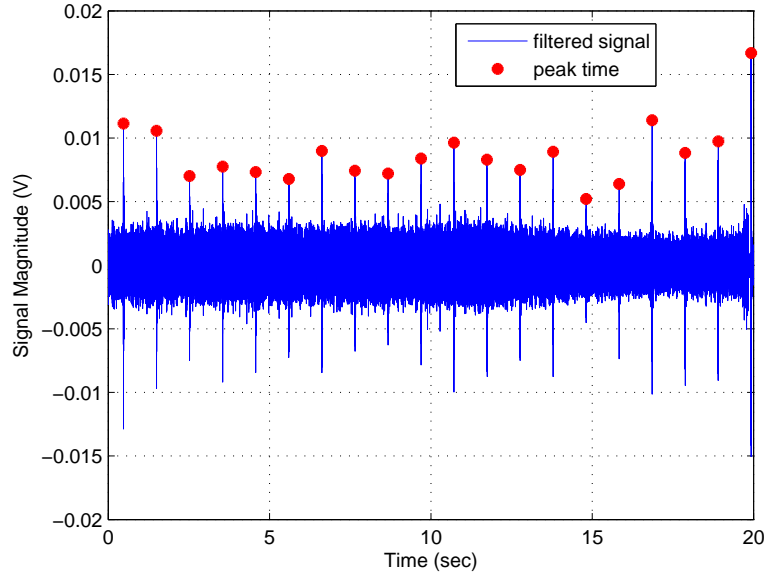


Figure 6.16: Filtered signal of received signal from the 3rd hydrophone with respect to time and the peak times of this filtered signal

$$x = \begin{pmatrix} \delta\varphi_{eb}^e \\ \delta v_{eb}^e \\ \delta r_{eb}^e \\ b_a \\ b_g \end{pmatrix} \quad (6.8)$$

The state propagation in an Earth frame was obtained in Chapter 4.

The rate of change of the attitude error is [20]

$$\delta\dot{\varphi}_{eb}^e \approx \hat{C}_b^e b_g - \Omega_{ie}^e \delta\varphi_{eb}^e \quad (6.9)$$

The rate of change of the velocity error is [20]

$$\delta\dot{v}_{eb}^e \approx - \left(\hat{C}_b^e \hat{f}_{ib}^b \right) \wedge \delta\varphi_{eb}^e - 2\Omega_{ie}^e \delta v_{eb}^e + \hat{C}_b^e b_a \quad (6.10)$$

The rate of change of the position error is [20]

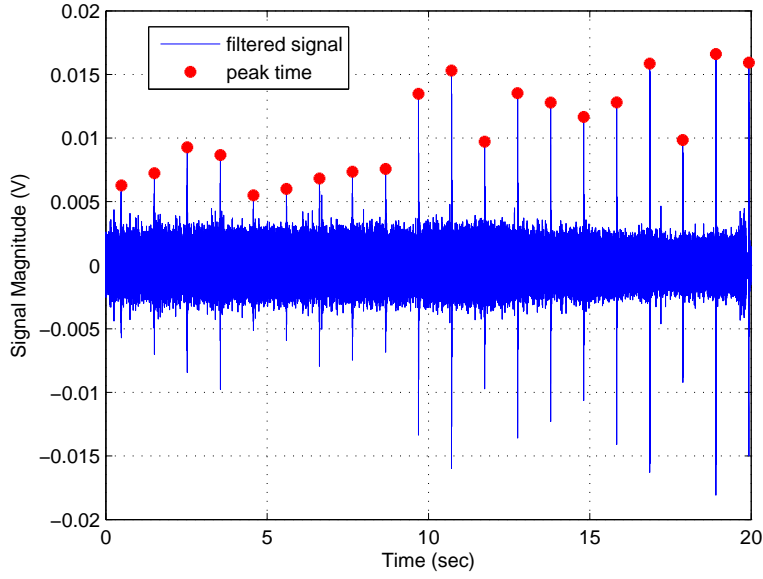


Figure 6.17: Filtered signal of received signal from the 4th hydrophone with respect to time and the peak times of this filtered signal

$$\delta \dot{r}_{eb}^e = \delta v_{eb}^e \quad (6.11)$$

The rate of accelerometer and gyro biases are assumed to be zero as [20]:

$$\dot{b}_a = 0 \quad \dot{b}_g = 0 \quad (6.12)$$

The state space representation of the system is:

$$\dot{x} = Fx + Qw \quad (6.13)$$

The system matrix, F is obtained from Equations 6.9, 6.10, 6.11 and 6.12 as [20]:

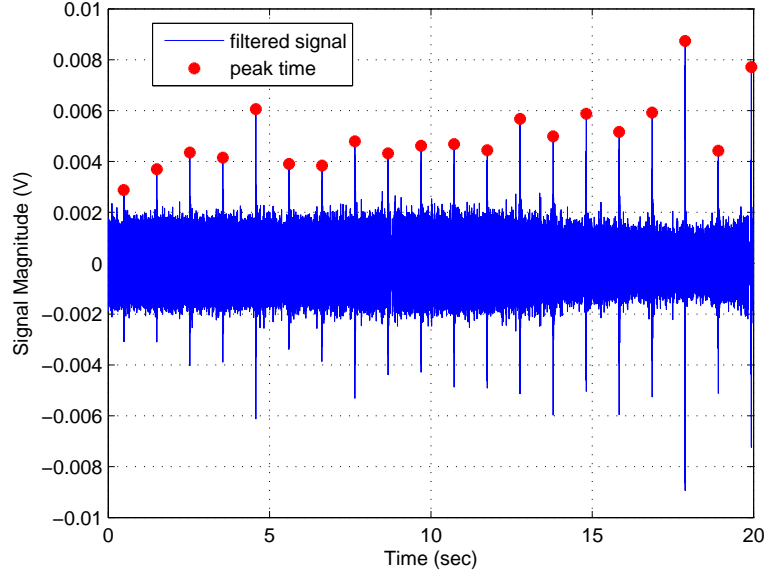


Figure 6.18: Filtered signal of received signal from the 5th hydrophone with respect to time and the peak times of this filtered signal

$$F = \begin{bmatrix} -\Omega_{ie}^e & 0_3 & 0_3 & 0_3 & \hat{C}_b^e \\ [-\hat{C}_b^e \hat{f}_{ib}^b \wedge] & -2\Omega_{ie}^e & 0_3 & \hat{C}_b^e & 0_3 \\ 0_3 & I_3 & 0_3 & 0_3 & 0_3 \\ 0_3 & 0_3 & 0_3 & 0_3 & 0_3 \\ 0_3 & 0_3 & 0_3 & 0_3 & 0_3 \end{bmatrix} \quad (6.14)$$

The data from the inertial sensor, depth sensor and acoustic measurement system comes in discrete time. Hence, the equivalent representation of the state-space representation in discrete time is used. The discrete time representation is defined as

$$x_{k+1} = \Phi_k x_k + w_k \quad (6.15)$$

The state transition matrix, Φ_k is obtained from the system dynamics matrix F and time range $\Delta t = t_{k+1} - t_k$ [16].

$$\Phi_k = e^{F\Delta t} = I + F\Delta t \quad (6.16)$$

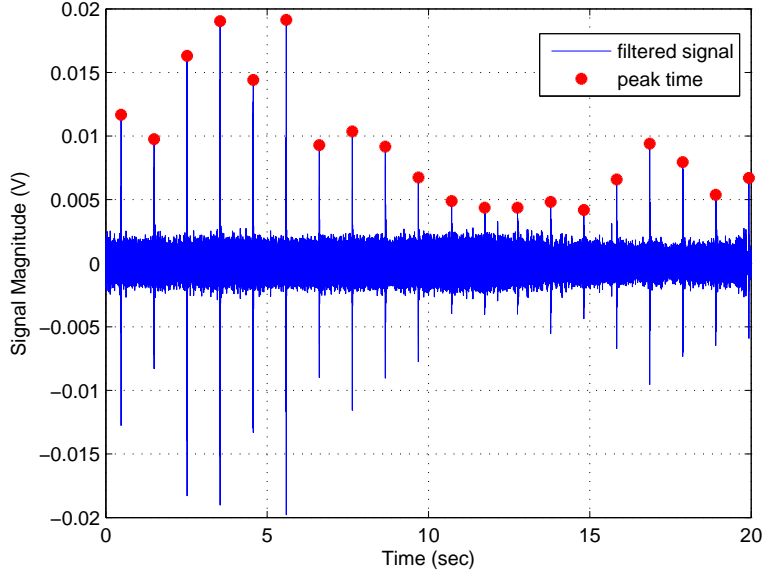


Figure 6.19: Filtered signal of received signal from the 6th hydrophone with respect to time and the peak times of this filtered signal

The covariance matrix of the system noise is given by [20].

$$Q = \begin{pmatrix} n_{rg}^2 I_3 & 0_3 & 0_3 & 0_3 & 0_3 \\ 0_3 & n_{ra}^2 I_3 & 0_3 & 0_3 & 0_3 \\ 0_3 & 0_3 & 0_3 & 0_3 & 0_3 \\ 0_3 & 0_3 & 0_3 & n_{bad}^2 I_3 & 0_3 \\ 0_3 & 0_3 & 0_3 & 0_3 & n_{bgd}^2 I_3 \end{pmatrix} \tau_s \quad (6.17)$$

where the value of n_{rg}^2 and n_{ra}^2 are related to standard deviation of the noise on the accelerometer acceleration measurement and gyro angular rate measurement, respectively. The value of n_{bad}^2 and n_{bgd}^2 are related to standard deviation of the accelerometer and gyro dynamic biases [20].

6.2.3 Measurement Model for Acoustic-based Navigation Experiment of SAGA

Since the measurements are taken at discrete intervals, the measurement vector is modeled as:

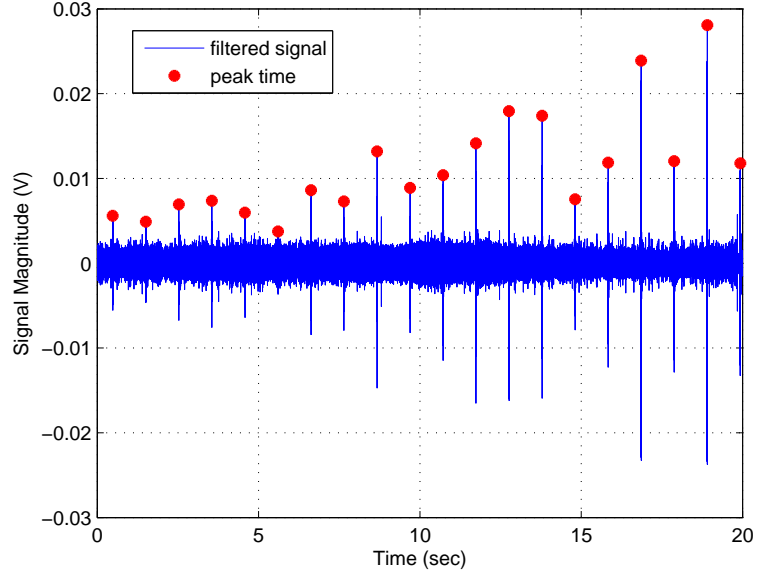


Figure 6.20: Filtered signal of received signal from the 7th hydrophone with respect to time and the peak times of this filtered signal

$$z_k = H_k x_k + v_{mk} \quad (6.18)$$

where H_k is the measurement matrix, x_k is the state vector and v_{mk} is the white noise sources. The measurement model is composed of attitude and position. The position of the vehicle comes from acoustic-based navigation system and depth sensor. Also, the position data is obtained by integrating the measured accelerations coming from the inertial navigation system. The attitude data comes from IMU (UM7). The measurement z vector is shown as:

$$\partial z_k = \begin{bmatrix} \partial \varphi_{eb}^e \\ \delta r_{eb}^e \end{bmatrix} = \begin{bmatrix} \varphi_{imu} \\ r_{acs} - r_{imu} \end{bmatrix} \quad (6.19)$$

where δr_{eb}^e is the position error between acoustic, depth measured data, r_{acs} , and inertial measured data, r_{imu} . φ_{imu}^e is the measured attitudes from IMU. It is not the attitude error since there is only one attitude measurement data. So, the output of the Kalman filter is the estimated attitudes data, not the estimated attitude error.

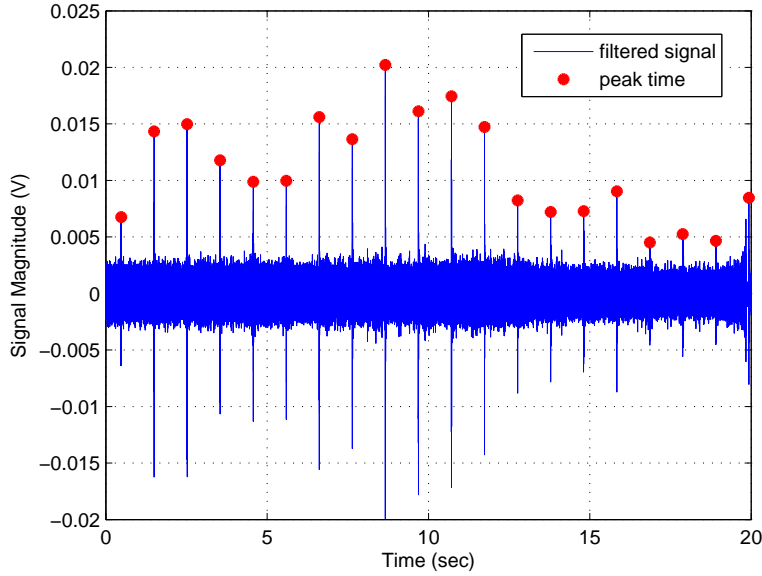


Figure 6.21: Filtered signal of received signal from the 8th hydrophone with respect to time and the peak times of this filtered signal

$$r_{acs} = \begin{bmatrix} x_{acoustic} \\ y_{acoustic} \\ z_{depth} \end{bmatrix} \quad r_{imu} = \begin{bmatrix} x_{imu} \\ y_{imu} \\ z_{imu} \end{bmatrix} \quad (6.20)$$

H_k , the measurement matrix is obtained as [20]:

$$H_k = \begin{bmatrix} -I_3 & 0_3 & 0_3 & 0_3 & 0_3 \\ 0_3 & 0_3 & -I_3 & 0_3 & 0_3 \end{bmatrix} \quad (6.21)$$

Since the noise on each component of the measurement vector is independent, the measurement covariance matrix, R is a diagonal matrix. The biases of all sensors are determined by calibration before the pool experiment. The north direction of the vehicle is fixed with respect to north direction in the earth frame for the calibrating UM7 (including magnetometer). The depth sensor is calibrated when the vehicle is on the surface of the water. After the calibration, the measurement covariance matrix components are obtained. In this study, the simplified R matrix is defined as:

Table 6.1: Detected peak times of the first, second, third and fourth received signals.

No of peaks	t_1	t_2	t_3	t_4
1	0,47542	0,47422	0,47171	0,48092
2	1,49677	1,49703	1,49698	1,50604
3	2,52423	2,52186	2,52026	2,52208
4	3,54734	3,54703	3,54594	3,55161
5	4,57467	4,57043	4,57248	4,57728
6	5,5953	5,59572	5,59634	5,59964
7	6,61657	6,62214	6,62287	6,62334
8	7,64062	7,6409	7,64304	7,64235
9	8,66704	8,66509	8,67283	8,67319
10	9,69387	9,68878	9,69379	9,69102
11	10,71509	10,71355	10,71259	10,71595
12	11,73714	11,73627	11,73823	11,73976
13	12,76196	12,7598	12,76515	12,76154
14	13,7835	13,7862	13,78663	13,7866
15	14,81052	14,80976	14,81096	14,81153
16	15,83201	15,83128	15,83404	15,83299
17	16,85924	16,85845	16,85846	16,85927
18	17,88247	17,8824	17,88035	17,8798
19	18,90676	18,90551	18,90745	18,90603
20	19,93253	19,93162	19,92823	19,93
21	20,97609	20,95459	20,9544	20,95537
22	22,66472	22,66208	21,97567	22,66526
23	24,03593	24,0294	23,00164	24,02656
24	25,06801	25,05327	24,02337	25,04927
25	26,07579	26,08215	25,04821	26,08301
26	27,09889	27,09872	26,07178	27,10632
27	28,12394	28,12593	27,09468	28,13023
28	29,14855	29,14618	28,11955	29,15465
29			29,14415	

$$R = \begin{bmatrix} R_{11} & 0_3 \\ 0_3 & R_{22} \end{bmatrix} \quad (6.22)$$

The value of R_{11} is related to the standard deviation of the measurement attitude, σ_{att} and the value of R_{22} is related to the standard deviation of the measurement position,

σ_{pos} .

Table 6.2: Detected peak times of the fifth, sixth, seventh and eighth received signals.

No of peaks	t_5	t_6	t_7	t_8
1	0,47957	0,47261	0,47579	0,4763
2	1,5049	1,49844	1,5051	1,49819
3	2,5277	2,5198	2,53003	2,52155
4	3,55101	3,54386	3,55145	3,54442
5	4,57606	4,56798	4,5761	4,56841
6	5,60108	5,5937	5,60177	5,5939
7	6,62488	6,61461	6,62445	6,61629
8	7,64646	7,63984	7,6445	7,64065
9	8,67072	8,66347	8,67197	8,66357
10	9,69733	9,6892	9,69461	9,68934
11	10,71819	10,71848	10,7186	10,71227
12	11,74461	11,74142	11,73872	11,73799
13	12,76313	12,76153	12,76194	12,76395
14	13,7885	13,78723	13,78642	13,78758
15	14,81546	14,81435	14,81183	14,81061
16	15,83322	15,83504	15,83353	15,837
17	16,85763	16,85789	16,85691	16,86148
18	17,88056	17,88103	17,88157	17,88139
19	18,90882	18,90454	18,90628	18,90645
20	19,93349	19,92935	19,92902	19,93121
21	20,95413	20,95443	20,95351	20,95391
22	21,97551	22,66585	22,66758	22,66768
23	22,99992	24,02745	24,02564	24,02923
24	24,02501	25,05169	25,04962	25,04985
25	25,04999	26,07476	26,07517	26,07369
26	26,07337	27,09913	27,10078	27,09723
27	27,09698	28,12419	28,13046	28,12243
28	28,12087	29,14829	29,154	29,14526
29	29,15264			

The depth sensor is used to support the position of the vehicle along the z axis. Depth sensor used in the experiment is shown in Fig. 6.30. Absolute pressure range of this depth sensor is 0 – 14 bar. It includes a piezoresistive pressure sensor and an ADC-Interface. It provides a 16 bit data word from a pressure and temperature dependent voltage. The depth measured from the depth sensor and the fitted polynomial is shown in Fig. 6.31 in the earth frame. The heave velocity can be obtained by taking the derivative of the measured depth data. For this purpose, the measured depth data are

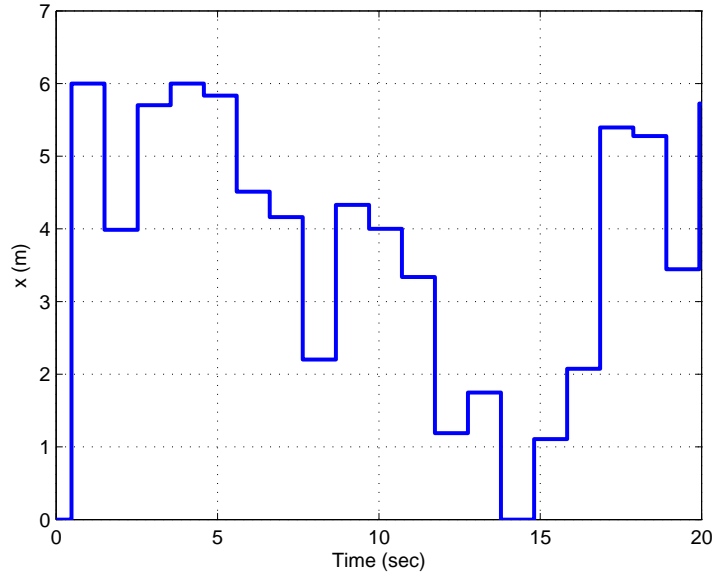


Figure 6.22: The position of the vehicle along x-axis obtained from the acoustic-based navigation system

interpolated.

6.2.4 Simulation Results for the Acoustic-based Navigation Experiment of SAGA

The system response is simulated for applied motor inputs in 3D motion. The measurement data is filtered using an indirect Kalman filter algorithm in Simulink/Matlab environment. During the experiment, applied PWM values of the right, left and the vertical thrusters are shown in Fig. 6.32.

Since the system input for the mathematical model of SAGA is force value (Nm) of each thruster, these applied PWM values are transformed into force values. Applied forces (Nm) of the right, left and vertical thrusters during the experiment are shown in Fig. 6.33.

Fig. 6.34 shows the estimated position errors in x, y and z-axes in the Earth frame coming from the output of the Kalman filter and the real position errors was defined in Chapter 4. Fig. 6.35 shows the estimated attitude errors, roll, pitch and yaw errors in the Earth frame and the real attitude errors. Since the output of the Kalman filter is the

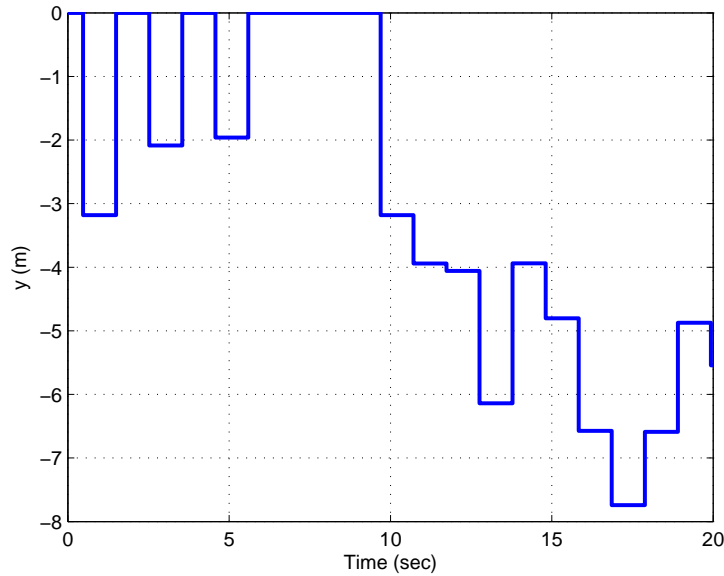


Figure 6.23: The position of the vehicle along y-axis obtained from the acoustic-based navigation system

estimated attitude, the estimated attitude error is obtained from Eqn. 4.73 in Chapter 4. Fig. 6.36 shows the estimated velocity errors, surge, sway and heave errors coming from the output of the Kalman filter and the real attitude errors.

The output of the integrated navigation solution, the corrected position, attitude and velocity are shown in figures from Fig. 6.37, to 6.39.

These estimated position and attitude data and the position and attitude information comes from the model response are used for system identification of SAGA in Chapter 7.

Difficulties of the Experiment:

Many pool experiments were done until accurate data from the acoustic based measurement system is obtained. Firstly, pinger is fixed to a known position in the pool and eight hydrophones are located separately far away from the pinger and from each other. Then, pinger sends the acoustic signal and each hydrophone is checked whether it is receiving the signal or not. It is observed that the signal completely dissipates at the of 7m from the pinger, in this preliminary experiment. Accuracy of the experiment is adversely because of the small experimental volume and short experiment

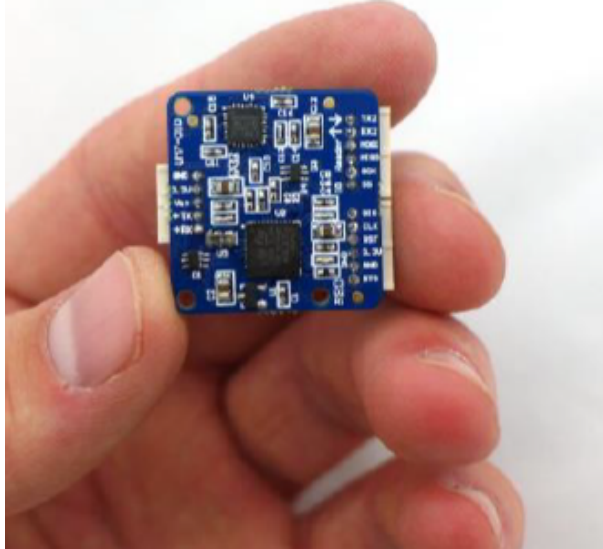


Figure 6.24: IMU (UM7) used in the experiment

duration. The connection of the each hydrophone cable effects the accuracy of the experiments since the received acoustic signals contain very high noise because of the thrusters. Another very important factor effecting the accuracy is the degree of indeterminacy in the position of the hydrophones in the pool.

6.3 Conclusion

The position of the SAGA obtained by using an integrated navigation system experimentally in this chapter. First, the acoustic based navigation system is constructed in the pool of the METU. Since the accuracy of the obtained position from the inertial measurement system is low, the position data is supported with the acoustic-measurement system and the depth sensor. System and measurement model are obtained in order to estimate the measured data using an indirect Kalman filter algorithm. Integrated navigation solutions are corrected position and attitudes which will be used in system identification of SAGA.

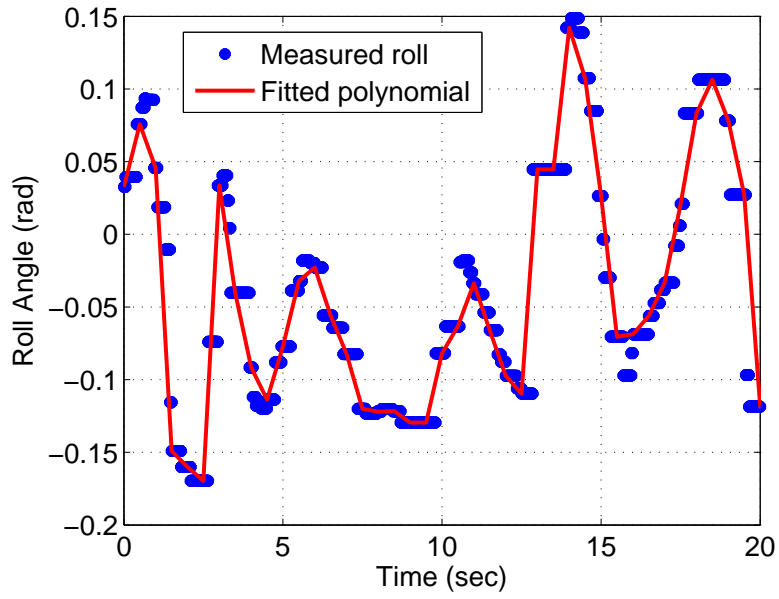


Figure 6.25: Roll angle measured from the IMU with respect to time and fitted curve of the measured roll angle

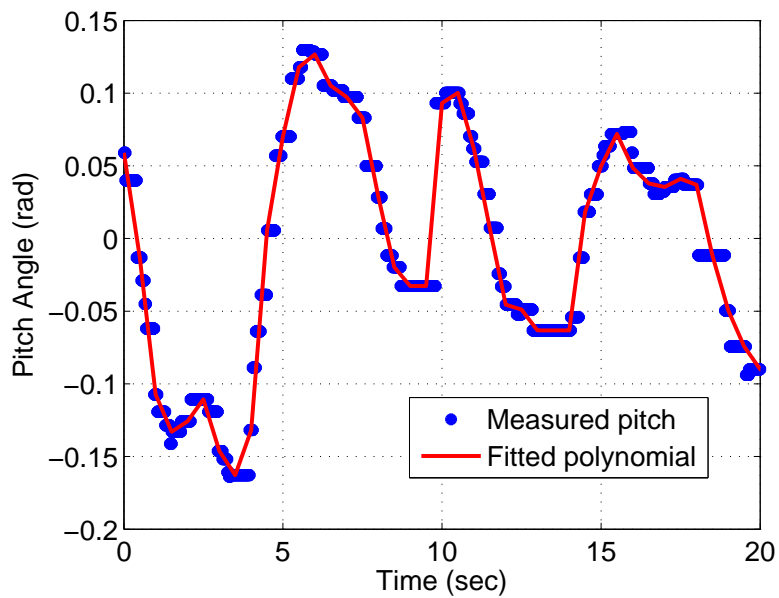


Figure 6.26: Pitch angle measured from the IMU with respect to time and fitted curve of the measured pitch angle

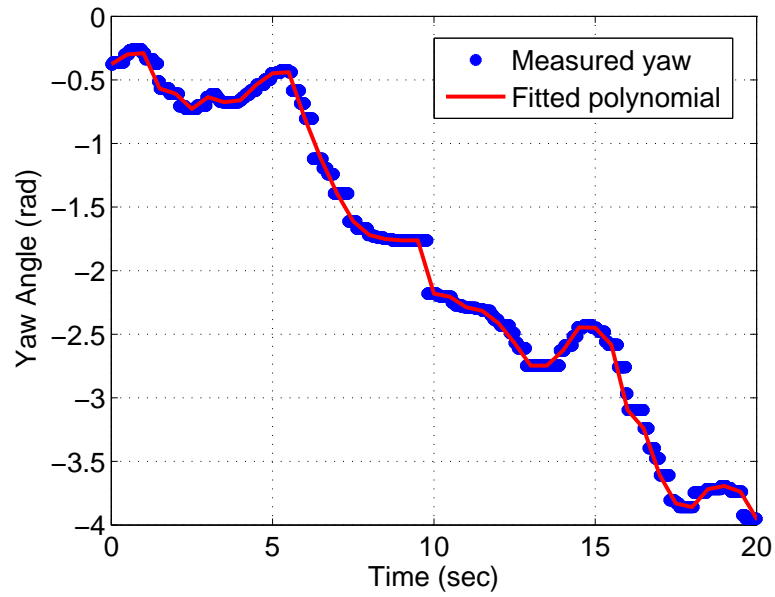


Figure 6.27: Yaw angle measured from the IMU with respect to time and fitted curve of the measured yaw angle

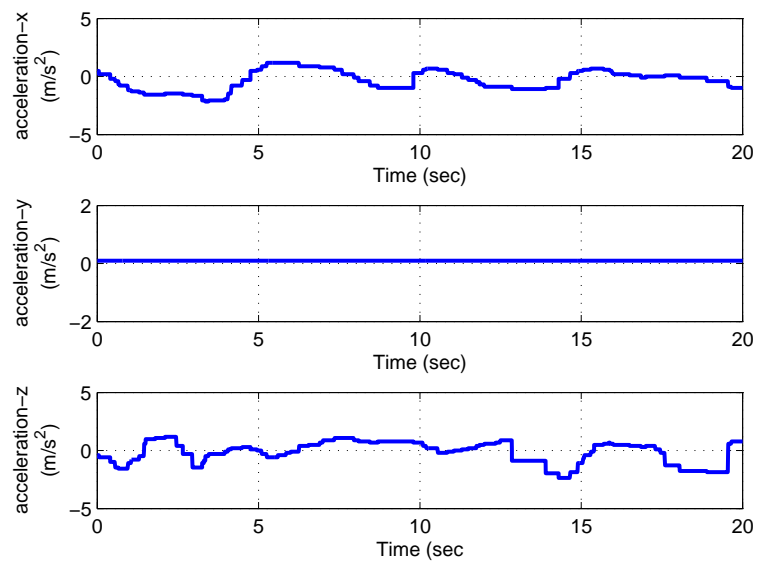


Figure 6.28: Measured translational accelerations in x, y and z-axes from the IMU in the body frame

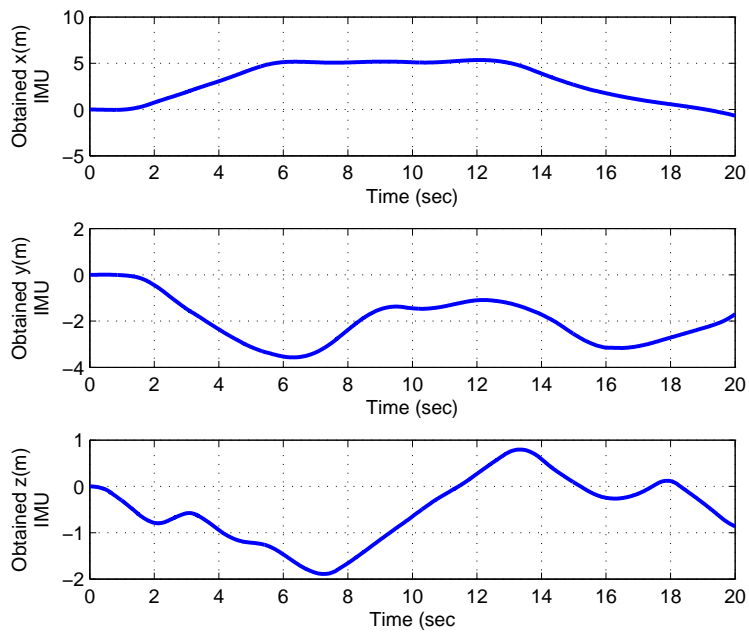


Figure 6.29: Obtained translational positions in x, y and z-axes from the IMU in the earth frame

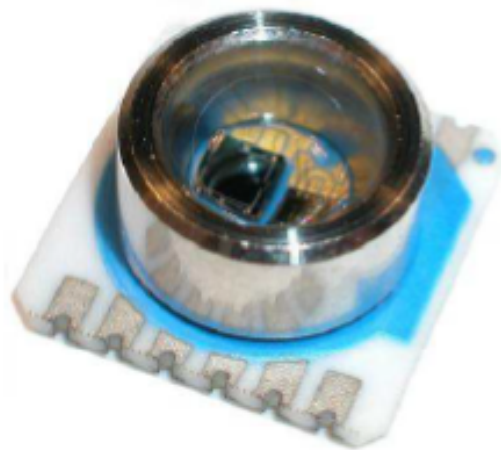


Figure 6.30: Depth sensor used in the experiment

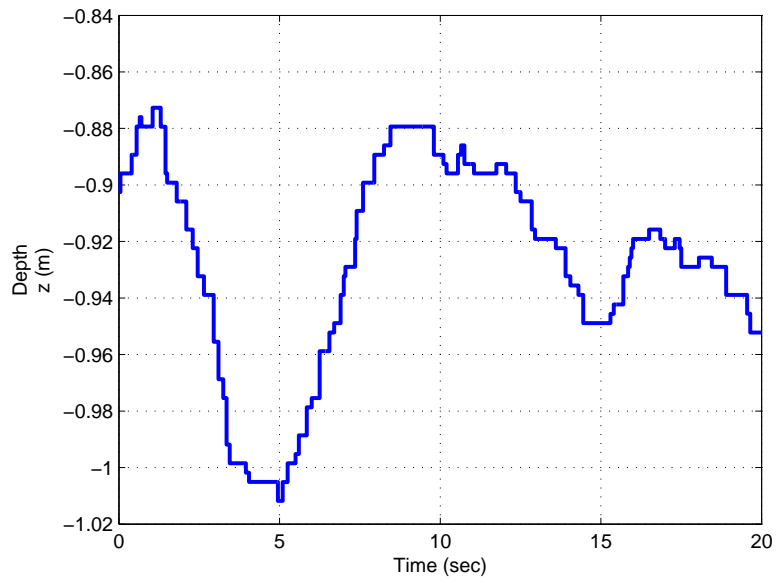


Figure 6.31: Measured depth comes from the depth sensor

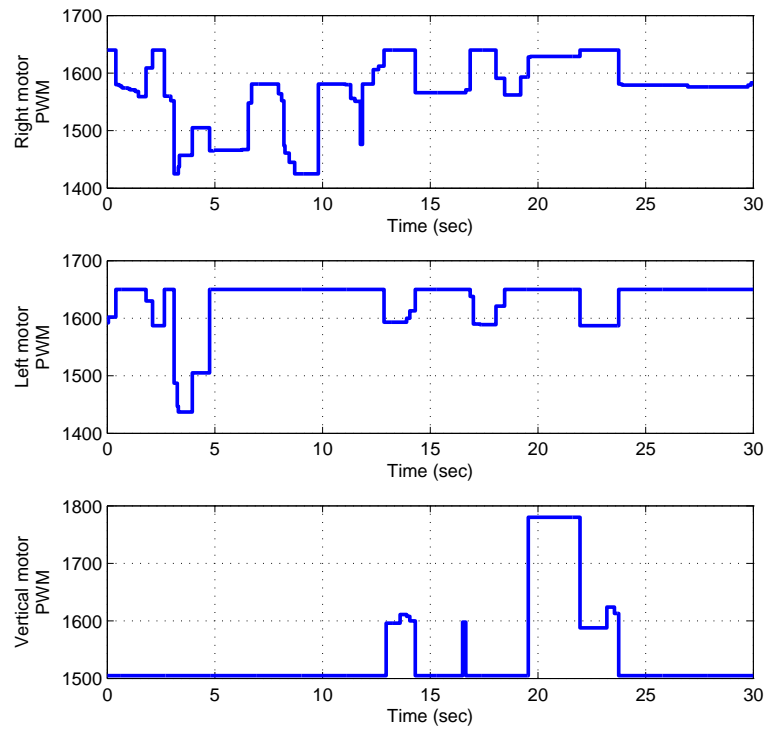


Figure 6.32: Applied PWM value of the right, left and vertical thruster during the acoustic-based navigation experiment

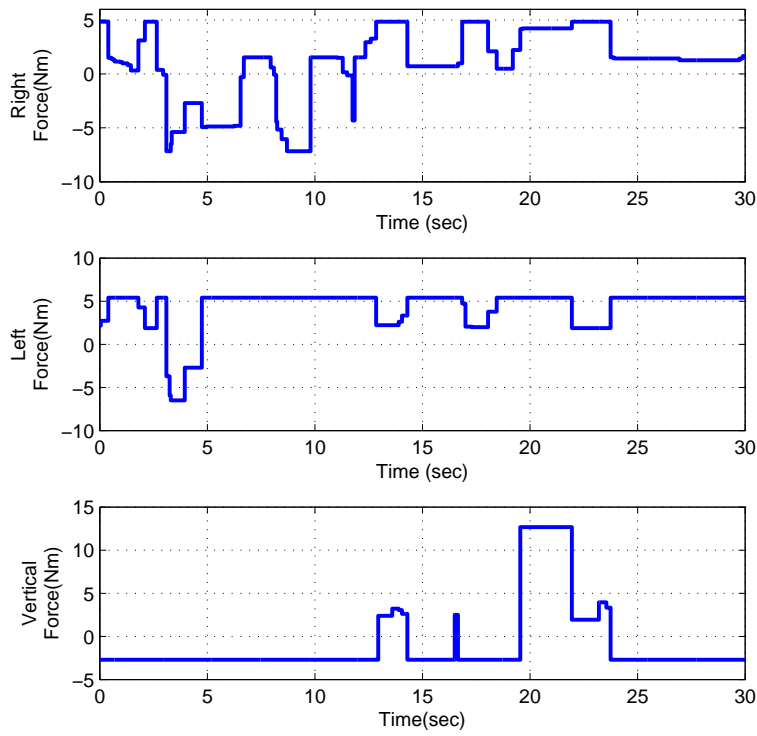


Figure 6.33: Obtained force value of the right, left and vertical thruster during the acoustic-based navigation experiment

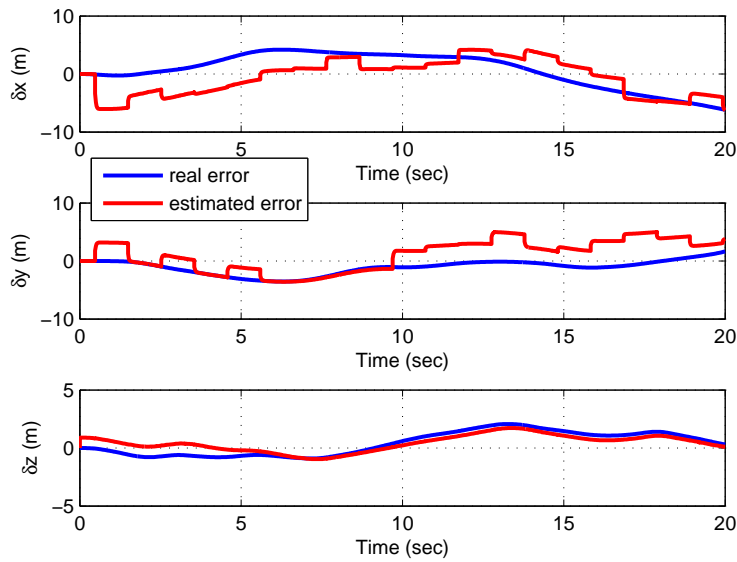


Figure 6.34: Real position errors in the x, y and z-axes (blue line) and the estimated position error in the x, y and z-axes from the Kalman filter (red line)

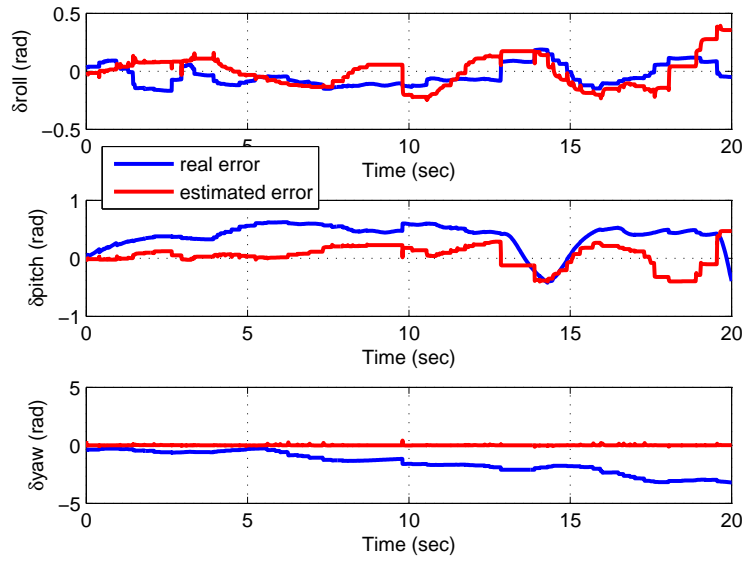


Figure 6.35: Real roll, pitch and yaw errors (blue line) and the estimated roll, pitch and yaw error from the Kalman filter (red line)

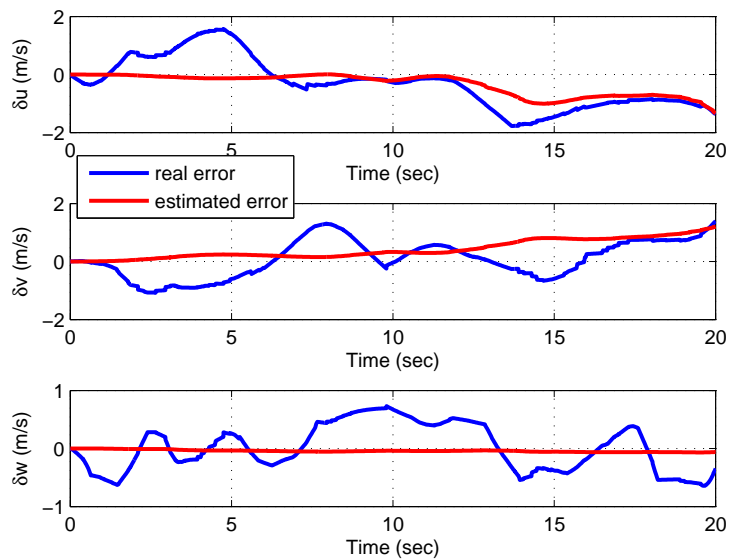


Figure 6.36: Real surge, sway and heave velocity errors (blue line) and the estimated surge, sway and heave velocity errors come from Kalman filter (red line)

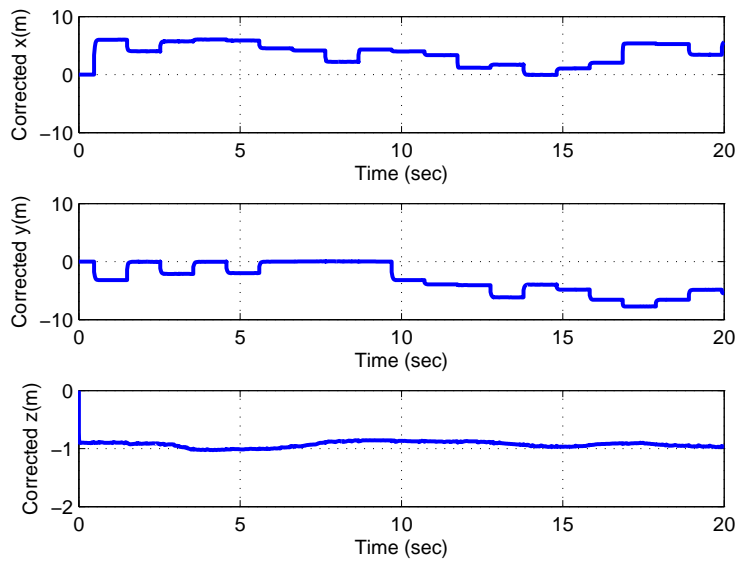


Figure 6.37: The output of the integrated navigation solution, corrected positions in the earth frame

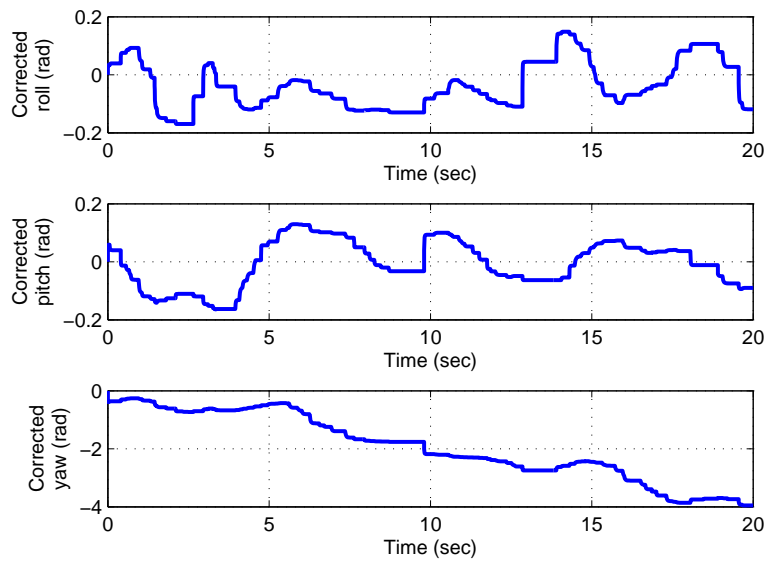


Figure 6.38: The output of the integrated navigation solution, corrected attitudes in the earth frame

CHAPTER 7

SYSTEM IDENTIFICATION OF SAGA

7.1 Introduction

Usually, mathematical models of unmanned underwater vehicles (UUV) have some unknown parameters such as added mass and damping coefficients. The added mass parameters and damping coefficients can be obtained from some hydrodynamic software programs such as WAMIT, VERES and SEAWAY and, for example, SOLIDWORKS. If the structure of the vehicle has some symmetry with respect to pitch and yaw planes, added mass parameters can be obtained approximately using the strip theory. For more accuracy, values of these parameters can be improved by a system identification study based on the navigational data from a pool experiment. In this study, the initial approximate values of these parameters are used in the original mathematical model. Then, these parameters are improved with a system identification study for coupled and uncoupled motion based on the simulation data coming from the integrated navigation system. For more accuracy, these parameters are improved with a system identification study for coupled motion based on the acoustic experimental data. System response is obtained for cases, before system identification and the after system identification. Decoupled motions of the vehicle and related parameters with this motion are shown in Table 7.1 [25].

Since SAGA cannot perform sway and roll motions under control, the related added mass parameters and drag coefficients, Y_v , Y_v^* , K_p and K_p^* cannot be identified accurately. The optimization problem that minimizes the error between the estimated measurement position and attitude values coming from the integrated navigation so-

Table 7.1: Decoupled motion of the vehicle and related parameters

Motions	Parameters
Surge	X_u and $X_{\dot{u}}$
Sway	Y_v and $Y_{\dot{v}}$
Heave	Z_w and $Z_{\dot{w}}$
Roll	K_p and $K_{\dot{p}}$
Pitch	M_q and $M_{\dot{q}}$
Yaw	N_r and $N_{\dot{r}}$

lution in Chapter 6 and the actual position and attitude values which are obtained by mathematical modeling at the time interval from $t = 0$ to $t = T$ (where T is the simulation time). This problem is formulated as in Equation 7.1. For solving the constrained non-linear optimization problem Optimization Toolbox by MATLAB is used. It provides “fmincon” as a solver for constrained non-linear optimization. Optimization Toolbox uses algorithms to solve these kinds of problems such as the interior point algorithm, SQP algorithm, the active set algorithm and trust-region reflective algorithm. Using the “fmincon” solver and trust-region reflective algorithm, the resultant optimization problem with the cost function J is solved [14]. So These unknown parameters which are added mass and drag coefficients are identified by solving the optimization problem described above several times, choosing different initial values of the unknown parameters represented by the vector, x_c

$$x_c = [x_{c1} \ x_{c2} \ x_{c3} \ x_{c4} \ x_{c5} \ x_{c6} \ x_{c7} \ x_{c8}]^T$$

$$x_c = [X_u \ X_{\dot{u}} \ Z_w \ Z_{\dot{w}} \ M_q \ M_{\dot{q}} \ N_r \ N_{\dot{r}}]^T$$

$$\text{Minimize } J = \int_0^T |d_{measured}(t) - d_{model}(t)|^2 dt$$

or

$$\text{Minimize } J = \sum_{i=0}^{N-1} w_k |x_i|^2$$

subject to

$$0 \leq x_{ci} \leq -100$$

Initial values of each parameter are selected as

$$x_{c1} = \begin{bmatrix} -5 & -15 \end{bmatrix}, x_{c2} = \begin{bmatrix} -1 & -2.5 \end{bmatrix}, x_{c3} = \begin{bmatrix} -9 & -25 \end{bmatrix}, x_{c4} = \begin{bmatrix} -1 & -5 \end{bmatrix} \quad (7.2)$$

$$x_{c5} = \begin{bmatrix} -5 & -18 \end{bmatrix}, x_{c6} = \begin{bmatrix} -0.01 & -0.5 \end{bmatrix}, x_{c7} = \begin{bmatrix} -2 & -10 \end{bmatrix}, x_{c8} = \begin{bmatrix} -0.01 & -0.09 \end{bmatrix} \quad (7.3)$$

where T is the simulation time and it is equal to the acoustic-based experiment duration, N is the data between the time interval from $t = 0$ to $t = T$, x is difference between the measurement state vector and the obtained state vector from model response and the w_k is the weight factor of each state.

The system identification steps can be summarized as:

1. Select the initial parameters from Equations 7.2 and 7.3.

2. Run the simulation.

3. Obtained the state from model response as $x_{model} = \begin{bmatrix} x_{mdl} & y_{mdl} & z_{mdl} & \theta_{mdl} & \varphi_{mdl} \end{bmatrix}^T$.

4. Solve the optimization problem which is defined in Eqn 7.1 with the state measurement, $x_{measured} = \begin{bmatrix} x_{meas} & y_{meas} & z_{meas} & \theta_{meas} & \varphi_{meas} \end{bmatrix}^T$.

5. Generate the new parameters, $x_{c,new} = \begin{bmatrix} X_u & X_i & Z_w & Z_i & M_q & M_q & N_r & N_r \end{bmatrix}^T$.

6. If the stopping criteria is satisfied, stop the algorithm and the final obtained parameters are the system identification result. Then the loop can be run with different initial values of parameters.

7. If the stopping criteria is not satisfied simulation is run with the new parameters

obtained from step 5. Until the stopping criteria is satisfied, the loop continues from step 2 to step 6.

7.2 System Identification Based on Simulation Data

System identification is performed using the data generated from response of the vehicle model even though it is more accurate to do it using the experimental data. In the simulation-based system identification, measured data obtained from the model response is generated by adding the noise according to the accuracy of the sensors. For the system identification study, the uncoupled motion model, surge, yaw, pitch or coupled motion model of the vehicle can be used.

7.2.1 Uncoupled Motion Test Based on Simulation Data

Surge Motion Test Based on Simulation Data

If the right and left thrusters are activated only, with equal force, the equation of the resultant motion in six degrees of freedom is expressed as

$$\sum X = (m - X_{\dot{u}}) \dot{u} - (m - Y_{\dot{v}}) vr + (m - Z_{\dot{w}}) wq - X_u u \quad (7.4)$$

The vehicle moves in the x-direction with surge speed, u . The equation of uncoupled surge motion in single-degree-of freedom is simplified as:

$$\sum X = (m - X_{\dot{u}}) \dot{u} - X_u u \quad (7.5)$$

where,

$\sum X$: The total force with direction x direction,

m : The mass of the vehicle,

u : The surge speed of the vehicle.

For the surge motion test, the measured navigation data based on simulation is generated from vehicle's model response. It is considered that the position data comes from acoustic and vision-based navigation system and inertial navigation system for surge motion test. They are shown in Fig. 7.1

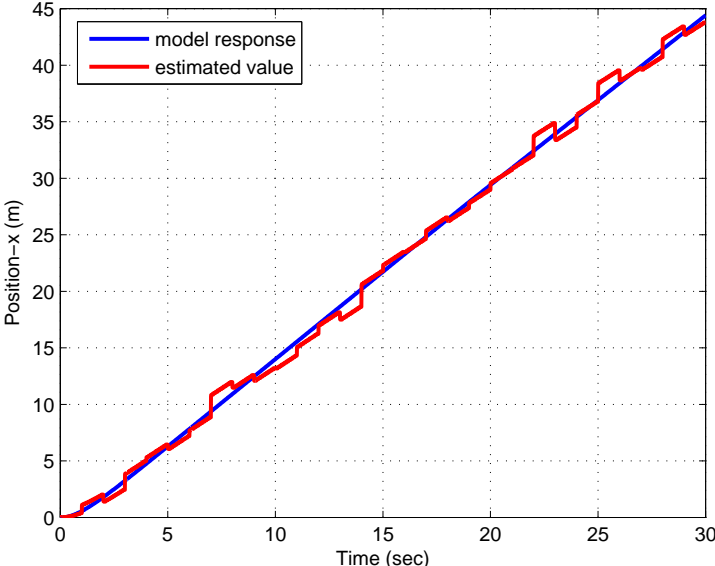


Figure 7.1: Position in the x-axis coming from the model response and the estimated position in the x-axis from the integrated navigation solution for the surge motion test based on simulation data

Figure 7.1 shows the position in the x-axis from the model response and the estimated value of the position in the x-axis from Kalman filter. The added mass and damping coefficients related to surge motion are obtained by solving the optimization problem which is defined as in Eqn. 7.1 using the simulation-based data as shown in Fig. 7.1.

Table 7.2: Optimization results for the surge motion test based on simulation data

Parameters	Obtained value	Actual value
X_u	-26.48	-13
$X_{\dot{u}}$	-19.6	-1.94

Yaw Motion Test Based on Simulation Data

If the right and left thrusters are activated only, with different forces, the equation of resultant motion in six degrees of freedom is defined as

$$\sum X = (m - X_{\dot{u}}) \dot{u} - (m - Y_{\dot{v}}) vr + (m - Z_{\dot{w}}) wq - X_u u \quad (7.6)$$

$$\sum N = (I_z - N_{\dot{r}}) \dot{r} + (X_{\dot{u}} - Y_{\dot{v}}) vu + (I_y - I_x + K_{\dot{p}} - M_{\dot{q}}) qp - N_r r \quad (7.7)$$

The vehicle moves in the xy plane with surge speed, u and yaw angle, ψ . The equation of uncoupled yaw motion is simplified into a two single-degree-of freedom motions as

$$\begin{bmatrix} \sum X \\ \sum N \end{bmatrix} = \begin{bmatrix} (m - X_{\dot{u}}) \dot{u} - X_u u \\ (I_z - N_{\dot{r}}) \dot{r} - N_r r \end{bmatrix} \quad (7.8)$$

where,

$\sum X$: The total force with direction x direction,

m : The mass of the vehicle,

u : The surge speed of the vehicle,

$\sum N$: The total moment in the yaw plane,

I_z : The inertia tensor of the vehicle in the z-axis,

r : The angular rate component in the z-axis.

For the yaw motion test, the measured navigation data based on simulation is generated from vehicle's model response. The position data comes from the acoustic and vision-based navigation systems and inertial navigation system for the yaw motion test. They are shown in Fig. 7.2 and Fig. 7.3. The attitude data comes from the inertial navigation system and the magnetic compass as shown in Fig. 7.4.

All these estimated positions and attitude are used in the system identification for the yaw motion test. The added mass and damping coefficients related to yaw motion are obtained by solving the optimization problem which is defined as in Eqn. 7.1.

Pitch Motion Test Based on Simulation Data

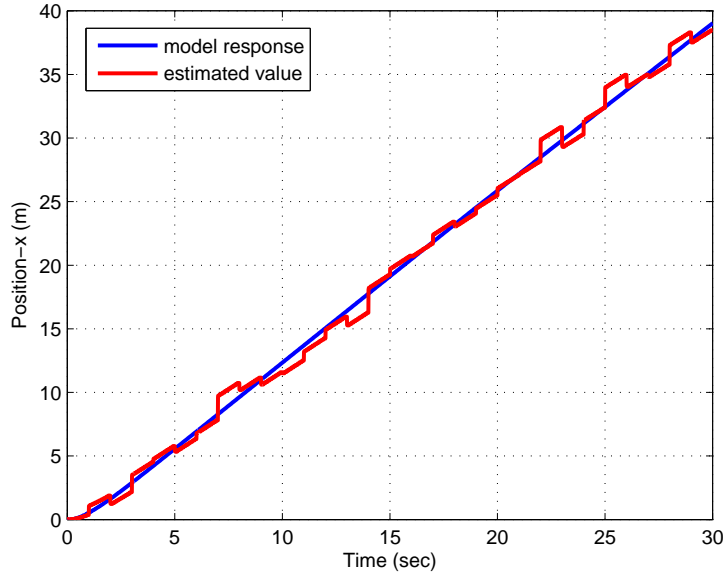


Figure 7.2: Position in the x-axis coming from the model response (blue line) and the estimated position in the x-axis from the integrated navigation solution (red line) for the yaw motion test based on simulation data

Table 7.3: Optimization results for the yaw motion test based on simulation data

Parameters	Obtained Value	Actual Value
X_u	-7.328	-13
$X_{\dot{u}}$	-13.7	-1.94
N_r	-2.0385	-5
$N_{\dot{r}}$	-12.998	-0.03

If the vertical thruster is activated only, the equation of resultant motion in six degrees of freedom is defined as

$$\sum Z = (m - Z_{\dot{w}}) \dot{w} - (m - X_{\dot{u}}) uq + (m - Y_{\dot{v}}) vp - Z_w w \quad (7.9)$$

$$\sum M = (I_y - M_{\dot{q}}) \dot{q} + (Z_{\dot{w}} - X_{\dot{u}}) uw + (I_x - I_z + N_{\dot{r}} - K_{\dot{p}}) rp - M_q q + (z_G - z_B) W \sin\theta \quad (7.10)$$

The vehicle moves in the xz plane (i.e., the pitch plane) with heave speed, (w) and pitch angle, θ . The equation of uncoupled pitch motion is obtained from two single-

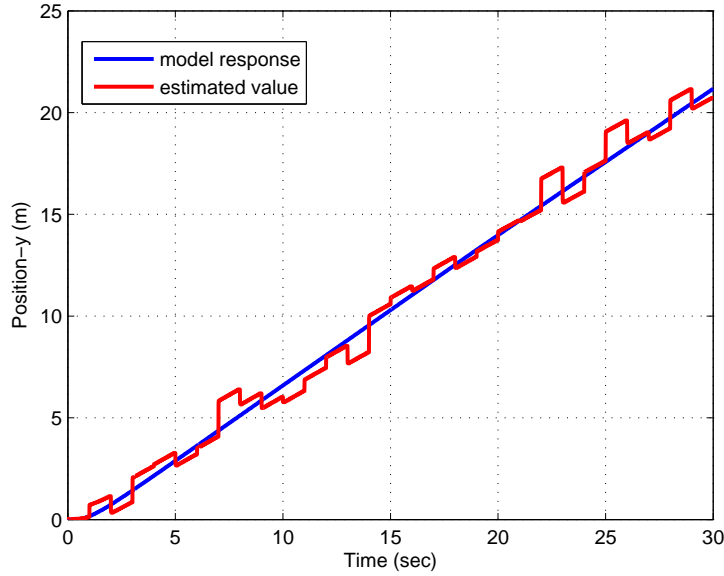


Figure 7.3: Position in the y-axis coming from the model response (blue line) and the estimated position in the y-axis from the integrated navigation solution (red line) for the yaw motion test based on simulation data

degree-of freedom motions as.

$$\begin{bmatrix} \sum Z \\ \sum M \end{bmatrix} = \begin{bmatrix} (m - Z_{\dot{w}}) \dot{w} - Z_w w \\ (I_y - M_{\dot{q}}) \dot{q} - M_q q + (z_G - z_B) W \sin\theta \end{bmatrix} \quad (7.11)$$

where,

$\sum Z$: The total force in the xz plane,

$\sum M$: The total moment in the xz plane,

z_G, z_B : The gravity and buoyancy forces component along the z axis,

I_y : The inertia tensor of the vehicle along the y axis,

w, q : The heave speed in the z direction and the angular rate component in the y-axis.

For the pitch motion test, the measured navigation data based on simulation is generated from vehicle's model response. It is considered that the position data comes from acoustic and inertial navigation systems and the depth sensor for pitch motion.

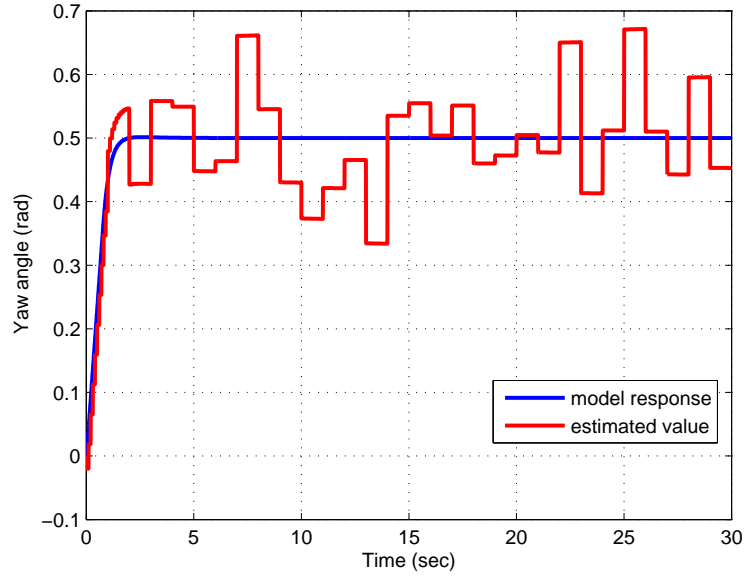


Figure 7.4: Yaw angle coming from the model response (blue line) and the estimated yaw angle from the integrated navigation solution (red line) for the yaw motion test based on simulation data

They are shown in Fig. 7.5 and Fig. 7.6. The attitude data comes from the inertial navigation system and the magnetic compass as shown in Fig. 7.7.

All measured data are filtered using a Kalman filter algorithm as in Section 4.7. Fig. 7.5 and Fig. 7.6 show the position in x and z- axes from model response and the estimated value of the position in x and z- axes from Kalman filter, respectively. Fig. 7.7 shows the pitch angle from the model response and the estimated pitch angle from Kalman filter.

All these estimated positions and angles will be used for system identification. The added mass and damping coefficients related to pitch motion are obtained by solving the optimization problem which is defined in Eqn. 7.1.

7.2.2 Coupled Motion Test Based on Simulation Data

The vehicle moves in 3D by activating right, left and vertical thrusters. Since SAGA cannot perform sway and roll motions under control, the coupled motion of SAGA in 4 DOF is expressed in Eqn. 7.12.

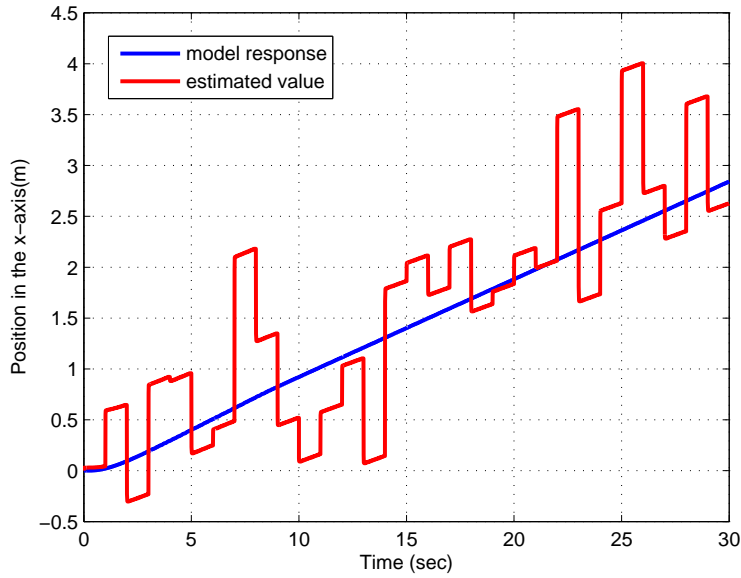


Figure 7.5: Position in the x-axis coming from the model response (blue line) and the estimated position in the x-axis from the integrated navigation solution (red line) for the pitch motion test based on simulation data

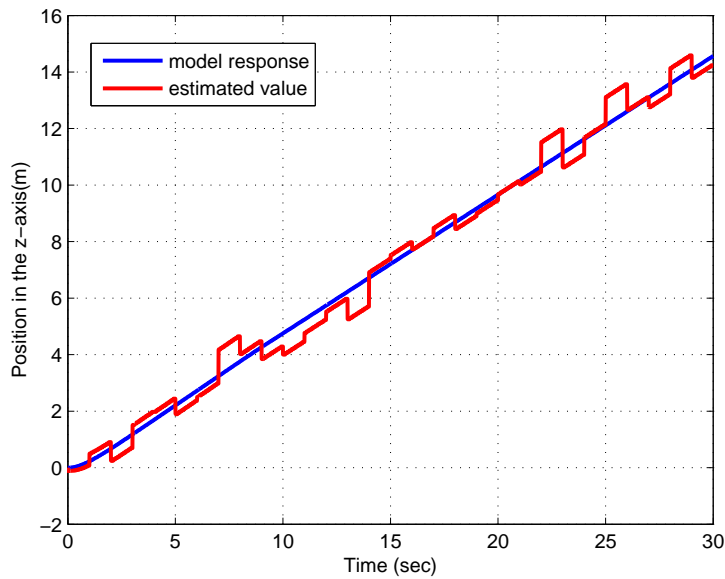


Figure 7.6: Position in the z-axis coming from the model response (blue line) and the estimated position in the z-axis from the integrated navigation solution (red line) for the pitch motion test based on simulation data

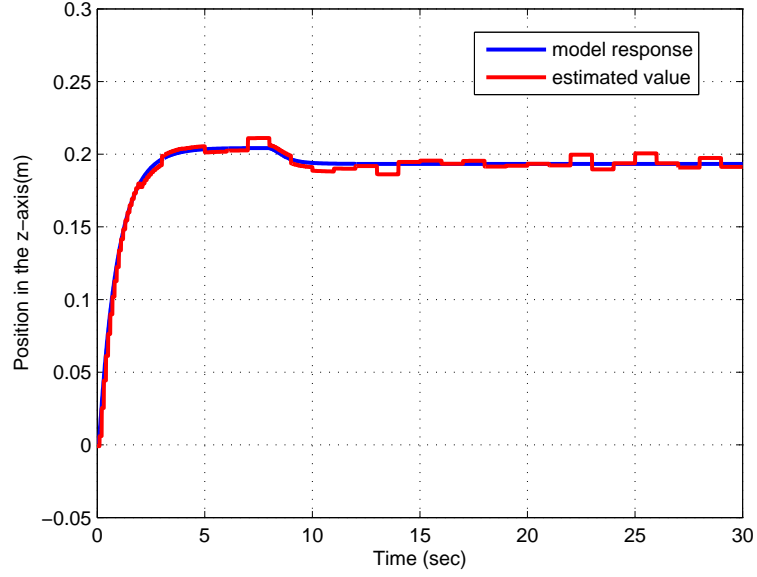


Figure 7.7: Pitch angle coming from the model response (blue line) and the estimated pitch angle from the integrated navigation solution (red line) for the pitch motion test based on simulation data

Table 7.4: Optimization results for pitch motion test based on simulation data

Parameters	Obtained value	Actual value
Z_w	-40.35	-19
$Z_{\dot{w}}$	-21.66	-3.94
M_q	-10.44	-13
$M_{\dot{q}}$	-0.161	-0.1

$$\begin{bmatrix} \sum X \\ \sum Z \\ \sum M \\ \sum N \end{bmatrix} = \begin{bmatrix} (m - X_{\dot{u}}) \dot{u} - (m - Y_{\dot{v}}) vr + (m - Z_{\dot{w}}) wq - X_u u \\ (m - Z_{\dot{w}}) \dot{w} - (m - X_{\dot{u}}) uq + (m - Y_{\dot{v}}) vp - Z_w w \\ (I_y - M_{\dot{q}}) \dot{q} + (Z_{\dot{w}} - X_{\dot{u}}) uw + (I_x - I_z + N_{\dot{r}} - K_{\dot{p}}) rp - \\ \quad - M_q q + (z_G - z_B) \\ (I_z - N_{\dot{r}}) \dot{r} + (X_{\dot{u}} - Y_{\dot{v}}) vu + (I_y - I_x + K_{\dot{p}} - M_{\dot{q}}) qp - N_r r \end{bmatrix} \quad (7.12)$$

For the 3D motion test, the measured navigation data based on simulation is generated from vehicle's model response. It is known that the position data comes from the acoustic and vision-based navigation systems, inertial navigation system and the

depth sensor for 3D motion test. They are shown in Fig. 7.8, 7.9 and Fig. 7.10. The attitude data comes from the inertial navigation system and magnetic compass. The measured yaw and pitch angles are shown in figures Fig. 7.11 and Fig. 7.12, respectively.

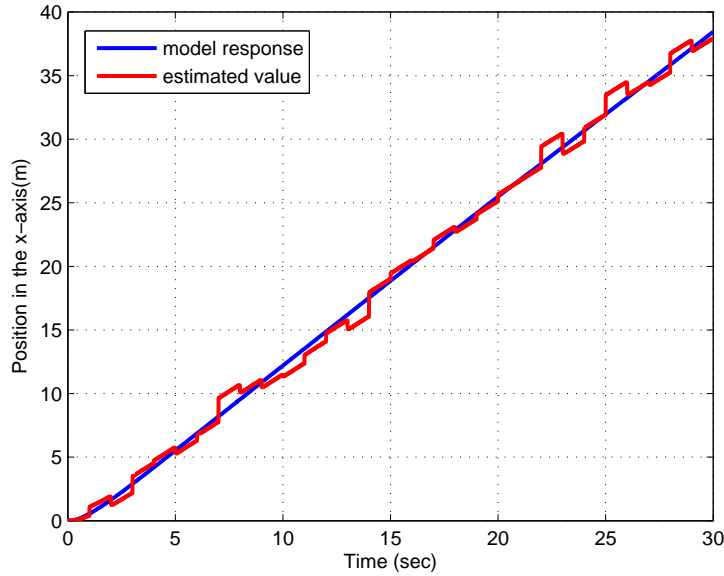


Figure 7.8: Position in the x-axis coming from the model response (blue line) and the estimated position in the x-axis from the integrated navigation solution (red line) for the coupled motion test based on simulation data

For the coupled motion test, added mass and added mass and drag parameters are determined by minimizing the cost function J defined in Eqn. 7.1 using the “fmincon” algorithm. In this function, $d_{measured}$ comes from the estimated navigation data for multisensor integration output and d_{model} is generated from the mathematical model response of SAGA. The histogram of the obtained parameters from optimization results for the different initial values of parameters are shown in Figures 7.13, 7.14, 7.15, 7.16, 7.17 and 7.18. Hence, the damping coefficients and the added mass parameters are recuperated by taking the average of the parameters obtained from optimization for different initial values. They are shown in Tables 7.5 and 7.6.

After the system identification study based on simulated data, the mathematical modeling of SAGA is improved using these recuperated damping and added mass parameters obtained from the system identification study. The responses of the mathematical

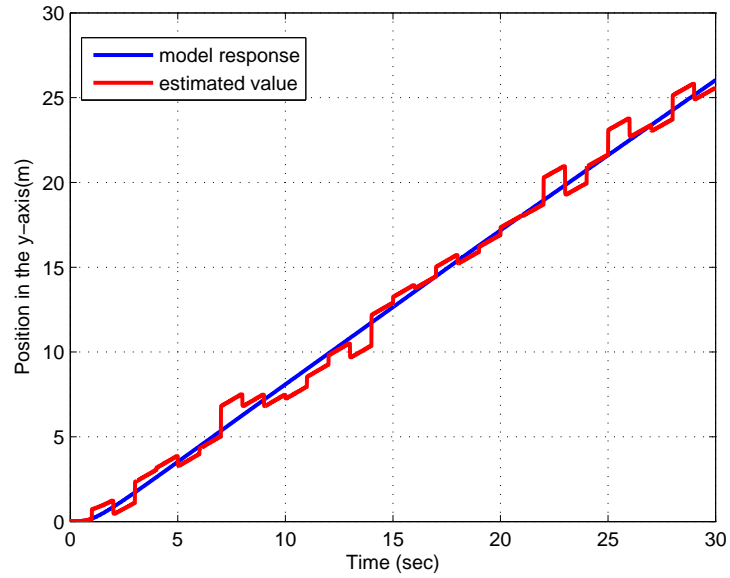


Figure 7.9: Position in the y-axis coming from the model response (blue line) and the estimated position in the y-axis from the integrated navigation solution (red line) for the coupled motion test based on simulation data

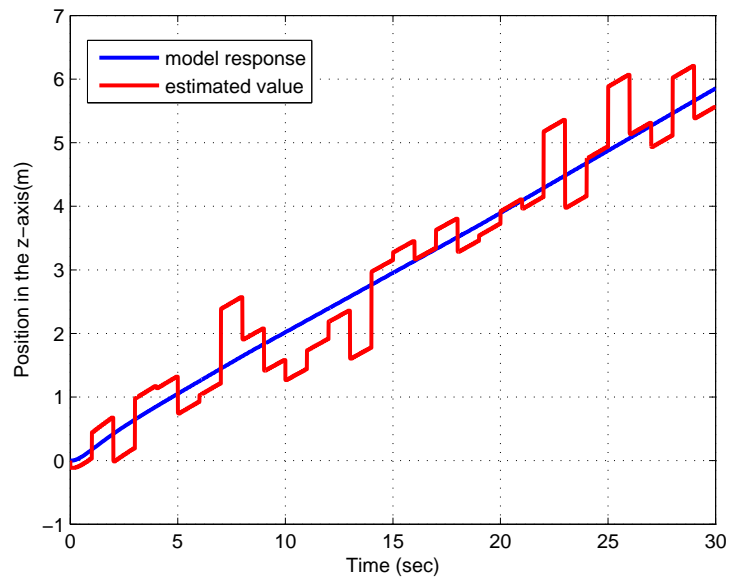


Figure 7.10: Position in the z-axis coming from the model response (blue line) and the estimated position in the z-axis from the integrated navigation solution (red line) for the coupled motion test based on simulation data

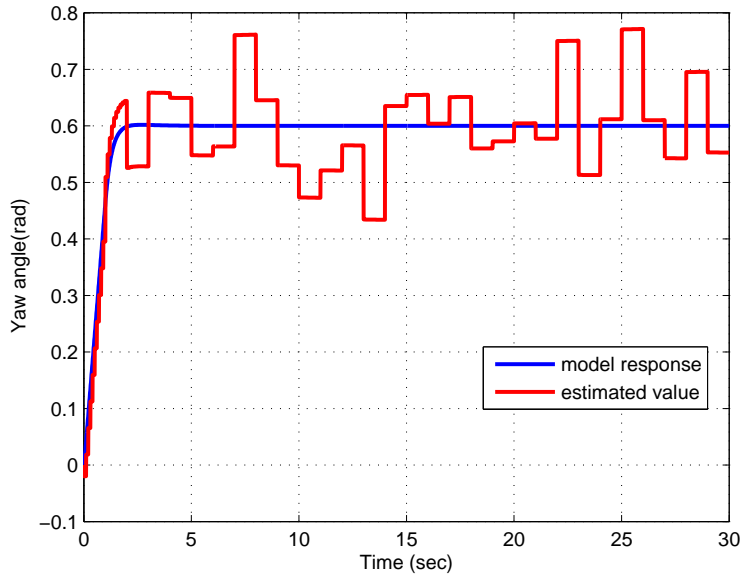


Figure 7.11: Yaw angle coming from the model response (blue line) and the yaw angle from the integrated navigation solution (red line) for the coupled motion test based on simulation test

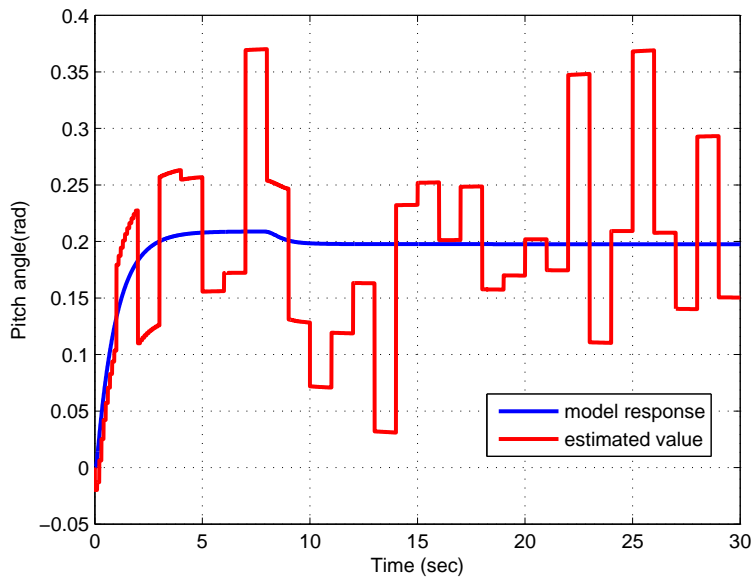


Figure 7.12: Pitch angle coming from the model response (blue line) and the pitch angle from the integrated navigation solution (red line) for the coupled motion test based on simulation test

model of SAGA using the parameters before and the after the system identification study are compared with the measured data. Figures 7.19, 7.20 and 7.21 show the es-

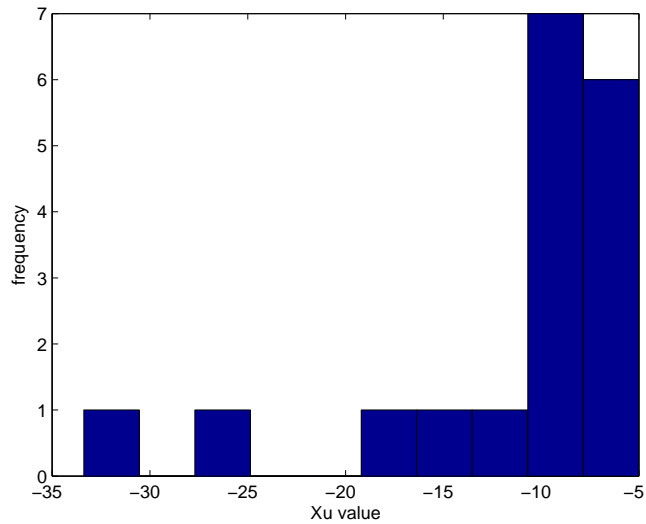


Figure 7.13: The histogram of X_u value in the system identification based on simulation data for coupled motion

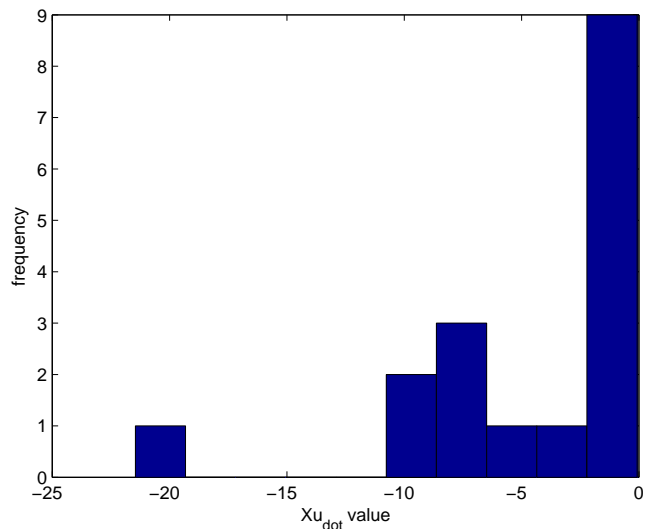


Figure 7.14: The histogram of \dot{X}_u value in the system identification based on simulation data for coupled motion

estimated positions in x, y, and z axes, and the positions in x, y and z axes obtained from the mathematical model response of SAGA before and the after system identification, respectively. Figures 7.22 and 7.23 show the estimated yaw and pitch angles and the yaw and pitch angles obtained from the mathematical model response of SAGA before and after the system identification, respectively. As seen results, results in

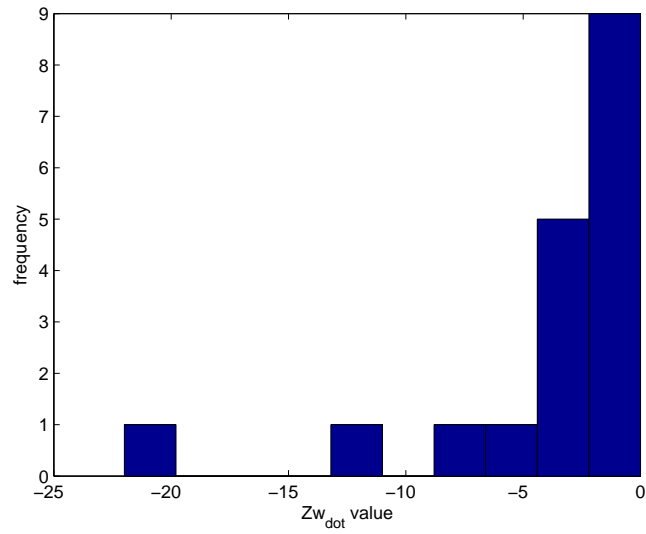


Figure 7.15: The histogram of $Z_{\dot{w}}$ value in the system identification based on simulation data for coupled motion

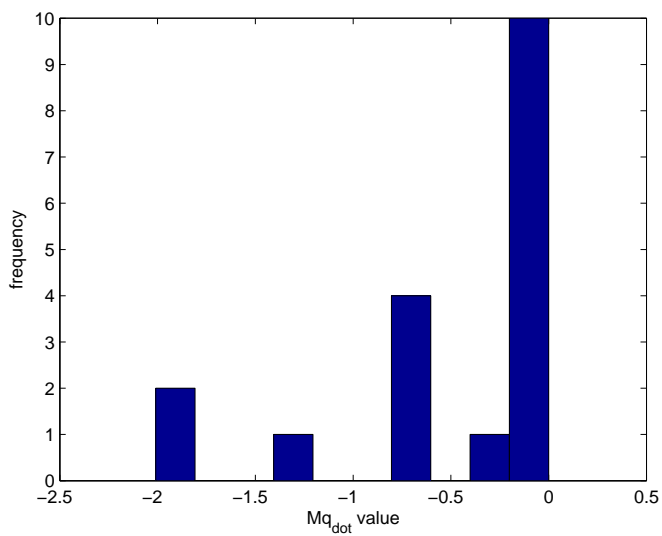


Figure 7.16: The histogram of $M_{\dot{q}}$ value in the system identification based on simulation data for coupled motion

coupled motion are more accurate than the uncoupled motion.

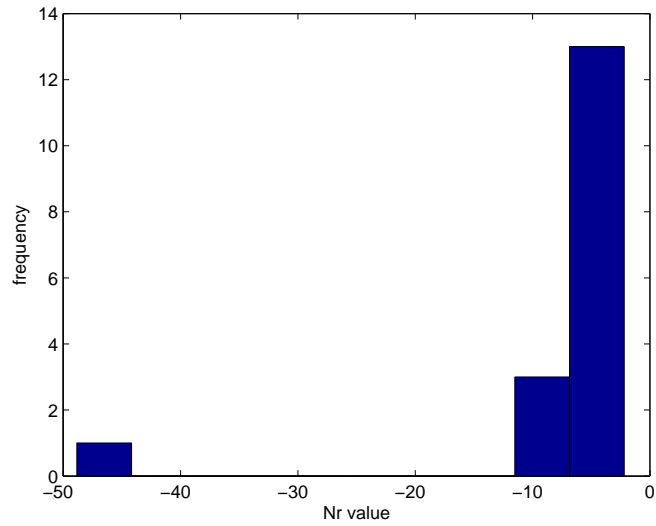


Figure 7.17: The histogram of N_r value in the system identification based on simulation data for coupled motion

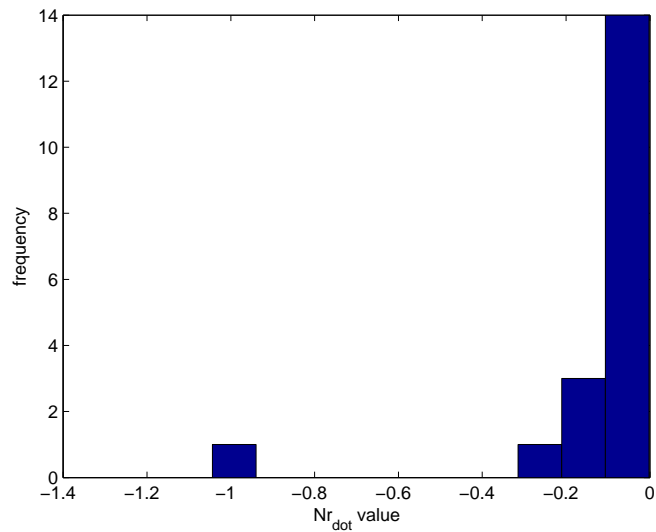


Figure 7.18: The histogram of $N_{r \cdot}$ value in the system identification based on simulation data for coupled motion

7.3 System Identification Based on Acoustic Experimental Data

The system identification is performed using the acoustic-based navigation data in Chapter 6. The optimization problem that minimizes the error between the estimated measurement position and the attitude value which is taken from the integrated navi-

Table 7.5: Damping coefficients as the results of optimization for coupled motion test based on simulation data

Obtained damping coefficients	Actual damping coefficients
$X_u = -13.57$	$X_u = -13$
$Z_w = -19$	$Z_w = -19$
$M_q = -13$	$M_q = -13$
$N_r = -3.57$	$N_r = -5$

Table 7.6: Added mass parameters as the results of optimization for system identification for coupled motion test based on simulation data

Obtained added mass parameters	Actual added mass parameters
$X_{\dot{u}} = -1.99$	$X_{\dot{u}} = -1.94$
$Z_{\dot{w}} = -3.14$	$Z_{\dot{w}} = -3.94$
$M_{\dot{q}} = -0.113$	$M_{\dot{q}} = -0.17$
$N_{\dot{r}} = -0.095$	$N_{\dot{r}} = -0.03$

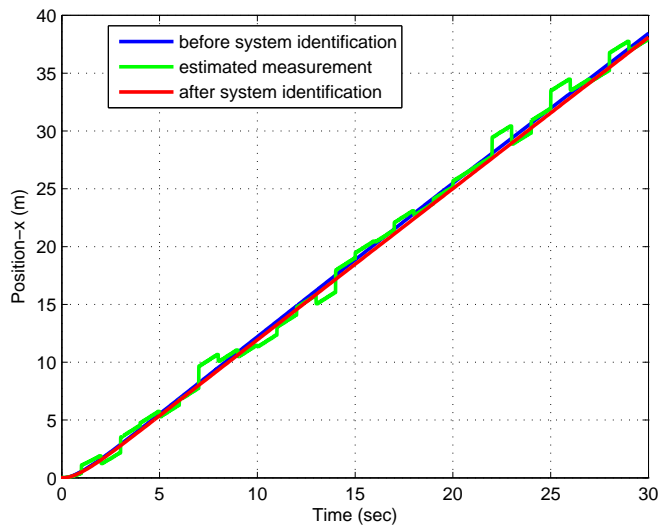


Figure 7.19: Estimated position in the x-axis from the Kalman filter (green line), the position in the x-axis from the system model response before system identification based on simulated data (blue line) and the position in the x-axis from the system model response after system identification based on simulated data (red line) with respect to time for the coupled motion

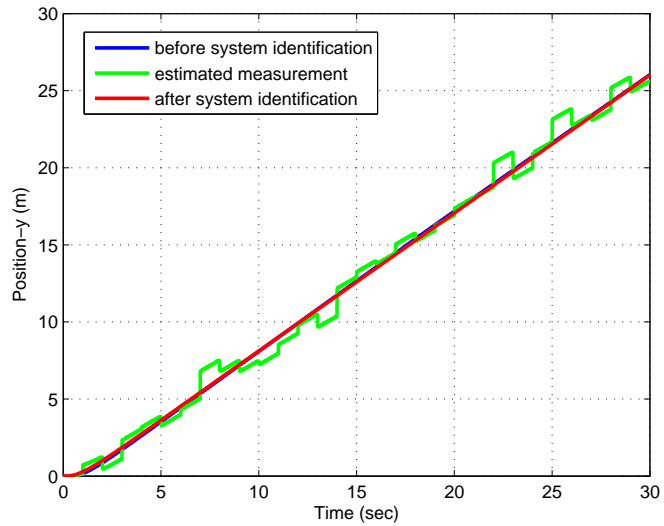


Figure 7.20: Estimated position in the y-axis from the Kalman filter (green line), the position in the y-axis from the system model response before system identification based on simulated data (blue line) and the position in the y-axis from the system model response after system identification based on simulated data (red line) with respect to time for the coupled motion

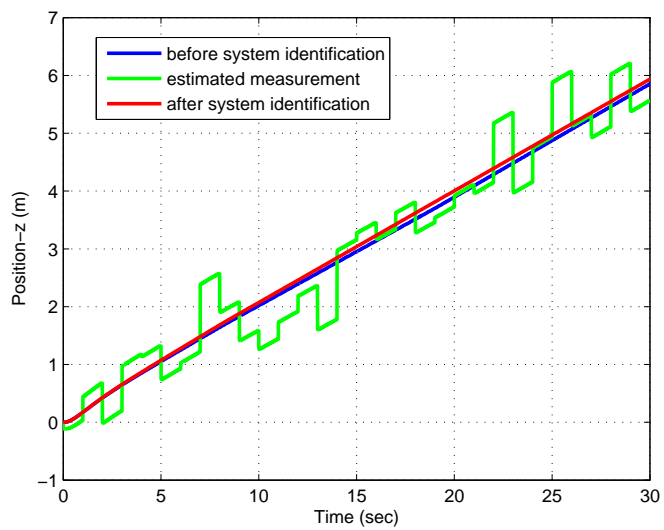


Figure 7.21: Estimated position in the z-axis from the Kalman filter (green line), the position in the z-axis from the system model response before system identification based on simulated data (blue line) and the position in the z-axis from the system model response after system identification based on simulated data (red line) with respect to time for the coupled motion

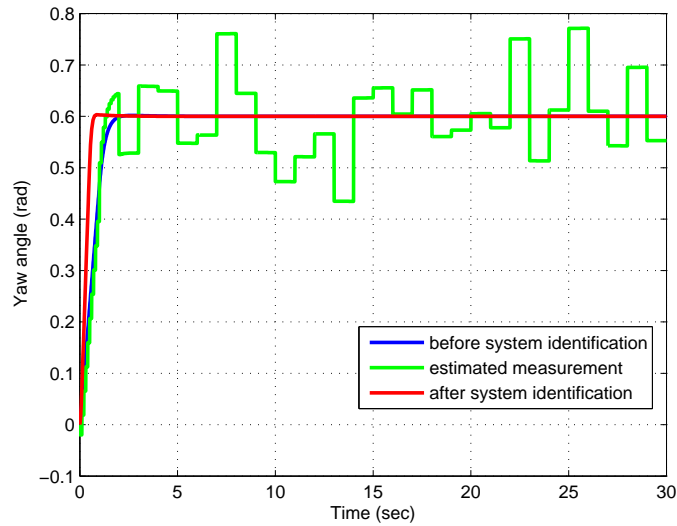


Figure 7.22: Estimated yaw angle from the Kalman filter (green line), the yaw angle from the system model response before system identification basen on simulated data (blue line) and the yaw angle from the system model response after system identification based on simulated data (red line) with respect to time

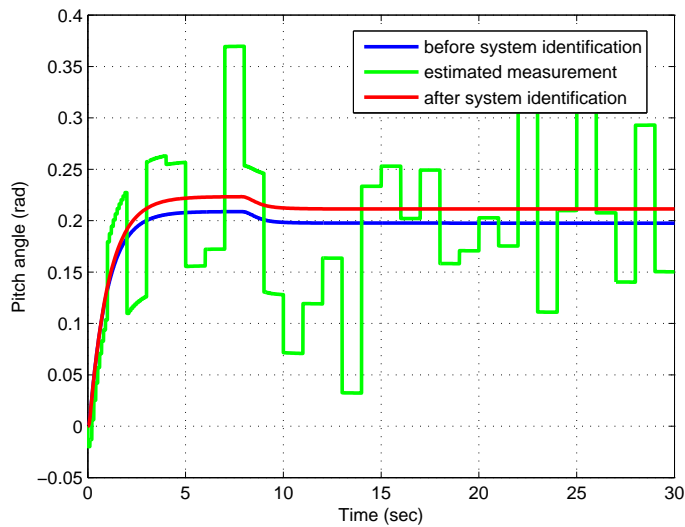


Figure 7.23: Estimated pitch angle from the Kalman filter (green line), the pitch angle from the system model response before system identification basen on simulated data (blue line) and the pitch angle from the system model response after system identification based on simulated data (red line) with respect to time

gation system experimentally and the position and attitude values which are obtained from the mathematical model. This problem was defined in Eqn. 7.1.

Table 7.7: Damping coefficients as the results of optimization for system identification based on the acoustic experimental data

Obtained damping coefficients	Actual damping coefficients
$X_u = -10.6$	$X_u = -13$
$Z_w = -27.516$	$Z_w = -19$
$M_q = -8.8643$	$M_q = -13$
$N_r = -7.3962$	$N_r = -5$

The damping coefficients, X_u , Z_w , M_q , N_r and the added mass parameters, $X_{\dot{u}}$, $Z_{\dot{w}}$, $M_{\dot{q}}$, $N_{\dot{r}}$ are obtained from the solution of the associated optimization problem using the “fmincon” algorithm. The histogram of the obtained parameters from optimization results for different initial values of parameters are shown in Figures 7.24, 7.25, 7.26, 7.27, 7.28, 7.29, 7.30 and 7.31. Hence, the damping coefficients and the added mass parameters are recuperated as shown in Tables 7.7 and 7.8 according to their histogram.

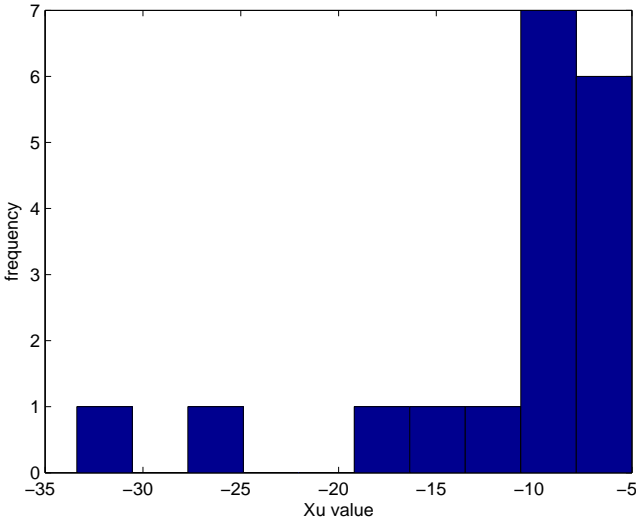


Figure 7.24: The histogram of X_u value in the system identification based on the acoustic experimental data for coupled motion

After the system identification study based on acoustic experimental data, the mathematical modeling of SAGA is improved using these recuperated damping and added mass parameters obtained from the system identification study. The responses of the mathematical model of SAGA using the parameters before and the after the system

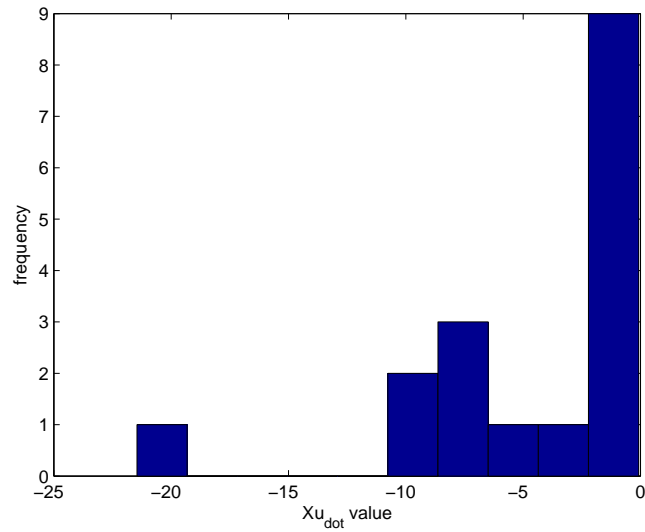


Figure 7.25: The histogram of $X_{\dot{u}}$ value in the system identification based on the acoustic experimental data for coupled motion

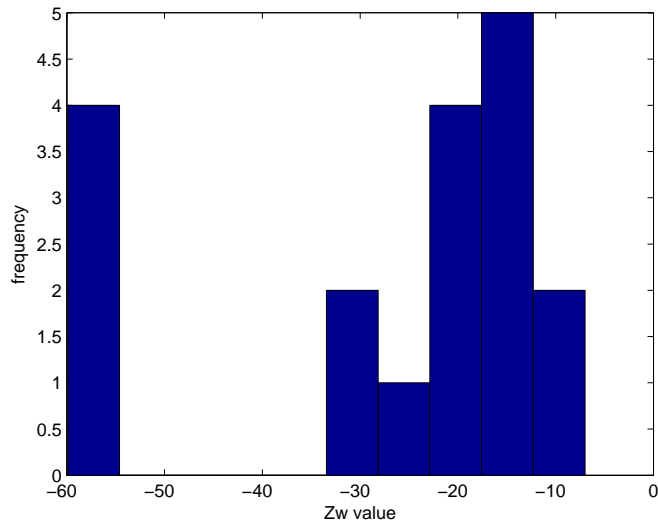


Figure 7.26: The histogram of Z_w value in the system identification based on the acoustic experimental data for coupled motion

identification study are compared with the measured data. Fig. 7.32 , Fig. 7.34 and Fig. 7.33 show the estimated positions in x, y, and z axes, and the positions in x, y and z axes obtained from the mathematical model response of SAGA before and the after system identification, respectively. Fig. 7.35 and Fig. 7.36 show the estimated yaw and pitch angles and the yaw and pitch angles obtained from the mathematical model

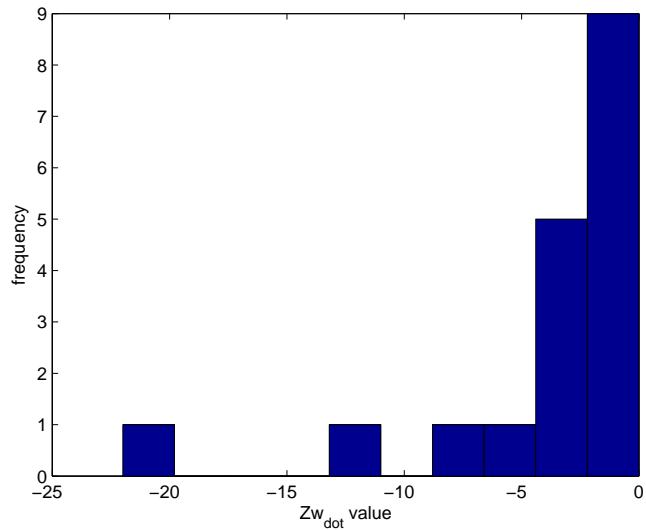


Figure 7.27: The histogram of $Z_{\dot{w}}$ value in the system identification based on the acoustic experimental data for coupled motion

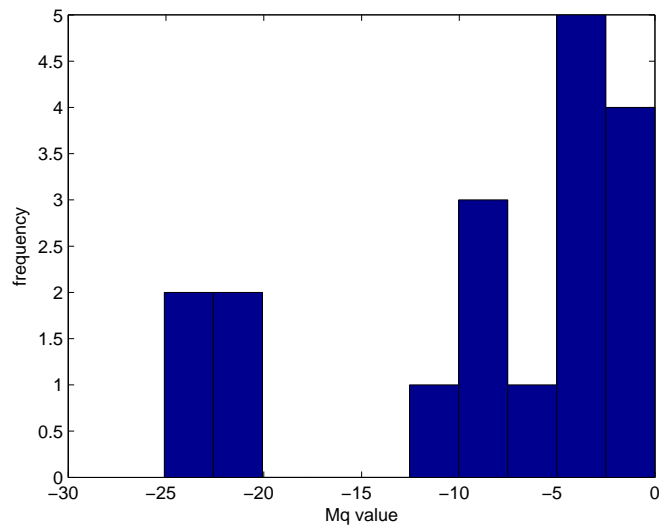


Figure 7.28: The histogram of M_q value in the system identification based on the acoustic experimental data for coupled motion

response of SAGA before and after the system identification, respectively. Since the added mass parameters and drag coefficients Y_v , Y_v' , K_p and K_p' cannot be identified accurately and also the experimental difficulties was mentioned in Chapter 6 the accuracy of the results are not sufficiently high.

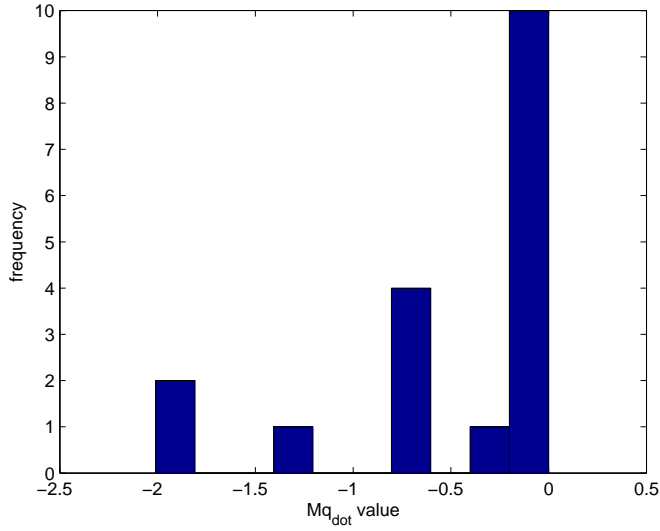


Figure 7.29: The histogram of M_q value in the system identification based on the acoustic experimental data for coupled motion

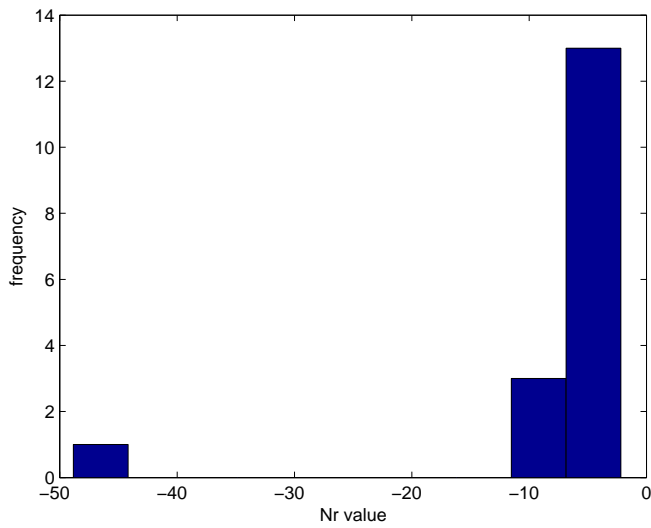


Figure 7.30: The histogram of N_r value in the system identification based on the acoustic experimental data for coupled motion

7.4 Conclusion

Decoupled motions of the vehicle and related parameters are defined. The optimization problem is formed to obtain these unknown parameters as in Eqn. 7.1. The system identification study of SAGA is performed using the simulation based data and

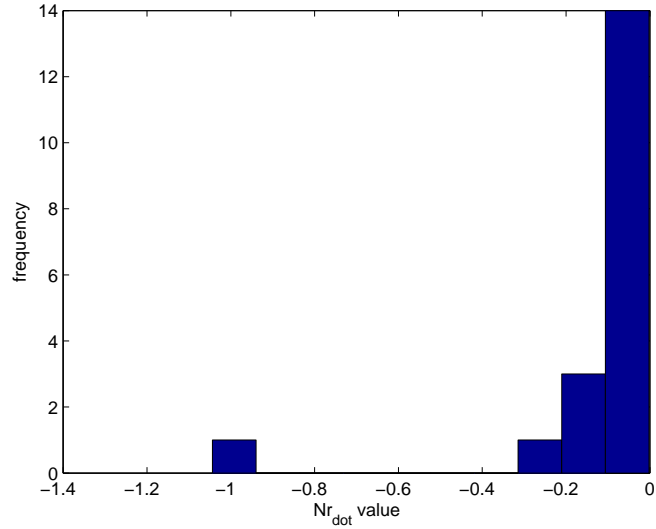


Figure 7.31: The histogram of $N_{\dot{r}}$ value in the system identification based on the acoustic experimental data for coupled motion

Table 7.8: Added mass parameters as the results of optimization for system identification based on the acoustic experimental data

Obtained added mass parameters	Actual added mass parameters
$X_{\dot{u}} = -4.947$	$X_{\dot{u}} = -1.94$
$Z_{\dot{w}} = -3.816$	$Z_{\dot{w}} = -3.94$
$M_{\dot{q}} = -0.487$	$M_{\dot{q}} = -0.1$
$N_{\dot{r}} = -0.134$	$N_{\dot{r}} = -0.03$

using the experimental data. System identification based on simulation data are performed for both coupled and uncoupled motions. For these motions, measured data is generated based on simulation from model response. It is expected that the result of the coupled motion test is more accurate than the result of the uncoupled motion test. The system identification is performed using experimental data for coupled motion. The system response is analyzed before and the after system identification based on acoustic experimental data.

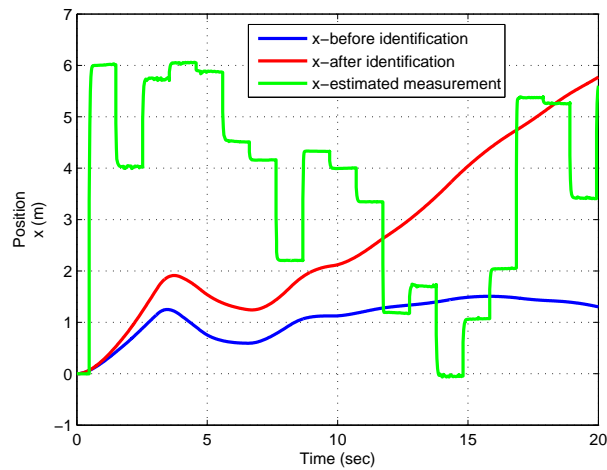


Figure 7.32: Estimated position in the x-axis from the Kalman filter (green line), the position in the x-axis from the system model response before system identification based on acoustic experimental data (blue line) and the position in the x-axis from the system model response after system identification based on acoustic experimental data (red line) with respect to time

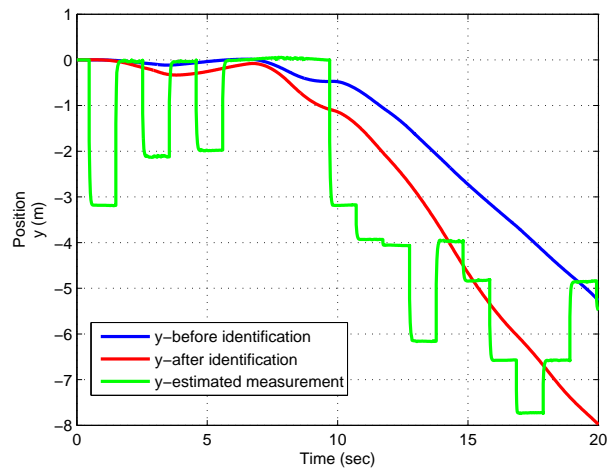


Figure 7.33: Estimated position in the y-axis from the Kalman filter (green line), position in the y-axis from the system model response before system identification based on acoustic experimental data (blue line) and position in the y-axis from the system model response after system identification based on acoustic experimental data (red line) with respect to time.

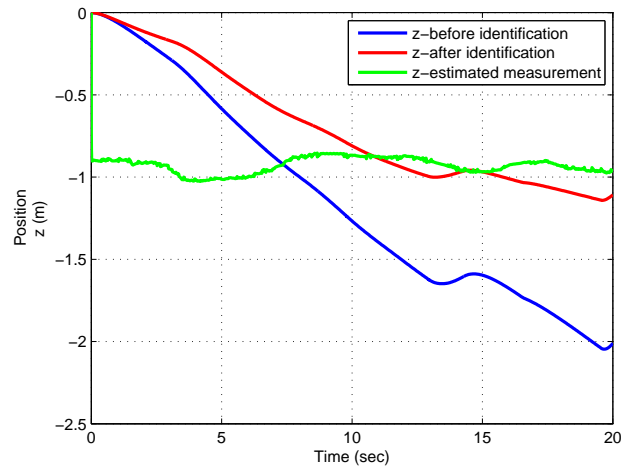


Figure 7.34: Estimated position in the z-axis from the Kalman filter (green line), the position in the z-axis from the system model response before system identification based on acoustic experimental data (blue line) and the position in the z-axis from the system model response after system identification based on acoustic experimental data (red line) with respect to time

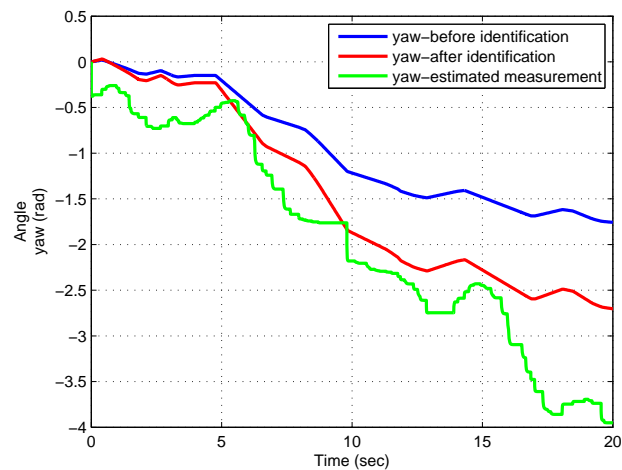


Figure 7.35: Estimated yaw angle from the Kalman filter (green line), the yaw angle from the system model response before system identification based on acoustic experimental data (blue line) and the yaw angle from the system model response after system identification based on acoustic experimental data (red line) with respect to time

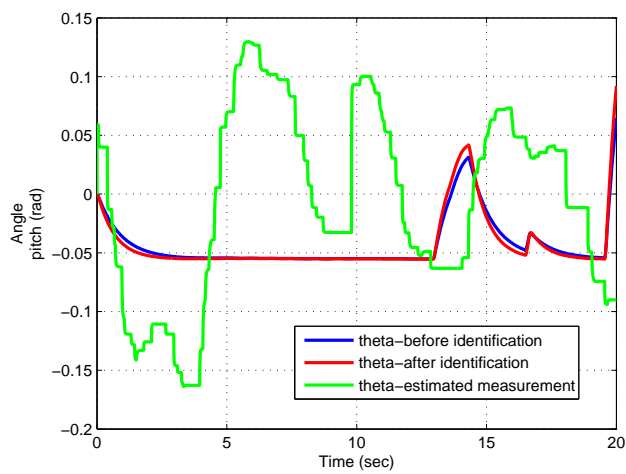


Figure 7.36: Estimated pitch angle from the Kalman filter (green line), the pitch angle from the system model response before system identification based on acoustic experimental data (blue line) and the pitch angle from the system model response after system identification based on acoustic experimental data (red line) with respect to time

CHAPTER 8

CONCLUSION AND FUTURE WORK

8.1 Conclusion

In order to construct the simulation model and to design the autopilots of the vehicle, first, a nonlinear mathematical model of SAGA was obtained in 6 DOF. System model was studied by activating different thrusters. Then, the autopilots were designed by using PID controllers. The surge, heave speed and the rotational velocity that changes the yaw angle and the depth and heading were controlled successfully. Before the guidance of the vehicle is performed, the navigation problem should be solved since the navigation data is the reference value to the guidance system. The inertial navigation system, acoustic and vision based measurement systems and the aiding sensors were integrated to solve the navigation problem. A suitable system model and a measurement model were defined. Error states were estimated using a Kalman filter. Estimated error states obtained from the output of the Kalman filter were used to correct the state estimates. These corrected state form the output of the navigation solutions. As shown from the simulation results, the estimated state errors are much smaller in the integrated navigation system.

Guidance was first performed with the way point guidance by LOS algorithm. It is seen that the vehicle can reach to the desired points by this algorithm. Vehicle can reach the desired points more smoothly by adjusting the weight of the thruster. Then, the guidance was performed using way point guidance based optimal control theory. An optimal control problem was constructed in such a way that the vehicle reaches the desired position and rotation with desired velocity, by spending minimum energy.

This optimal control problem was then solved by using the genetic algorithm toolbox of Matlab.

A nonlinear mathematical model of SAGA is obtained from a combination of system identification and a navigation study. Real-time experiments were performed using SAGA on a relatively small region in the swimming pool of METU. The navigation problem was solved by integrating the IMU data with the remaining sensor information, and the acoustic based measurement system. Since all the measurement data is noisy the fusion is performed using a Kalman filter algorithm. The system identification of SAGA is achieved by using the estimated data from the integrated navigation system. The unknown parameters, added mass and damping coefficients were obtained more accurately as the result of the system identification study. First, system identification of SAGA is performed using the navigation data based on simulation measurements. The results in the system identification for coupled motion based on simulation data are more accurate than the results for the uncoupled motion based on simulation measurements. Then, the system identification is performed based on experimental navigation data. The responses of the mathematical model of SAGA using the parameters with and without the system identification study are compared with the measured data. It is seen that the model response was improved after the system identification study. Accuracy of the experiment was affected because of the small experimental volume and short experiment duration. The connection of the each hydrophone cable affects the accuracy of the experiments since the received acoustic signals contain very high noise because of thrusters. Another very important factor affecting the accuracy is the degree of indeterminacy in the position of the hydrophones in the pool.

8.2 Future Work

In the future, open sea experiments will be done for solution of the navigation problem of SAGA using a USBL device and a surface vehicle. This solution is expected to be much more accurate for navigation. Multi- sensor data cannot be fused at the same time by the loosely coupled integration architecture. In order to fuse all measurements at the same time, different architectures such as cascaded filtered, federated

filtered type architectures can be used. During the system identification study, classical optimization algorithms in Matlab (fminsearch algorithm) as well as evolutionary optimization techniques such as differential evolution, particle swarm optimization and genetic algorithms can be used and compared as part of the future studies.

In the future, when the vehicle is operating under external guidance, the optimal autopilots can generate the reference signals for the real autopilots by interpolating the already calculated trajectories. Simulation studies can be performed for different initial and different final velocities. In this way, minimum value of the performance index can be obtained for a wide range of initial and final velocities. The results may also be verified experimentally.

Bibliography

- [1] S. S. Ahn, M. Ruzzene, F. Scorcelletti, and C. L. Bottasso. Configuration optimization of supercavitating underwater vehicles with maneuvering constraints. *IEEE Journal of Oceanic Engineering*, 35(3):647–662, July 2010.
- [2] J. P. J. Avila, J. C. Adamowski, N. Maruyama, F. K. Takase, and M. Saito. Modeling and identification of an open-frame underwater vehicle: The yaw motion dynamics. *Journal of Intelligent & Robotic Systems*, 66(1):37–56, 2012.
- [3] V. Bakaric, Z. Vukic, and R. Antonic. Improved basic planar algorithm of vehicle guidance through waypoints by the line of sight. In *First International Symposium on Control, Communications and Signal Processing*, pages 541–544, 2004.
- [4] K. A. C. Baumgartner, S. Ferrari, and A. V. Rao. Optimal control of an underwater sensor network for cooperative target tracking. *IEEE Journal of Oceanic Engineering*, 34(4):678–697, Oct 2009.
- [5] J. Biggs and W. Holderbaum. Optimal kinematic control of an autonomous underwater vehicle. *IEEE Transactions on Automatic Control*, 54(7):1623–1626, July 2009.
- [6] B. Bingham and W. Seering. Hypothesis grids: improving long baseline navigation for autonomous underwater vehicles. *IEEE Journal of Oceanic Engineering*, 31(1):209–218, Jan 2006.
- [7] G. C. Bishop. Gravitational field maps and navigational errors [unmanned underwater vehicles]. *IEEE Journal of Oceanic Engineering*, 27(3):726–737, Jul 2002.
- [8] E. Borhaug, A. Pavlov, and K. Y. Pettersen. Integral los control for path following of underactuated marine surface vessels in the presence of constant ocean

- currents. In *2008 47th IEEE Conference on Decision and Control*, pages 4984–4991, Dec 2008.
- [9] R. Brown and Y. Hwang. *Introduction to random signals and applied Kalman filtering*. John Wiley and Sons Inc., 1997.
- [10] A. E. Bryson and Y. C. Ho. *Applied optimal control, optimization, estimation and control*. 1975.
- [11] M. Caccia and G. Veruggio. Guidance and control of a reconfigurable unmanned underwater vehicle. *Control engineering practice*, 8(1): 21-37, 2000.
- [12] W. Caharija, K. Y. Pettersen, M. Bibuli, P. Calado, E. Zereik, J. Braga, J. T. Gravdahl, A. J. Sorensen, M. Milovanovi, and G. Bruzzone. Integral line-of-sight guidance and control of underactuated marine vehicles: Theory, simulations, and experiments. *IEEE Transactions on Control Systems Technology*, 24(5):1623–1642, Sept 2016.
- [13] F. Y. Cevher. Autopilot and guidance design for a mini rov (remotely operated underwater vehicle). Master’s thesis, METU, 2012.
- [14] H. H. Chen. Vision-based tracking with projective mapping for parameter identification of remotely operated vehicles. *Ocean Engineering*, 35(10):983 – 994, 2008.
- [15] D. Company. <http://www.desistek.com.tr/>.
- [16] J. Crassidis and J. Junkins. *Optimal estimation of dynamic systems*. 2004.
- [17] B. R. Dzikowicz, B. T. Hefner, and R. A. Leasko. Underwater acoustic navigation using a beacon with a spiral wave front. *IEEE Journal of Oceanic Engineering*, 40(1):177–186, Jan 2015.
- [18] T. Fossen. *Guidance and Control of Ocean Vehicles*. 1994.
- [19] N. Fukushima, M. S. Arslan, and I. Hagiwara. An optimal control method based on the energy flow equation. *IEEE Transactions on Control Systems Technology*, 17(4):866–875, July 2009.

- [20] P. Groves. *Principles of GNSS, Inertial, and Multi-Sensor Integrated Navigation Systems*. Boston:Artech House, 2008.
- [21] A. J. Healey and D. Lienard. Multivariable sliding mode control for autonomous diving and steering of unmanned underwater vehicles. *IEEE Journal of Oceanic Engineering*, 18(3):327–339, Jul 1993.
- [22] O. Hegrenaes and O. Hallingstad. Model-aided ins with sea current estimation for robust underwater navigation. *IEEE Journal of Oceanic Engineering*, 36(2):316–337, April 2011.
- [23] E. Y. Hong, T. K. Meng, and M. Chitre. Online system identification of the dynamics of an autonomous underwater vehicle. In *2013 IEEE International Underwater Technology Symposium (UT)*, pages 1–10, March 2013.
- [24] S. K. Kartal, E. Ege, and K. Leblebicioglu. Optimal autopilot and guidance of the roV: Saga. *IFAC-PapersOnLine*, 49(3):401406, 2016.
- [25] S. K. Kartal and K. Leblebicioglu. Vision-based navigation and system identification of unmanned underwater survey vehicle. In *2015 International Conference on Mathematical Methods, Mathematical Models and Simulation in Science and Engineering*, Vienna, Austria, 15-17 March, 2015.
- [26] S. Khanmohammadi, G. Alizadeh, J. Jassbi, and M. Pourmahmood. A new artificial intelligence approach for 2d path planning for underwater vehicles avoiding static and energized obstacles. In *2008 IEEE Congress on Evolutionary Computation (IEEE World Congress on Computational Intelligence)*, pages 1988–1995, June 2008.
- [27] L. Lasdon, S. Mitter, and A. Waren. The conjugate gradient method for optimal control problems. *IEEE Transactions on Automatic Control*, 12(2):132–138, Apr 1967.
- [28] P. M. Lee and B.-H. Jun. Pseudo long base line navigation algorithm for underwater vehicles with inertial sensors and two acoustic range measurements. *Ocean Engineering*, 34(3–4):416 – 425, 2007.

- [29] S. K. Lee, K. H. Sohn, S.-W. Byun, and J.-Y. Kim. Modeling and controller design of manta-type unmanned underwater test vehicle. In *Journal of mechanical science and technology*, 23(4): 987-990, 2009.
- [30] M. P. M. D. Agostino, A. M. Manzano. Performances comparison of different mems-based imu. In *Position Location and Navigation Symposium (PLANS), 2010 IEEE/ION, 2010*, pages 187201, 2010.
- [31] S. C. Martin and L. L. Whitcomb. Experimental identification of six-degree-of-freedom coupled dynamic plant models for underwater robot vehicles. *IEEE Journal of Oceanic Engineering*, 39(4):662–671, Oct 2014.
- [32] P. A. Miller, J. A. Farrell, Y. Zhao, and V. Djapic. Autonomous underwater vehicle navigation. *IEEE Journal of Oceanic Engineering*, 35(3):663–678, July 2010.
- [33] Y. Min and H. Junyin. The calibration of the usbl transducer array for long-range precision underwater positioning. In *IEEE 10th International Conference on Signal Processing Proceedings*, pages 2357–2360, Oct 2010.
- [34] K. Ogata. *Modern Control Engineering*. Prentice Hall PTR, 2001.
- [35] L. Paull, S. Saeedi, M. Seto, and H. Li. Auv navigation and localization: A review. *IEEE Journal of Oceanic Engineering*, 39(1):131–149, Jan 2014.
- [36] T. Prester. Development of a six-degree of freedom simulation model for the remus autonomous underwater vehicle. In *MTS/IEEE Oceans 2001. An Ocean Odyssey. Conference Proceedings (IEEE Cat. No.01CH37295)*, volume 1, pages 450–455, 2001.
- [37] P. Rigby, O. Pizarro, and S. B. Williams. Towards geo-referenced auv navigation through fusion of usbl and dvl measurements. In *OCEANS 2006*, pages 1–6, Sept 2006.
- [38] I. Spangelo and O. Egeland. Trajectory planning and collision avoidance for underwater vehicles using optimal control. *IEEE Journal of Oceanic Engineering*, 19(4):502–511, Oct 1994.

- [39] V. P. Srin. A vision for supporting autonomous navigation in urban environments. *Computer*, 39(12):68–77, Dec. 2006.
- [40] L. S. Y. Zhao, M. Haremuz. Stochastic modelling and analysis of imu sensors errors. *Archives of Photogrammetry, Cartography and Remote Sensing*, vol. 22, pages 437-449, 2011.
- [41] S. Zanolli and G. Conte. Remotely operated vehicle depth control. *Control Engineering Practice*, 2003, 11(4): 453-459.
- [42] A. Zielinski and L. Zhou. Precision acoustic navigation for remotely operated vehicles (rov). *Hydroacoustics Annual Journal*, pages 255-264, vol. 8., 2005.

APPENDIX A

EXPERIMENTAL WORK IN POOL AND LAKE

A.1 Experimental Work in Pool and Lake

Many pools and lakes experiments have been tested with SAGA. Firstly, pinger is fixed at the known position in the pool of METU and hydrophones are located separately in the pool as shown in Fig. A.1. It is observed that the distance between hydrophones and pinger is far away, signal sending from pinger is weak.

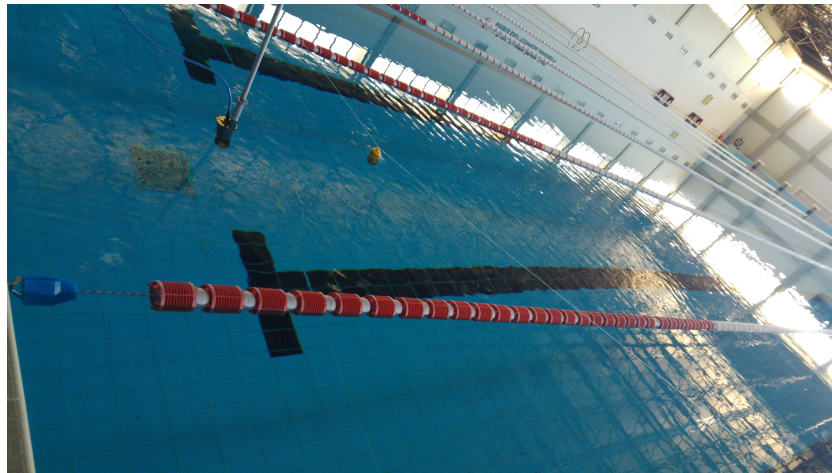


Figure A.1: Experiment to test whether the pinger works

In order to detect the critical distance between hydrophones and pinger, all hydrophones are collected and they are located at known positions in the pool. The critical distance between pinger and hydrophones is found as the pinger slowly gets away from the hydrophones. This experiment is shown in Fig. A.2 . Next, the acoustic based experiment is designed as shown in Fig. A.3 and it is supported by using the camera located above pool as shown in Fig. A.4.

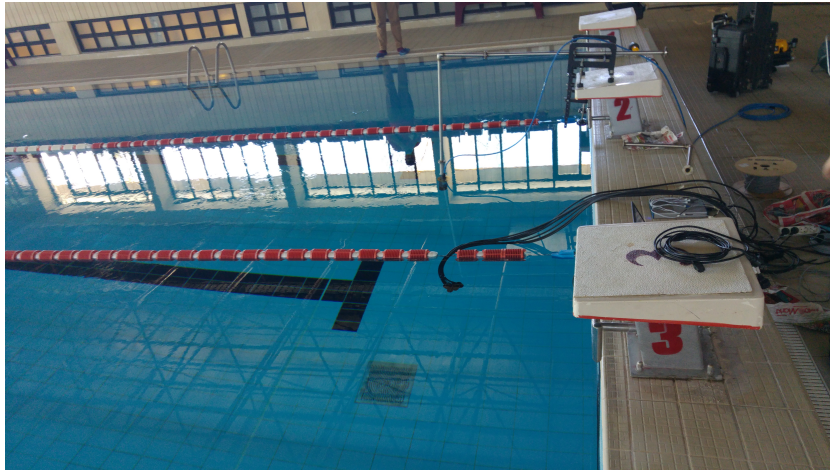


Figure A.2: Experiment to detect the critical distance between hydrophones and the pinger



Figure A.3: Acoustic-based navigation experiment set-up

In order to design the acoustic based navigation experiment using USBL, whether USBL works in the pool was checked first. It is observed that the signal reflections occur in the pool because the pool is very shallow to perform such an experiment. Hence, USBL does not work in the pool. This experimental set-up is shown in Fig. A.5. Then, whether USBL works in the lake is checked. The lake experiment preparation is shown in Fig. A.7 and Fig. A.6. Although there are some problems in the lake experiment, this study continues and it will be completed soon.



Figure A.4: Acoustic-based navigation experimental set-up

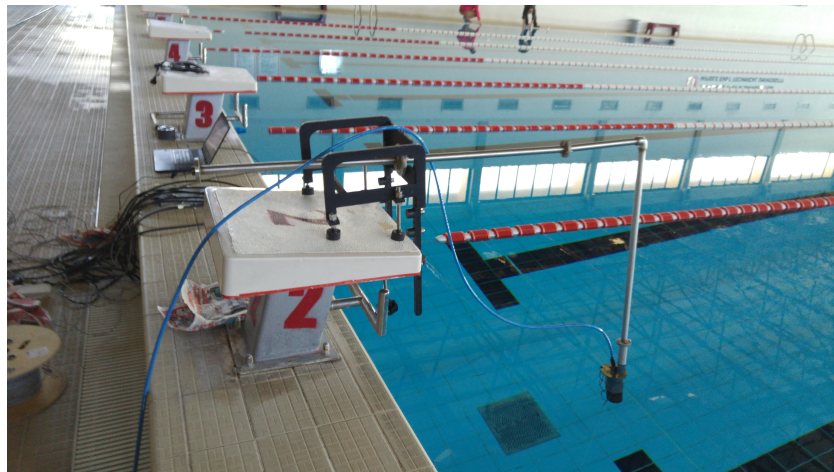


Figure A.5: Experiment to test whether USBL works in the pool



Figure A.6: Experiment to test whether USBL works in the lake



Figure A.7: Experiment to test whether USBL works in the lake

APPENDIX B

SOME INFORMATION OF SENSORS USED IN THE EXPERIMENT

B.1 UM7 Specifications

ATTITUDE AND HEADING SPECIFICATIONS

EKF Estimation Rate	500 Hz
Static Accuracy – Pitch and Roll	+/- 1 degree, typical*
Dynamic Accuracy – Pitch and Roll	+/- 3 degrees, typical*
Static Accuracy – Yaw	+/-3 degrees, typical*
Dynamic Accuracy – Yaw	+/- 5 degrees, typical*
Repeatability	0.5 degrees
Resolution	< 0.01 degrees

Figure B.1: Attitude and heading specifications

GYRO SPECIFICATIONS

Sensitivity change vs. temperature*	+/- 0.04% / deg C
Bias change vs. temperature*	+/- 20 deg/s from -40 C to +85 C
Rate noise density	0.005 deg/s/rHz
Total RMS noise	0.06 deg/s-rms
Non-linearity	0.2 % FS
Dynamic range	+/- 2000 deg/s
Cross-axis sensitivity	+/- 2%
Nonlinearity	0.2%
Mechanical frequency – x-axis	33 kHz nominal
Mechanical frequency – y-axis	30 kHz nominal
Mechanical frequency – z-axis	27 kHz nominal

Figure B.2: Gyro specifications

ACCELEROMETER SPECIFICATIONS

Sensitivity change vs. temperature*	+/- 0.02% / deg C
Bias change vs. temperature (X,Y)*	+/- 0.75 mg/deg C
Bias change vs. temperature (Z)*	+/- 1.50 mg/deg C
Rate noise density	400 ug / rHz
Dynamic Range	+/- 8 g

Figure B.3: Accelerometer specifications

MAGNETOMETER SPECIFICATIONS

Dynamic range	+/- 1200 uT
Initial scale factor tolerance*	+/- 4%
Initial bias tolerance*	+/- 300 uT
Dynamic range	+/- 1200 uT

Figure B.4: Magnetometer specifications

CURRICULUM VITAE

PERSONAL INFORMATION

Surname, Name: Karadeniz Kartal, Seda

Nationality: Turkish (TC)

Date and Place of Birth: 05.03.1982, Malatya

Marital Status: Married

E-mail: sedakaradeniz@gmail.com

EDUCATION

Institution	Degree	Year
METU, Electrical and Electronics Engineering Dept.	M.S.-PhD	2006-2017
METU, Basic English Dept		2005-2006
Firat University, Electrical and Electronics Engineering Dept.	B.S.	2001-2005
Inonu University, Biology Dept.		1998-2001
Malatya High School	High School	1995-1998

WORK EXPERIENCE

Year	Place	Enrollment
2005-2016	METU, Dept. of Electrical and Electronics Eng.	Research Assistant
2016-Present	BEU, Dept. of Electrical and Electronics Eng.	Research Assistant

PROJECT

TÜBİTAK 1001 project under grant 111E267: Path Planning for Unmanned Underwater Vehicles and Improvement of Underwater Optics with Acoustic Image Support, (2012-2015).

PUBLICATIONS

1. Seda Karadeniz Kartal, M. Kemal Leblebicioğlu, Emre Ege, "Bir İnsansız Sualtı Gözlem Aracının (Saga) Akustik ve Görüntüleme Temelli Yer Tespiti ve Sistem Tanılaması", *Yeni Türkiye Dergisi*, pp. 44-56, 2016.
2. Seda Karadeniz Kartal, M. Kemal Leblebicioğlu, Emre Ege, "Optimal Autopilot and Guidance of ROV: SAGA", *IFAC-PapersOnLine*, 49(3), pp. 401-406, 2016.
3. Seda Karadeniz Kartal, M. Kemal Leblebicioğlu, Emre Ege, "Bir İnsansız Sualtı Gözlem Aracı (SAGA) Yer Tespitinin Deneysel Testi ve Sistem Tanılaması", *Otomatik Kontrol Türk Milli Komitesi Ulusal Toplantısı (TOK)*, Eskişehir, 2016.
4. Seda Karadeniz Kartal, M. Kemal Leblebicioğlu, Emre Ege, "Optimal Autopilot and Guidance of ROV: SAGA", *14th IFAC Symposium a Control in Transportation Systems (CTS 2016)*, Istanbul, Turkey.
5. Seda Karadeniz Kartal, M. Kemal Leblebicioğlu, "Vision-based Navigation and System Identification of Unmanned Underwater Survey Vehicle", *Proceedings of the International Conference on Mathematical Methods, Mathematical Models and Simulation in Science and Engineering (MMSSE 2015)*, Vienna, March 15-17, 2015.
6. Seda Karadeniz Kartal, M. Kemal Leblebicioğlu, Emre Ege, "Bir İnsansız Sualtı Gözlem Aracının (SAGA) Akustik -temelli Yer Tespiti ve Sistem Tanılaması", *Otomatik Kontrol Türk Milli Komitesi Ulusal Toplantısı (TOK)*, Denizli, 2015.
7. Seda Karadeniz Kartal, M. Kemal Leblebicioğlu, Emre Ege, "Bir İnsansız Sualtı Gözlem Aracının (SAGA) Görüntüleme-temelli Yer Tespiti ve Sistem Tanılaması", *IEEE 23. Sinyal İşleme ve İletişim Uygulamaları Kurultayı (SİU 2015)*, Malatya.

8. Seda Karadeniz Kartal, M. Kemal Leblebiciođlu, "Bir İnsansız Sualtı Aracının Yer Tespiti ve GÜdümü", *Otomatik Kontrol Türk Milli Komitesi Ulusal Toplantısı (TOK)*, Kocaeli, 2014.
9. Seda Karadeniz Kartal, M. Kemal Leblebiciođlu, "Bir İnsansız Sualtı Aracının Navigasyonu", *Savunma Teknolojileri Kongresi*, Savtek, Ankara, 2014.
10. Seda Karadeniz Kartal, F. Yılmaz Cevher, M. Kemal Leblebiciođlu, "Bir İnsansız Sualtı Aracı: DSTR-300-4 için 3D Optimal GÜdüm Otopilot Tasarımı", *Otomatik Kontrol Türk Milli Komitesi Ulusal Toplantısı (TOK)* Niđde, 2012.
11. F. Yılmaz Cevher, S. Karadeniz Kartal, M. Kemal Leblebiciođlu, "Bir İnsansız Sualtı Aracı: DSTR-300-4 için Optimal GÜdüm Otopilot Tasarımı", *Otomatik Kontrol Türk Milli Komitesi Ulusal Toplantısı (TOK)*, Niđde, 2012.
12. Fırat Yılmaz Cevher, S. Karadeniz Kartal, M. Kemal Leblebiciođlu, "İnsansız Sualtı Aracı İçin Optimal Sapma Otopilot Tasarımı", *Savunma Teknolojileri Kongresi*, Savtek, Ankara, 2012.
13. Seda Karadeniz Kartal, Emre Ege, M. Kemal Leblebiciođlu, "Experimental Test of Acoustic-based Navigation and System Identification of an Unmanned Underwater Survey Vehicle (SAGA)", *Transactions of the Institute of Measurement and Control*, 2017 (Under Review)
14. Seda Karadeniz Kartal, Emre Ege, M. Kemal Leblebiciođlu, "Experimental Test of Vision-based Navigation and System Identification of an Unmanned Underwater Survey Vehicle (SAGA) for the Yaw Motion", 2017 (Under Preparation)